

Copyright © 1994, by the author(s).
All rights reserved.

Permission to make digital or hard copies of all or part of this work for personal or classroom use is granted without fee provided that copies are not made or distributed for profit or commercial advantage and that copies bear this notice and the full citation on the first page. To copy otherwise, to republish, to post on servers or to redistribute to lists, requires prior specific permission.

**OPTICAL PROXIMITY CORRECTION FOR
RESOLUTION ENHANCEMENT TECHNOLOGY**

by

David Michael Newmark

Memorandum No. UCB/ERL M94/34

16 May 1994

**OPTICAL PROXIMITY CORRECTION FOR
RESOLUTION ENHANCEMENT TECHNOLOGY**

Copyright © 1994

by

David Michael Newmark

Memorandum No. UCB/ERL M94/34

16 May 1994

ELECTRONICS RESEARCH LABORATORY

College of Engineering
University of California, Berkeley
94720

**OPTICAL PROXIMITY CORRECTION FOR
RESOLUTION ENHANCEMENT TECHNOLOGY**

Copyright © 1994

by

David Michael Newmark

Memorandum No. UCB/ERL M94/34

16 May 1994

ELECTRONICS RESEARCH LABORATORY

College of Engineering
University of California, Berkeley
94720

Table of Contents

| | |
|-------------------------------------------------------------------------------------|-----------|
| Chapter 1 Introduction | 1 |
| 1.1 Background and Motivation | 1 |
| 1.2 Thesis Organization | 3 |
| Chapter 2 Resolution Enhancement Techniques and Optical Proximity Correction | 6 |
| 2.1 Proximity and Projection Printing | 6 |
| 2.2 Resolution Enhancement Techniques | 6 |
| 2.2.1 Phase-Shifting Masks | 9 |
| 2.2.2 Off-axis Illumination | 12 |
| 2.3 Motivation for Optical Proximity Correction | 14 |
| 2.4 CAD Tools for Analyzing Resolution Enhancement Techniques | 17 |
| Chapter 3 Evaluating Resolution Enhancement Techniques | 23 |
| 3.1 Introduction | 23 |
| 3.2 E-D Trees | 23 |
| 3.3 Design Rule Generation (DRGEN) | 25 |
| 3.4 Initial Evaluation of Resolution Enhancement Techniques | 31 |
| 3.4.1 Introduction | 31 |
| 3.4.2 Conventional and Alternate Aperture | 33 |
| 3.4.3 Rim and Attenuating | 34 |
| 3.4.4 Annular Illumination | 34 |
| 3.4.5 Attenuating Mask with Annular Illumination | 37 |
| 3.4.6 Rim PSM with Annular Illumination | 37 |
| 3.4.7 Summary | 37 |
| Chapter 4 Experimental Verification: Dead Zones and Bias | 41 |
| 4.1 Introduction | 41 |
| 4.2 Rim Phase-Shift Mask Design | 41 |
| 4.3 Experimental Evaluation of Resist Lines Printed with Reticle | 44 |
| 4.3.1 Comparison of Aerial Image Simulations and Experiment | 46 |
| 4.3.2 Depth of Focus Predictions Compared to Experiment | 46 |
| 4.3.3 Dead Zones Confirmed by SEM cross-sections | 46 |
| 4.3.4 Comparison of Rim PSM with Annular Illumination to other PSM techniques | 53 |
| 4.3.5 Overlapping E-D Trees Predict the Correct Bias | 53 |
| 4.4 Summary | 56 |

| | |
|--------------------------------------------------------------------------------|------------|
| Chapter 5 Experimental Verification: Effects at Low k_1 | 57 |
| 5.1 Introduction | 57 |
| 5.2 Dense Features | 57 |
| 5.3 Mask Design | 58 |
| 5.4 Experimental Results | 59 |
| 5.5 Proximity Effects | 66 |
| 5.6 Using Simulation to Understand the Severity of the Proximity Effect | 66 |
| 5.7 Physical Explanation of the Proximity Effect | 69 |
| 5.8 Silicon Substrate Reflections | 70 |
| 5.9 Acid Diffusion in APEX-E | 78 |
| Chapter 6 2-D Optical Proximity Correction | 83 |
| 6.1 Introduction | 83 |
| 6.2 E-beam 2-D Proximity Correction | 84 |
| 6.3 Current Research on Optical Proximity Correction | 85 |
| 6.4 Edge-Nibbler Algorithm for Optical Proximity Correction of Small Layouts | 86 |
| 6.5 Concerns with the Edge -Nibbler Algorithm | 97 |
| 6.5.1 Depth of Focus Performance | 97 |
| 6.5.2 Mask Inspection | 97 |
| 6.5.3 Data Increase | 105 |
| 6.5.4 Fabrication Concerns | 106 |
| 6.6 Optical Proximity Correction of Larger Layouts | 106 |
| 6.6.1 Introduction | 106 |
| 6.6.2 Overview of Proposed Optical Proximity Correction System | 107 |
| 6.6.3 Divide and Conquer Approach | 108 |
| 6.7 The Pattern Library | 111 |
| Chapter 7 Polynomials for Intra and Inter-Feature Proximity Corrections | 116 |
| 7.1 Introduction | 116 |
| 7.2 Intra-Feature Proximity Correction | 116 |
| 7.3 Overview of Inter-Feature Proximity Corrections | 118 |
| 7.3.1 Representative Figure Method | 120 |
| 7.3.2 Partitioning the Periphery | 122 |
| 7.3.3 Learning Correction Functions for the Representative Regions | 123 |
| 7.3.4 Real Layout Results | 127 |
| 7.3.5 Bias Accuracy Problems | 129 |
| 7.4 Positional Influences | 132 |
| 7.5 Pixel-Based Approach | 134 |
| 7.6 Example with Current System | 139 |
| 7.7 Practical Implementation Issues | 144 |
| 7.8 Overall Perspective | 147 |
| Chapter 8 Conclusion | 150 |

Acknowledgments

I would like to express my thanks to Professor Andrew R. Neureuther. His enthusiasm, and understanding provided invaluable assistance during the course of this research. I am also deeply indebted to Dr. Sheila Vaidya for giving me access to the people and capabilities of AT&T Bell Labs and for her many thoughtful and extremely helpful insights regarding my thesis work. I would like to thank Jakub Segen, also of AT&T Bell Labs, for his advice on this project. Finally, I am grateful to Professor Avidesh Zakhor, Professor William Oldham, and Professor Ilan Adler for serving on my qualifying exam and for some thought provoking discussions.

It has been a wonderful experience working with my colleagues in the TCAD and lithography group, and I want to express my appreciation for their support.

Finally, I would like to thank my parents for their patience and understanding.

The financial support of SRC/Sematech Contract No. 93-MC-500 is gratefully acknowledged.

Chapter 1 Introduction

1.1 Background and Motivation

Optical lithography is a critical processing step in the production of integrated circuits. It allows engineers to rapidly produce many copies of an extremely complex and finely detailed pattern in photoresist by using a single mask or reticle and a complex optical system known as a stepper. The photoresist is then used as a temporary mask in subsequent processing steps to control the eventual pattern of thin-films on the wafer. Since the width of these films determine the device characteristics, lithographic resolution is critical to producing high quality and high performance integrated circuits. In fact, decreases in the minimum resolution of photolithography is the driving force behind faster microprocessors and denser DRAMs. Traditionally, reductions in wavelength and advances in resist technology allowed lithographers to gradually decrease the working resolution used to manufacture integrated circuits. Recently, however, these standard methods for linewidth reduction have become increasingly expensive, so resolution enhancement techniques, such as phase-shifting masks [1], off-axis illumination [2], and pupil plane filtering [3] have been introduced in an attempt to improve resolution without decreasing the wavelength or using expensive resist processes.

A large number of phase-shift techniques for improving resolution have surfaced over the last several years. The techniques include subresolution shifters [4], rim phase-shifting masks (PSM) [5], attenuated PSM [6], and alternate aperture PSM [1]. Each approach shows promise for improving the depth of focus and exposure latitude in optical lithography. A large depth of focus (DOF) is important for maintaining dimensional control across varying wafer topography and through the thick resist layers needed for planariza-

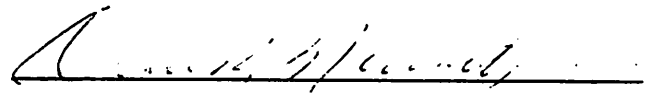
tion and plasma etch masks. It is also important for desensitizing the process to slight variations in resist thickness and exposure dose.

Despite the success of resolution enhancement technology in certain instances, such as printing $0.25\mu\text{m}$ lines and spaces at i-line [7,8], there remain a number of challenges which must be overcome before the techniques can be used extensively in integrated circuit processing. For example, current phase-shifting methods have problems with implementation of the technique to all types of features [9]. For example, an alternate aperture PSM can double the resolution and depth of focus for dense lines and spaces, but it does not affect isolated lines. Of course, that problem restricts the technique's usefulness to grating patterns, such as those found in DRAMs. A rim or attenuated PSM is more generally applicable to the random patterns found on masks for microprocessors, but dense geometries may not be resolved. In addition, sidelobes, or localized increases in intensity can occur, which may cause resist top-loss. New illuminator designs, such as an annular illumination, have also promised great improvements in depth of focus and resolution [2]. However, the designs typically work only for dense features. Again, isolated patterns show no resolution improvement and the method is not generally useful for most masks.

Another challenge faced by users of resolution enhancement techniques is that proximity effects cause large variations in the linewidth of minimum sized features. Proximity effects arise when the size of a printed feature depends on its neighbors. For example, the linewidth difference between dense and isolated lines is caused by proximity effects because the dimension of the line changes depending upon whether or not it is in an array. The most common proximity effects are caused by optical diffraction, and thus, they are called optical proximity effects. However, in general, proximity effects can also arise from the interplay between the optical image and the resist system. The problem is quite serious since typical lithographic processing requirements dictate that the linewidth should vary by a maximum of $\pm 10\%$ across the entire wafer. Linewidth variations caused

aspect of the assessment design graphs, the existence of a loss in depth of focus for certain feature sizes. The experiment also shows that bias corrections can be accurately predicted for a given set of features. In addition to optical effects, the influence of the resist and wafer parameters can be quite significant. Our experimental and simulation results of isolated lines indicate the importance of substrate reflections and resist acid diffusion on the linewidth.

Two dimensional optical proximity effects, such as the dependence of line end shortening on neighboring features, tend to occur frequently, and they require sophisticated biasing techniques. Our approach combines a 2-D bias algorithm with a pattern recognition system. The bias algorithm quickly converges to an optimized pattern, and it is the engine for a pattern recognition system which can bias large masks. The idea is to develop a library of base patterns and associated correction polynomials that can bias the base pattern for any periphery. The polynomials are calculated from the insight that bias corrections of individual pixels in the periphery can be linearly superimposed. With the approach, large layouts are corrected for certain critical features.



Prof. A. R. Neureuther

Committee Chairman

ABSTRACT

Optical Proximity Correction for Resolution Enhancement Technology

by

David M. Newmark

Doctor of Philosophy in Electrical Engineering and Computer Science

University of California at Berkeley

Professor Andrew R. Neureuther, Chair

Traditionally, lithographic resolution is improved by wavelength reduction or advanced resist processing. However, lithographic performance can be improved by modifying non-standard parameters such as the illuminator or mask. This thesis describes issues associated with non-traditional lithography enhancements.

To assess resolution enhancement techniques, a general design rule generation system is developed. This program, called DRGEN, is also capable of biasing features or adjusting feature edges differently than the designed mask. In our studies, DRGEN is used to simulate features consisting of lines and spaces while systematically varying three important lithographic variables, defocus, bias, and line-space ratio. The data from several thousand simulations of different pattern and enhancement techniques are summarized in a database from which we have extracted simple design graphs to assess enhancement technologies. The same database is then used to optimize the bias of patterns on the mask.

Experimental verification of our assessment and biasing approach is accomplished by designing and printing a rim phase-shifting mask. The experimental results verify a key

by proximity effects are often greater than this specification, as in [10], necessitating some type of pattern-based correction scheme. The process of correcting masks by adjusting or biasing edges to compensate for proximity effects is known as proximity correction.

This thesis explores the optical, resist, and thin-film aspects of proximity effects and proximity corrections. The general applicability of resolution enhancement techniques to typical masks is investigated through systematic simulation studies which suggest that a combination of mask and stepper enhancements can improve resolution and depth of focus for any feature. Optical/resist and optical/substrate interactions are investigated through an example that exhibits severe proximity effects which can only be understood by looking at these physical phenomena. In addition, design tools are created to calculate proximity corrections to compensate for the optical proximity effect.

1.2 Thesis Organization

Chapter 2 gives an overview of resolution enhancement techniques and a physical explanation of their mechanism. Chapter 3 describes a 1-D optical proximity correction tool, DRGEN, which can summarize the information from several thousand SPLAT aerial image simulations and allow the user to explore many mask and stepper configurations for possible resolution enhancement. As described in Chapter 4, DRGEN also allows the user to design state of the art biased rim phase-shift masks. In one experiment, a rim PSM is utilized to study a dead zone phenomenon observed in simulation and to explore DRGEN's capability for correctly biasing rim phase-shift masks. Chapter 5 describes another experiment in which rim phase-shifting masks and annular illumination are used to print $0.22\mu\text{m}$ dense and isolated bright field lines. Severe proximity effects observed with the resulting features are explained using the results of TCAD simulation tools. Chapter 6 describes the 2-D optical proximity effect and proposes a system architecture

for correcting masks to account for optical proximity effects. Chapter 7 discusses the implementation of certain key aspects of that system, including a novel way to account for the bias of peripheral features on a main pattern. The chapter concludes with an example of a mask corrected by biasing only the ends of lines.

References for Chapter 1

- [1] M.D. Levenson, N.S. Viswanathan, R.A. Simpson, "Improving Resolution in Photolithography with a Phase-Shifting Mask," *IEEE Transactions on Electron Devices*, Vol. Ed-29, No. 12, pp. 1812-1846, December 1982.
- [2] Satori Asai, Isamu Hanyu, and Kohki Hikosaka, "Improving projection lithography image illumination by using sources far from the optical axis," *J. Vac. Sci. Technol. B* 9(6), Nov/Dec 1991, pp. 2788-2791.
- [3] H. Fukuda, T. Terasawa, and S. Okazaki, "Spatial filtering for DOF and resolution enhancement in optical lithography," *J. Vac. Sci. Technol. B* 9, p. 3113 (1991).
- [4] T. Terasawa, N. Hasegawa, T. Kurosaki, T. Tanaka, "0.3 micron Optical Lithography Using a Phase-Shifting Mask," *SPIE Proceedings*, vol. 1088, p. 25, 1989.
- [5] Y. Yanagishita et al., "Phase-shifting photolithography applicable to real IC patterns," *SPIE Proceedings*, vol. 1463, p. 207 (1991).
- [6] B. Lin, "The attenuated PSM," *Solid State Tech.*, Jan. 1992, p. 43.
- [7] A. Nitayama, T. Sato, K. Hasimoto, F. Shigemitsu, M. Nakase, "New PSM with self-aligned phase shifters for quarter micron lithography," *1989 IEDM Tech Digest*, p. 3.3.1 (1989).
- [8] I. Hanyu, S. Asai, K. Kosemura, H. Ito, M. Nunokawa, and M. Abe, *SPIE Proceedings*, vol 1264, p. 167, 1990.
- [9] D.M. Newmark and A.R. Neureuther, "Phase-Shifting Mask Design Tool," *BACUS Photomask Technology*, 1991.
- [10] W.N. Partlo, P.J. Thompkins, P.G. Dewa, P.F. Michaloski, "Depth of Focus and Resolution Enhancement for i-line and deep-UV Lithography Using Annular Illumination," *SPIE: Optical/Laser Microlithography VI*, pp. 137-157, March 1993.

Chapter 2 Resolution Enhancement Techniques and Optical Proximity Correction

2.1 Proximity and Projection Printing

To preface a discussion of optical proximity correction for resolution enhancement techniques, it is necessary to begin with a brief overview of the theory of optical lithography and projection printing. Optical lithography is a method for transferring patterns from a mask into photoresist on a wafer. The most basic pattern transfer mechanism, proximity printing, is shown in Fig. 2.1. An ultra-violet light source illuminates a mask which contains chrome patterns that either block the light or allow it to pass through. Light not blocked by the mask exposes the resist on the substrate. The exposed resist is either rendered soluble or insoluble depending on the tone of the resist; the development process removes the soluble resist, leaving the pattern or its inverse.

Projection printing was developed to eliminate the need for the mask and resist to be in close contact. The diagram of this system is shown in Fig. 2.2. Again, a DUV light source illuminates the mask, but the image of the mask is now projected through a series of lenses to the wafer. The actual intensity pattern is not as sharp as the mask since diffraction effects allow some light to enter the opaque regions. The lens acts as a low pass spatial filter which cuts off higher spatial frequencies. Thus, the image loses some fidelity at the wafer plane, and, for example, a square wave will resemble a sinusoid. The image can still generate sharp resist profiles providing the contrast is above a certain threshold.

2.2 Resolution Enhancement Techniques

As have technologists in all other areas of the semiconductor industry, lithographers have continuously strived to advance the technology. In the past, equipment manufacturers improved stepper technology by decreasing the wavelength (λ) [1,2] and increasing

Proximity Printing for Optical Lithography

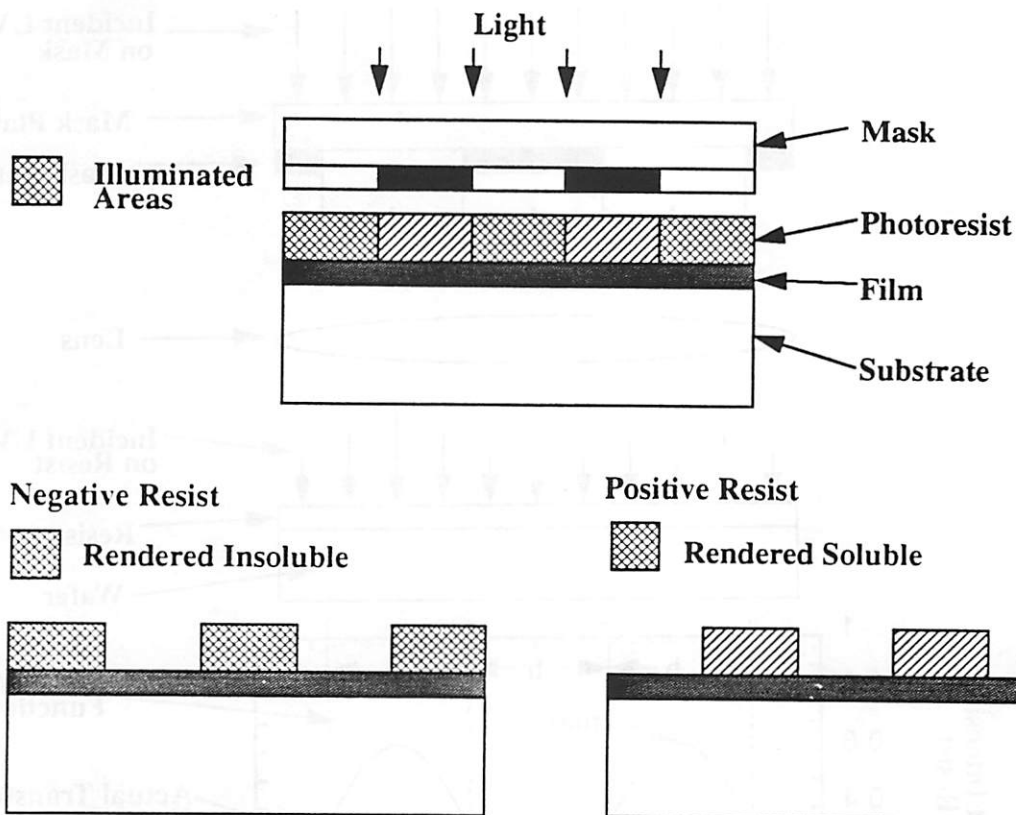


Figure 2.1 Proximity printing with optical lithography. The diagram shows the exposure and development of positive and negative resist.

the numerical aperture (NA). Based on the Rayleigh criterion for minimum resolution (Eq. 2.1), the combination of lower wavelengths and higher NA should improve the resolution. This change allows steppers to print smaller linewidths, but it requires new equip-

$$R = k_1 \frac{\lambda}{NA} \quad (2.1)$$

ment. Unfortunately, the expense of moving to each successive generation of lithography equipment has increased. For this reason, technologists are interested in ideas which can improve resolution without changing the wavelength and numerical aperture. Resolution

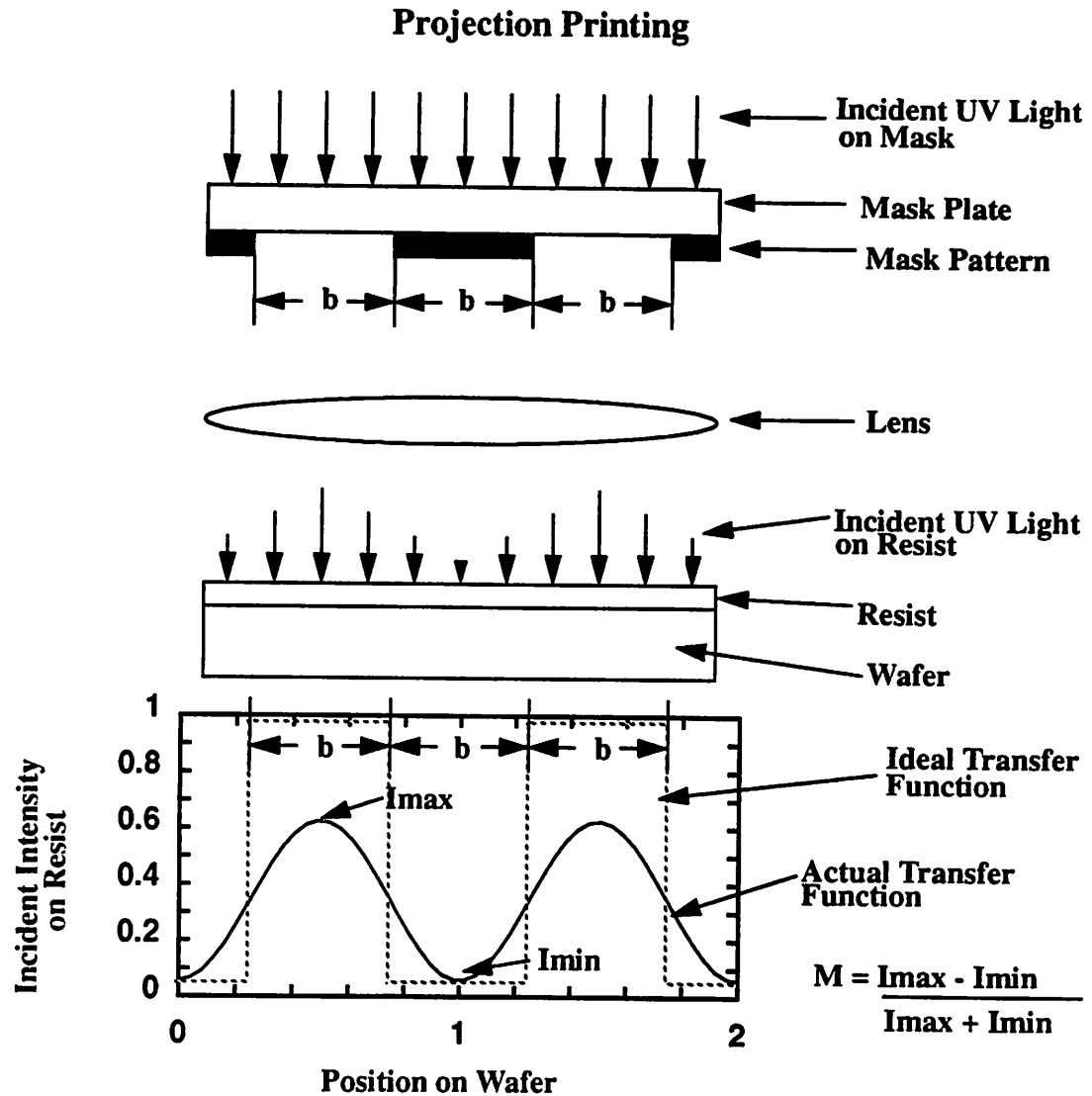


Figure 2.2 Simplified diagram of projection printing.

enhancement techniques fit this description since they can be implemented without dramatically changing the stepper itself. The basic idea is to change the technology factor, k_1 , in Eq. 2.1, rather than λ and NA. There exist a variety of resolution enhancement techniques which have the potential to accomplish this task, such as phase-shifting masks [3], off-axis illumination [4], and pupil plane filtering [5].

2.2.1 Phase-Shifting Masks

There are two categories of phase-shifting masks, strong and weak. The difference between the techniques can best be explained by describing diffraction limited imaging with the diagram in Fig. 2.3. Coherent light illuminates the line and space grating resulting in diffracted orders. If the system is diffraction limited, only the -1, 0 and +1 orders are captured by the projection lens. These orders interfere to form the aerial image.

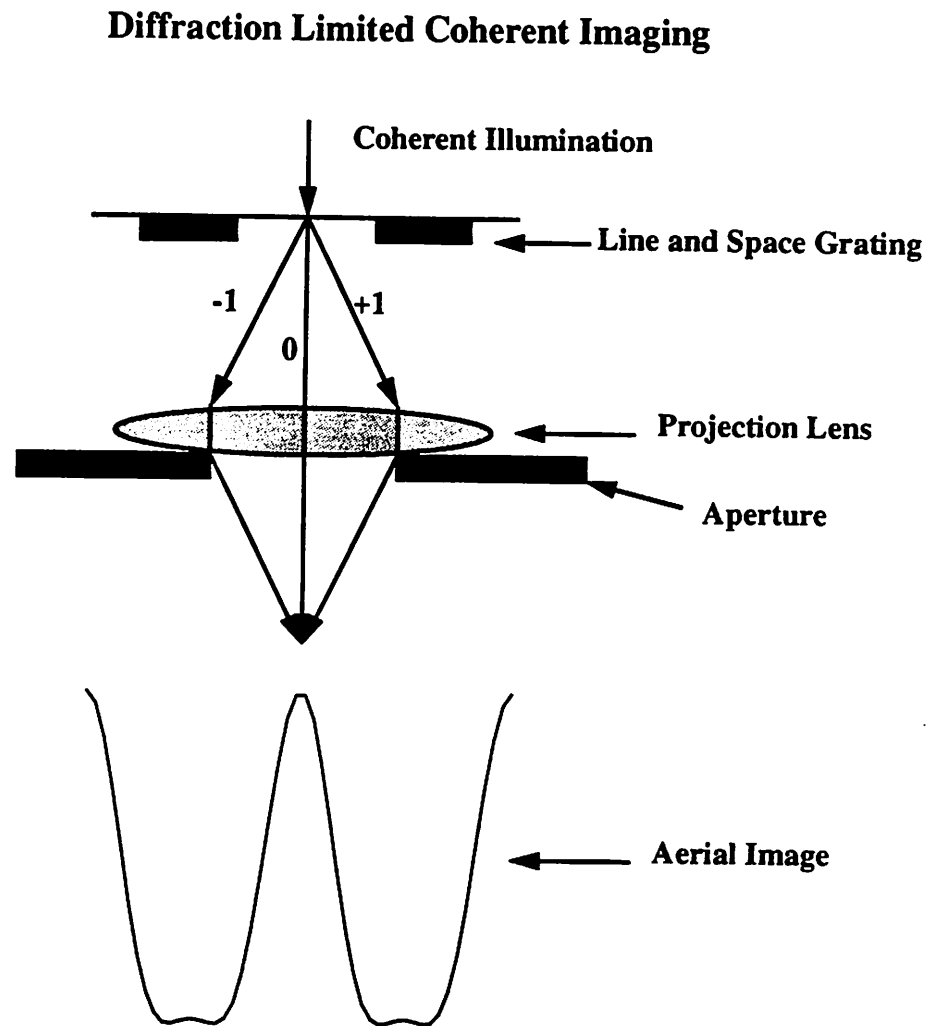


Figure 2.3 Diffraction limited coherent imaging. The -1, 0 and +1 orders combine to form the aerial image at the wafer plane.

Strong phase-shifting masks, consisting of the alternate aperture PSM [3], chromeless PSM [6,7], and phase-edge technology [8], achieve better resolution by removing the zero order. These kinds of phase-shifting masks are shown in Fig. 2.4. The chromeless and phase-edge techniques rely on the fact that nearby areas which are 180 degrees out of phase, create dark regions. Thus, the mask in Fig. 2.4a creates a line and space pattern and the mask in Fig. 2.4b produces a narrow isolated line. The alternate aperture technique, on the other hand, uses alternating 180 and 0 phase regions separated by chrome to enhance resolution and depth of focus. This type of phase-shifting mask is shown in Fig. 2.4c. The

Strong Phase-Shifting Masks

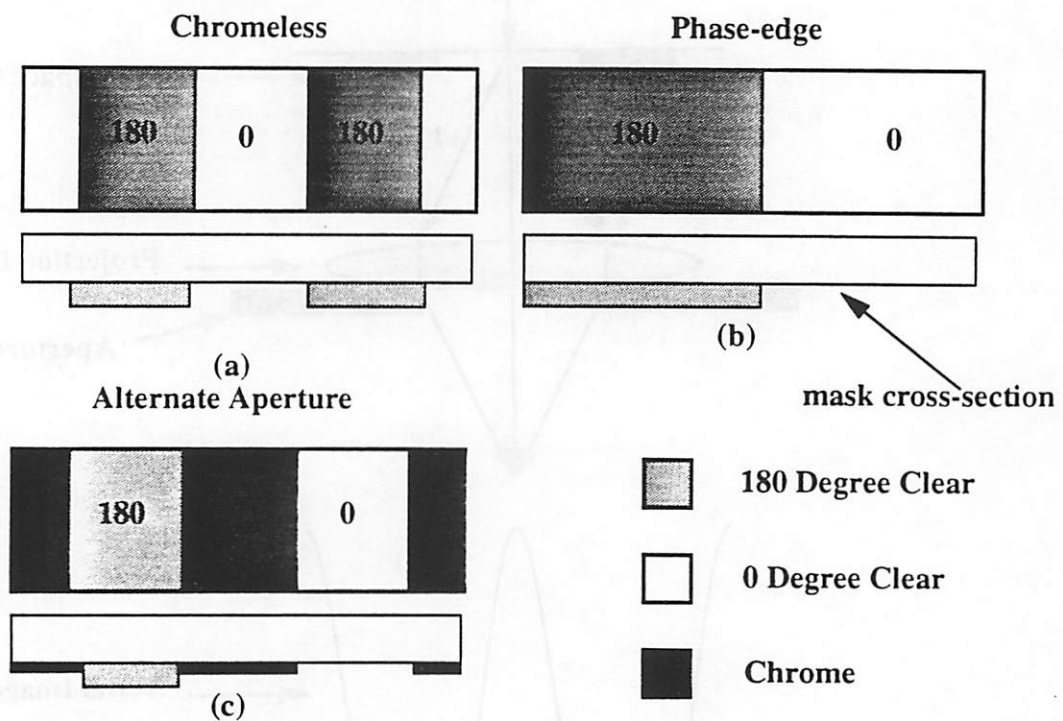


Figure 2.4 Strong phase-shifting masks, (a) chromeless, (b) phase-edge, and (c) alternate aperture.

explanation for the performance of this phase-shifting technique can be found by examining the diagram of Fig. 2.5, which shows the removal of the zero order by the chromeless phase-shifting mask technique. Removal of the zero order also leads to frequency doubling of the image which effectively increases the resolution by a factor of two.

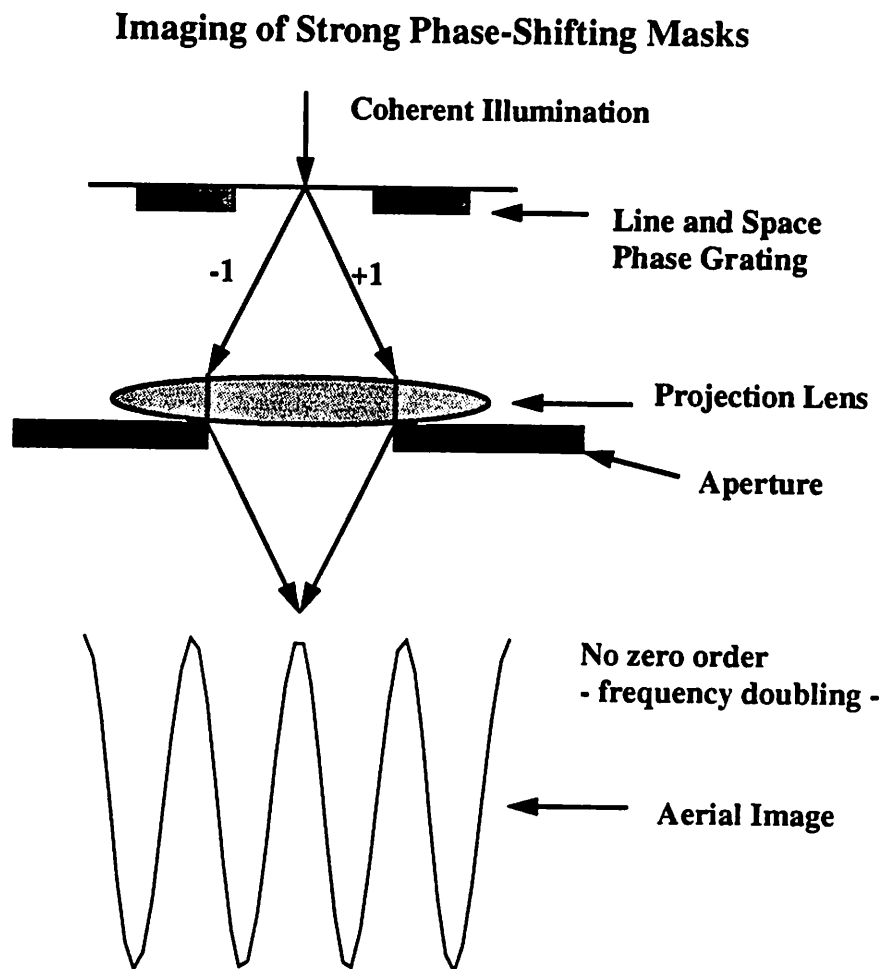


Figure 2.5 Imaging of a strong phase-shifting mask. The zero order has been eliminated by this technique and the frequency of the image is doubled.

Weak phase-shifting masks, on the other hand, less dramatically change the picture of diffraction limited imaging. In fact, the diffraction of weak phase-shifting masks is remarkably similar to Fig. 2.3. The main difference is that the weighting of the diffraction orders is changed, resulting in improved depth of focus. The effect on the aerial image is a sharpening of the intensity slope, which allows one to use the method for improving resolution. Weak phase-shifting techniques are shown in Fig. 2.6. The rim PSM [9] produces sharper profiles through the use of phase outriggers near clear and dark lines. The 180

Weak Phase-Shifting Masks

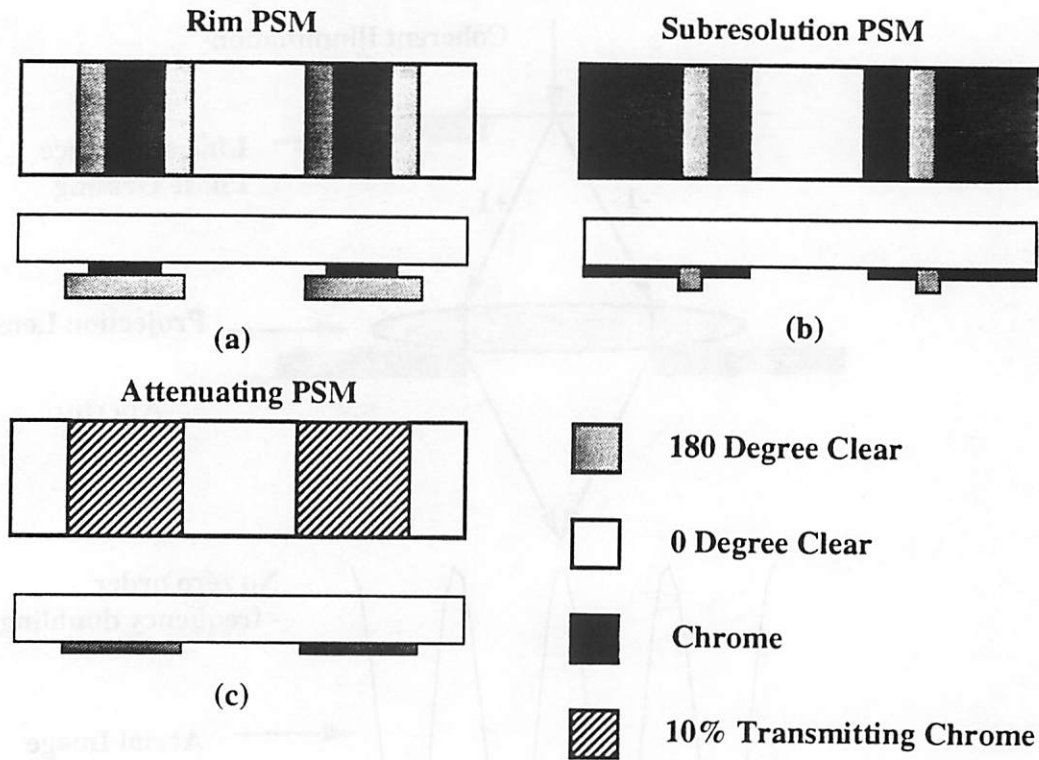


Figure 2.6 Weak phase-shifting mask techniques. (a) rim PSM, (b) subresolution PSM, and (c) attenuating PSM.

degree phase shifted subresolution shifters [10] boost the intensity of clear features. The dark areas of the attenuated mask are phase-shifted by π but with an attenuated amplitude that prevents the transmission of too much light through the dark areas. The negative amplitude provides the desired phase-shift improvement to the image [11]. More complete discussion of the various phase-shifting techniques can be found in [12].

2.2.2 Off-axis Illumination

Off-axis illumination has also been studied to improve the depth of focus and resolution in lithography. Various techniques have appeared in the literature including oblique [13], separated [14], quadrupole [15,16], and annular [17,18,19] illumination. Although

any off-axis technique will enhance the depth of focus for dense lines and spaces of a certain orientation, only annular illumination works with any feature orientation and places no restriction on mask layout [20]. The explanation for the dramatic imaging improvements with annular illumination can be found in [20] and [21]. Basically, annular illumination is very similar to strong phase-shifting masks since only two diffracted orders are passed through the lens. In the case of annular illumination, however, the 0 and +1 orders are captured by the imaging system. These orders recombine to form the image. As with the strong phase-shifting mask, this imaging system is capable of delivering frequency doubling. The reason annular illumination can not quite achieve frequency doubling is that the 0 and +1 orders are not equal and this creates some background intensity which reduces the contrast. Fig. 2.7 shows the diffracted orders for annular illumination.

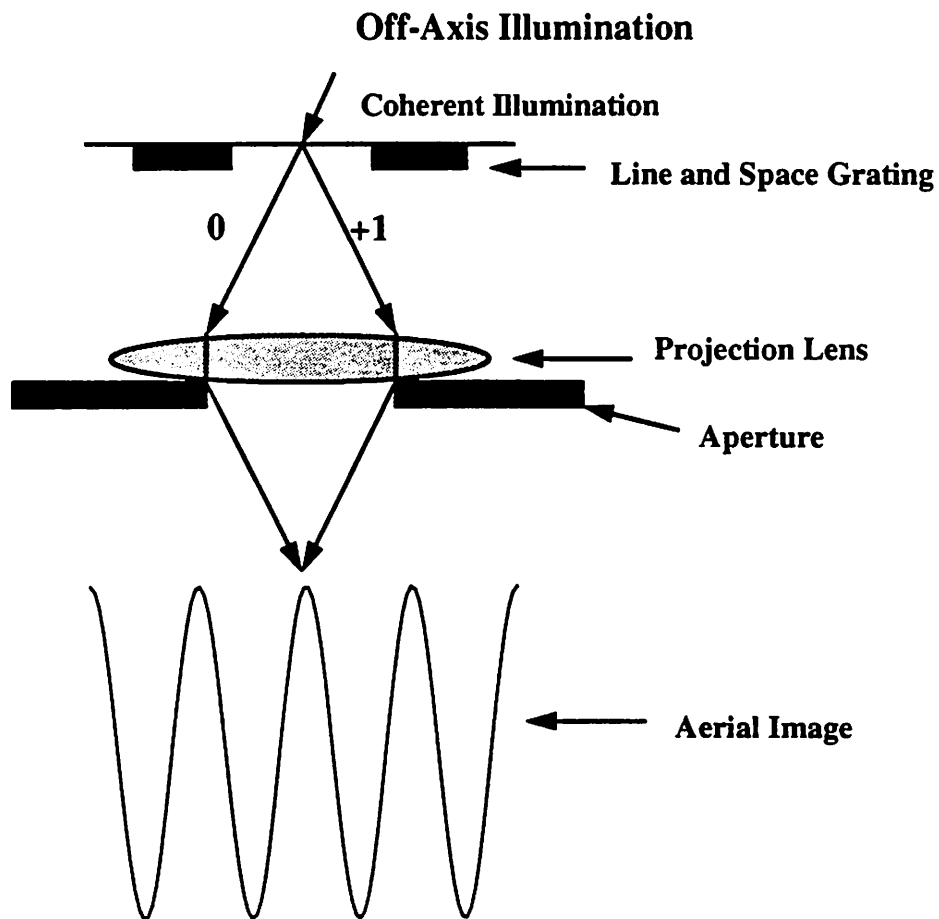
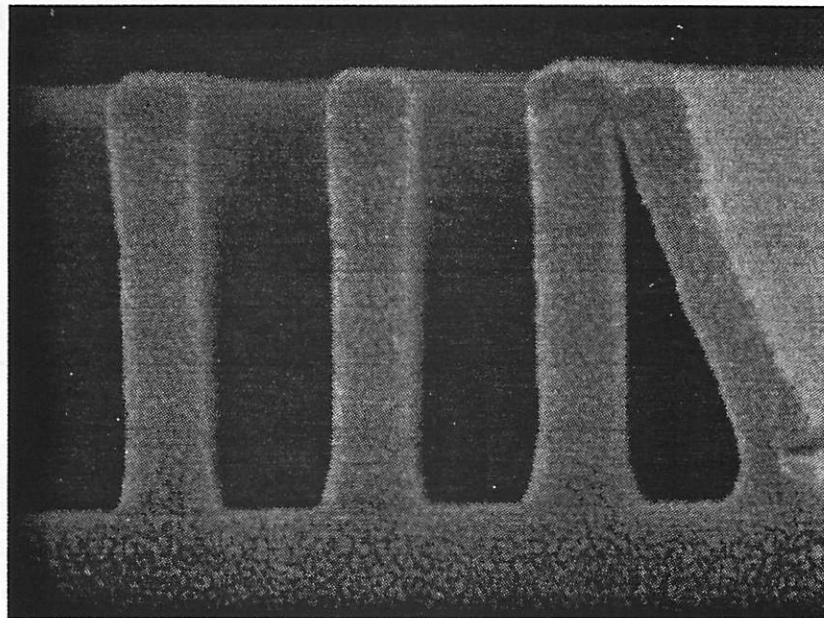


Figure 2.7 Annular illumination imaging of dense lines and spaces. Only the 0 and +1 orders are captured by the projection lens.

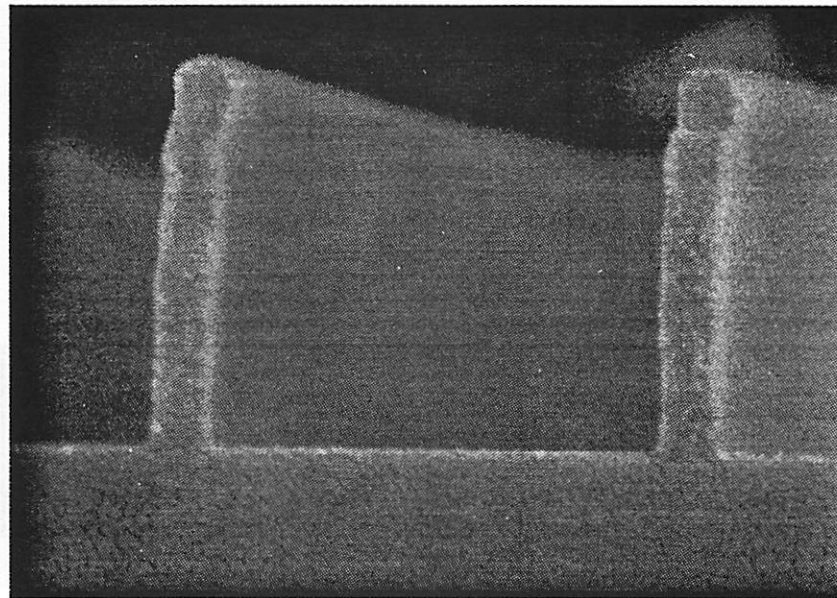
2.3 Motivation for Optical Proximity Correction

Initial experimental and simulation results with resolution enhancement techniques indicate that even though they can extend resolution and depth of focus, there are many technology challenges. For example, while annular illumination improves the depth of focus for dense lines and spaces, it reduces the focus latitude for isolated lines. Often the reason for the poor performance of isolated features can be traced to a linewidth change which rapidly brings the critical dimension out of control as focus shifts. This problem can be seen clearly in the SEM cross sections of Fig. 2.8. The rim phase-shifting mask used for these exposures has the same rim size for both dense lines and spaces and isolated lines. The resist profiles in Fig. 2.8 show that the linewidth of the image printed in APEX-E resist is much greater for the dense lines and spaces than for the isolated line. This problem is a pattern dependent proximity effect since the linewidth of the feature depends on its surroundings. In order to bring the linewidth back into control, the rim width of the isolated line on the phase-shift mask must be biased such that the dimension of the isolated line prints at the correct size. The rim width for the dense lines and spaces should remain the original size. Biasing the mask in this way is a pattern dependent proximity correction since the dense and isolated features are biased differently. The bias on the mask before and after the proximity correction is shown in Fig. 2.9.

In general, the problem is even more complex since masks with random logic have many different environments in which each feature must be corrected [22]. Furthermore, substrate reflections, resist reaction kinetics, and resist dissolution effects also play a role in influencing the profile and linewidth of the resist features. For instance, substrate reflections can lead to linewidth narrowing for off-axis illumination [23].



(a)



(b)

Figure 2.8 SEM photographs of (a) $0.22\mu\text{m}$ dense lines and spaces and (b) $0.22\mu\text{m}$ lines at a pitch of $1.08\mu\text{m}$ at $-0.6\mu\text{m}$ defocus and $16.8\text{mJ}/\text{cm}^2$. The center of focus is approximately $-0.6\mu\text{m}$. Note the large linewidth change between the dense and isolated features. As measured at the base of the resist, the linewidth changes from $0.21\mu\text{m}$ to $0.15\mu\text{m}$ from (a) to (b). These lines were printed using a 4X GCA DUV stepper with 0.53 NA and 0.6-0.7 partial coherence in $1.0\mu\text{m}$ of APEX-E positive resist with a rim phase-shifting mask.

Proximity Correction of Rim Phase-Shift Mask

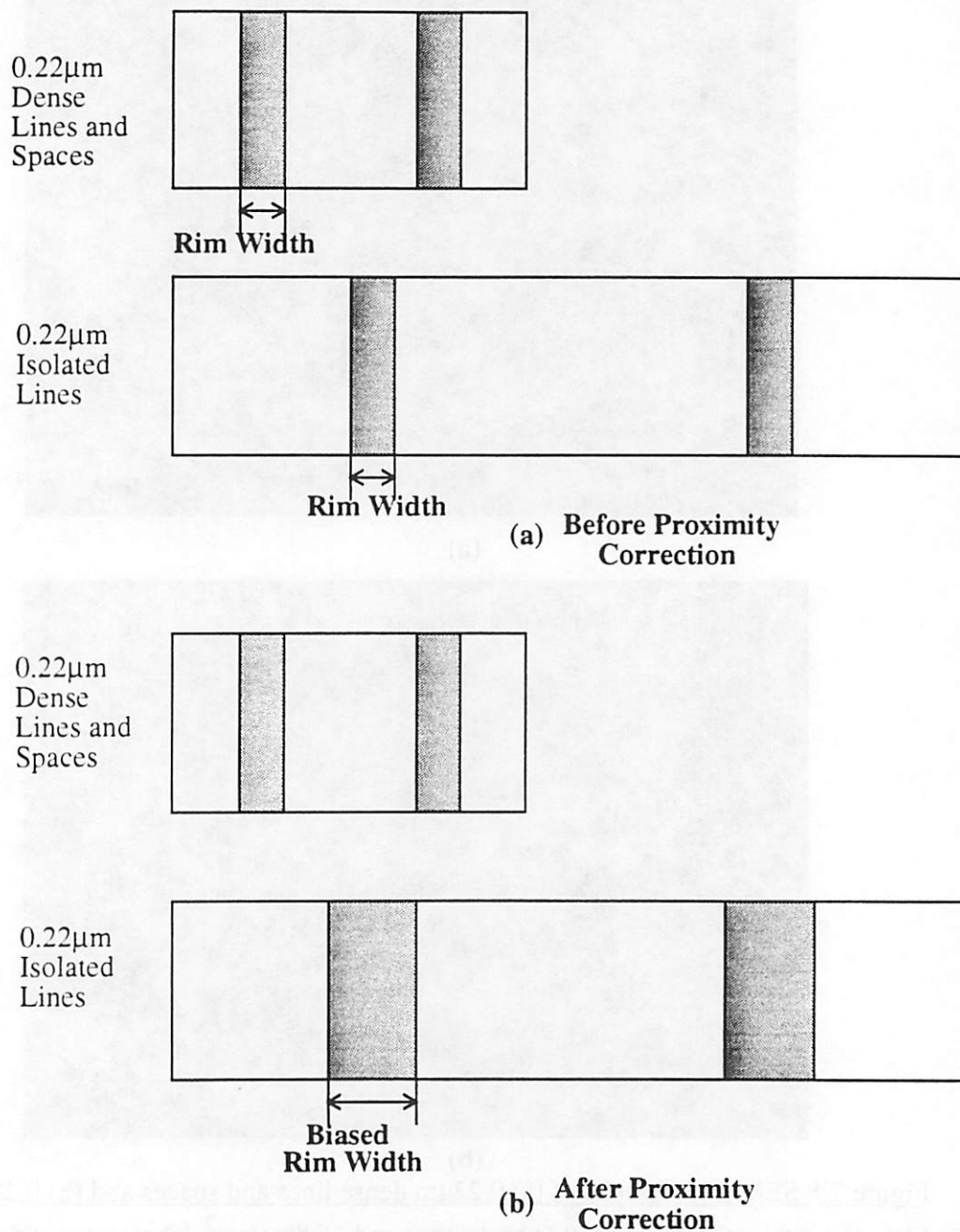


Figure 2.9 (a) Rim phase-shifting mask for printing dense and isolated lines before proximity correction. Use of this mask resulted in the features shown in Fig. 2.8. (b) Proximity corrected rim phase-shifting mask for printing dense and isolated lines. Note that the rim width of the isolated lines is now different from the rim width of the dense lines and spaces.

2.4 CAD Tools for Analyzing Resolution Enhancement Techniques

As we have shown, there are a large number of possible resolution enhancement techniques and various trade-offs associated with their use. Deciding which resolution enhancement technologies to use is particularly complex because all of these techniques have the common limitation that they do not affect all features in the same manner. While experimentation is viewed as the ultimate means of verification, it is far too slow and expensive to examine every alternative. On the other hand, simulation programs such as SPLAT (Simulation of Projection Lens Aberrations via TCCs) [24] can generate mask pattern images in a few seconds. Coupling these image simulation programs with post processors to extract measures of image quality can provide an effective means of evaluating these technologies.

Based on this need, a number of mask analysis and design systems have emerged. Initial work by K.K.H. Toh was directed towards the development of SPLAT, a fast and robust optical aerial image simulation program [24]. Further work led to the development of an analysis program which could run SPLAT for several iterations and extract pertinent information from the image cut lines [25]. Industrial versions of SPLAT have been developed leading to products such as DEPICT-2™, TMA's lithography simulation software [26]. In addition, researchers at AT&T and IBM have started developing other automated approaches for assessing technology issues [27,28]. Along these same lines, MASC was developed at the University of California, Berkeley [29,30]. Results from these simulation programs fed a growing realization that much more sophisticated tools would be necessary to design masks utilizing resolution enhancement techniques.

Although the CAD tools discussed above are useful for investigating the performance of some phase-shifting mask features, they are not useful for complex problems on real masks involving millions of patterns. For example, proximity correction for production masks is much more difficult since the corrections depend on the local environment

throughout the mask. Even for 1-D features, there are so many possible situations which may occur on a real mask that it would be extremely time-consuming to determine the correct mask dimensions experimentally. For this reason, computer simulations are necessary to speed up the experimental work. New ways are needed to deal with the mask database since pattern-based modifications must be incorporated into an existing layout. Also, these design techniques will be computationally intense and ways must be found to speed up the computations. Finally, accurate simulations of resist and substrate effects are necessary. If these problems can be tackled, appropriate CAD tools can be incorporated into the mask design process, and it may be possible to adjust the mask automatically to account for proximity effects.

However, today's CAD tools are clearly inadequate for undertaking proximity correction. While TCAD tools can simulate image, substrate, and resist effects, the number of possible situations is so overwhelming that off the shelf optimizers cannot be used. Instead, new systematic approaches are necessary which involve use of intermediate metrics and smarter approaches. The metrics and approaches are utilized in such a way that they lead to important understandings of the underlying phenomena. Experimental verification also results in greater understanding of the problems. The key understandings can then be incorporated into a smart algorithm which can quickly correct millions of features.

Our initial work in this area began with a partnership with AT&T to examine various resolution enhancement approaches. This need drove the creation of DRGEN which provides a facility to quickly evaluate resolution enhancement techniques in 1-D and bias masks to correct proximity effects. Experimental results from a mask designed to print $0.3\mu\text{m}$ features ($k_1=0.6$) indicate that DRGEN predicts the correct bias at this dimension. The same experiment also demonstrates the existence of dead zones for spaces of varying pitch. Additional work with $0.22\mu\text{m}$ features ($k_1=0.47$) demonstrates the linewidth nar-

rowing phenomenon for isolated versus dense features and indicates the inadequacy of aerial image simulation for predicting the bias at this k_1 . Out of this work grew a realization that it would be necessary to work with 2-D layouts. Initially, a fast optimizer is designed which can bias small patterns in five to ten iterations. To apply the results to larger layouts, pattern classification approaches are considered to speed up the correction process. An important result of the pattern classification system is that the change in the bias of a main pattern can be computed by a sum of the individual biases caused by features in the periphery. The complexity of the proximity correction problem is evaluated by considering the angular dependence of pixel-based correction elements. Finally, the bias system is incorporated into the OCT/VEM CAD framework.

References for Chapter 2

- [1] R.L. Sandstrom, R.P. Akins, U.K. Sengupta, C. Reiser, D.G. Larson, and S.L. Anderson, "Krypton fluoride excimer laser for microlithography," *SPIE Proceedings*, vol 1088, pp. 407-415, 1989.
- [2] V. Pol, J.H. Bennewitz, G.C. Escher, M. Feldman, V.A. Firtion, T.E. Jewell, B.E. Wilcomb, and J.T. Clemens, "Excimer laser-based lithography: A deep ultraviolet wafer stepper," *Proc. SPIE's Santa Clara Symp. on Microlithography*, vol. 633, pp. 6-16, 1986.
- [3] M.D. Levenson, N.S. Viswanathan, R.A. Simpson, "Improving Resolution in Photolithography with a Phase-Shifting Mask," *IEEE Transactions on Electron Devices*, Vol. Ed-29, No. 12, pp. 1812-1846, December 1982.
- [4] Satori Asai, Isamu Hanyu, and Kohki Hikosaka, "Improving projection lithography image illumination by using sources far from the optical axis," *J. Vac. Sci. Technol. B* 9(6), Nov/Dec 1991, pp. 2788-2791.
- [5] H. Fukuda, T. Terasawa, and S. Okazaki, "Spatial filtering for DOF and resolution enhancement in optical lithography," *J. Vac. Sci. Technol. B* 9, p. 3113 (1991).
- [6] H. Jinbo, Y. Yamashita, M. Saalamura, "Subhalf-Micron Patterning of Negative Working Resist by Using New Phase-Shifting Mask," *The 34th International Symposium on Electron, Ion, and Photon Beams*, 1990.
- [7] K.K.H. Toh, G. Dao, R. Singh, H. Gaw, "Chromeless Phase-Shifted Masks: A New Approach to Phase-Shifting Masks," *BACUS 10th Annual Symposium on Microlithography*, vol 1496, 1990.
- [8] H. Jinbo and Y. Yamashita, "Improvement of phase-shifter edge line mask method," *Japanese Journal of Applied Physics*, vol. 30, 2998 (1991).
- [9] Y. Yanagishita et al., "Phase-shifting photolithography applicable to real IC patterns,"

- SPIE Proceedings, vol. 1463, p. 207 (1991).
- [10] T. Terasawa, N. Hasegawa, T. Kurosaki, T. Tanaka, "0.3 micron Optical Lithography Using a Phase-Shifting Mask," *SPIE Proceedings*, vol. 1088, p. 25, 1989.
- [11] B.J. Lin, "The attenuated PSM," *Solid State Tech.*, Jan. 1992, p. 43.
- [12] B.J. Lin, "Phase-Shifting and Other Challenges in Optical Mask Lithography," *BACUS 10th Annual Symposium on Microlithography*, vol. 1496, 1990.
- [13] S. Matsuo, K. Komatsu, Y. Takeuchi, E. Tamechika, Y. Mimura, K. Harada, "High resolution optical lithography system using oblique incidence illumination," Intl. Electron Devices Meeting (IEDM), pp. 970-972, Dec. 1991.
- [14] Satoru Asai, Isamu Hanyu, and Kohki Hikosaka, "High performance optical lithography using a separated light source," *J. Vac. Sci. Technol. B* 10(6), Nov/Dec 1992, pp. 3023-3026.
- [15] N. Shiraishi, et al., "New Imaging Technique for 64M-DRAM," *SPIE Optical/Laser Microlithography V*, Vol. 1674, pp. 741, March 1992.
- [16] M. Noguchi, et al., "Subhalf Micron Lithography System with Phase-Shifting Effects," *SPIE Optical/Laser Microlithography V*, Vol 1674, pp. 92, March 1992.
- [17] K. Kamon, et al., "Photolithography System Using Annular Illumination," *Japanese Journal of Applied Physics*, Vol. 30, No. 11B, pp. 3021-3029, Nov. 1991.
- [18] A. Yen, et al., "0.25 μ m Lithography Using a Deep-UV Stepper with Annular Illumination," *Microelec. Eng.*, (*Proceedings of Microcircuit Engineering 92, Erlangen, Germany*), 1992.
- [19] K. Tounai, et al., "Resolution Improvement with Annular Illumination," *SPIE Optical/Laser Microlithography V*, Vol. 1674, pp. 753-764, March 1992.
- [20] W.N. Partlo, P.J. Tompkins, P.G. Dewa, P.F. Michaloski, "Depth of Focus and Resolution Enhancement for i-line and deep-UV Lithography Using Annular Illumina-

- tion," *SPIE Optical/Laser Microlithography VI*, pp. 137-157, March 1992.
- [21] Kazuya Kamon, Teru Miyamoto, Yasuhito Myoi, Hitoshi Nagata, Masaaki Tanaka, and Kazuo Horie, "Photolithography System Using Annular Illumination," *Japanese Journal of Applied Physics*, Vol. 30, No. 11B, November 1991, pp. 3021-3029.
- [22] C. Mack, "Simple method for rim shifter design: the biased self-aligned rim shifter," *1992 BACUS Symposium on Photomask Technology*, Vol. 1809, 1992.
- [23] D. M. Newmark, E. Tomacruz, S. Vaidya, A.R. Neureuther, "Investigation of Proximity Effects for a Rim Phase-Shifting Mask Printed with Annular Illumination," *SPIE: Optical/Laser Microlithography VII*, March 1994.
- [24] K.K.H. Toh, "Two Dimensional Images with Effects of Lens Aberrations in Optical Lithography," *M.S. Thesis*, University of California, Berkeley, 1988.
- [25] K.K.H. Toh, G. Dao, H. Gaw, A.R. Neureuther, and L. Fredrickson, "Design Methodology for Dark-Field Phase-Shifted Masks," *SPIE Optical/Laser Microlithography IV*, pp. 402-413, March 1991.
- [26] Technology Modeling Associated, Inc, Palo Alto, CA.
- [27] C.A. Spence, D.C. Cole, and B.A. Peck, "Using multiple focal planes to enhance the depth of focus," *SPIE Optical/Laser Microlithography V*, March 1992.
- [28] J.G. Garofalo, R.L. Kostelak, "Phase-Shifting Structures for Isolated Features," *SPIE Optical/Laser Microlithography IV*, pp. 151-166, March 1991.
- [29] D.M. Newmark and A.R. Neureuther, "Phase-Shifting Mask Design Tool," *BACUS Photomask Technology*, 1991.
- [30] D.M. Newmark and A.R. Neureuther, "Computer Aided Design Tool for Phase-Shifting Masks," *SPIE Optical/Laser Microlithography V*, March 1992.

Chapter 3 Evaluating Resolution Enhancement Techniques

3.1 Introduction

Phase-shifting masks (PSM) and off-axis illumination are beneficial for enhancing the depth of focus of some features on a mask but not for others. For example, annular illumination and strong PSM approaches, such as the alternate aperture phase-shift mask can improve the depth of focus of dense or tightly packed features by a factor of two. Weak PSM, such as the rim PSM, can be used to improve all types of features, but the technique only marginally increases the depth of focus for dense features. Another related problem is that most phase-shifting mask techniques require proximity correction to prevent dense and isolated features from printing with widely different critical dimensions [1].

The goal of this chapter is to address these concerns by developing automated techniques to determine the bias for a particular phase-shifting mask approach and to evaluate a variety of resolution enhancement techniques to find ones which may have broad applicability for random logic masks. With this goal in mind, a computer aided design system has been created to analyze and bias phase-shift masks for one-dimensional features. The system relies on aerial image simulation and exposure versus defocus plots [2] (exposure vs. defocus plots or E-D trees are explained below). The fundamental assumption behind this system is that depth of focus and bias information can be obtained by the intersection of multiple E-D trees. For instance, if two E-D trees overlap, the features should print with the target critical dimension at some exposure [3,4]. Design charts summarizing the trade-offs can be created from a few thousand SPLAT runs.

3.2 E-D Trees

E-D trees are graphs constructed from a sequence of aerial image simulations through focus that enable one to view several image characteristics on a single plot. An example

of through focus images and the corresponding E-D tree is shown in Fig. 3.1, for a $0.5\mu\text{m}$ dense line and space pattern imaged at $\lambda/\text{NA} = 1$. The E-D tree is calculated based on a $\pm 10\%$ critical dimension (CD) tolerance, $\pm 10\%$ in the example. The left branch of the E-D tree uses the -10% CD or $0.45\mu\text{m}$. On each aerial image, we extract the intensity (I) corresponding to this CD and plot the point $(\ln(1+I), \text{defocus})$ on the graph. The right branch is constructed in the same way, but it uses $+10\%$ CD or $0.55\mu\text{m}$. Since intensity and $\ln(1+I)$ are proportional to the exposure, this graph is an exposure versus defocus plot and commonly called an E-D tree [2].

Construction of E-D Trees

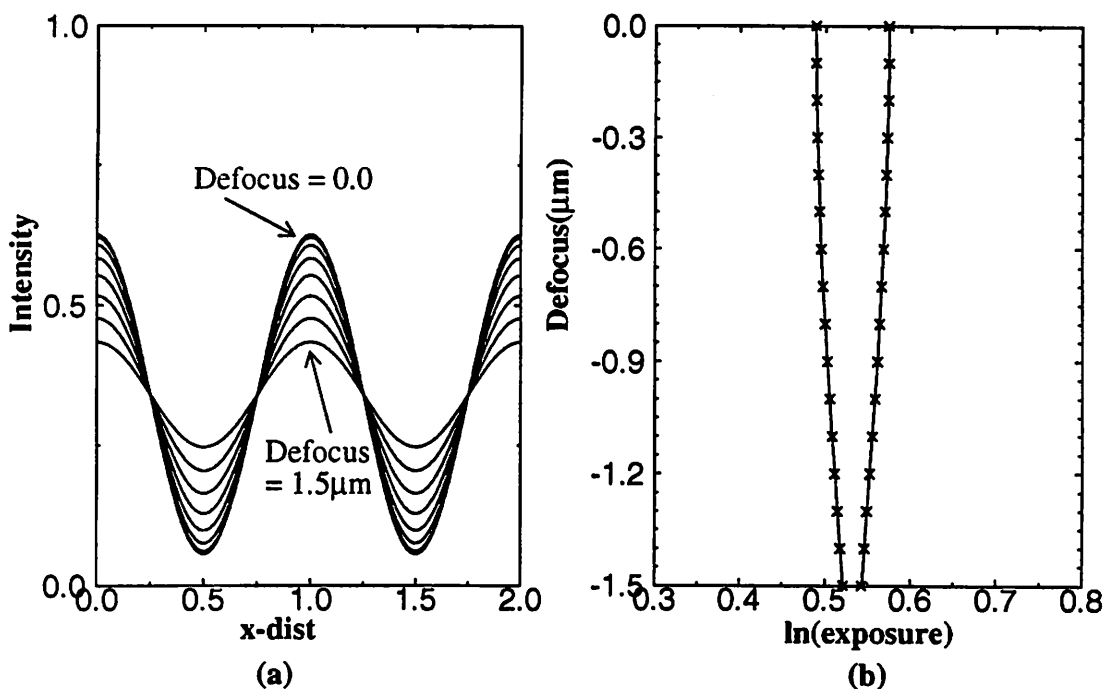


Figure 3.1. (a) Aerial images of $0.5\mu\text{m}$ line and space pattern through focus with $\lambda/\text{NA} = 1.0$ and 0.5σ . (b) E-D tree constructed from aerial images. A $\pm 10\%$ CD variation is used to plot the left and right branches of the E-D tree.

An E-D tree allows one to extract the depth of focus based on a specified exposure latitude. For instance, an exposure latitude of 20% corresponds to a constant x-distance on the graph. If a rectangle is constructed to just fit within both branches of the E-D tree and

its x-dimension is equal to the exposure latitude, the y-dimension is one-half of the total depth of focus of the feature. The exposure at the center of this rectangle is considered to be the nominal exposure, or the exposure required to obtain features with the target dimension, $0.5\mu\text{m}$ in this example. Any exposure or defocus within the rectangle will lead to features which have dimensions within the $\pm 10\%$ tolerance. Since E-D trees can conveniently summarize the depth of focus and nominal exposure, we use them throughout the next two chapters to evaluate resolution enhancement techniques and bias the features to correct proximity effects.

3.3 Design Rule Generation (DRGEN)

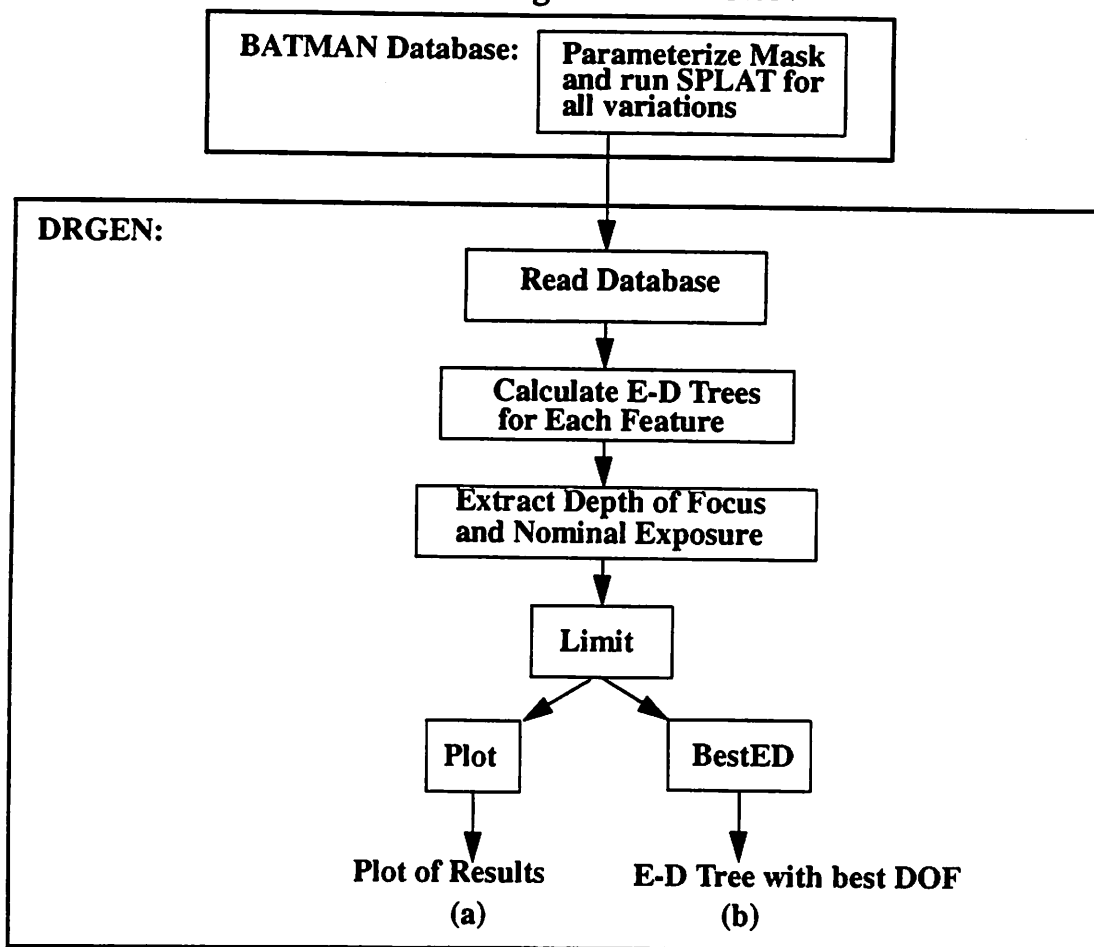
Designing a phase-shift mask technology for masks with random logic requires extensive evaluation of candidate approaches to determine the performance characteristics. The initial evaluation can be done at a fixed bias for binary intensity or chrome masks (BIM), attenuating masks, and annular illumination, since it is not initially necessary to find the bias for a fixed nominal exposure. After the candidate system is chosen, design of the actual bias required to achieve better process control necessitates pattern dependent biasing. Biasing is required so all features print with the desired critical dimension within a given exposure-defocus window. The need to quickly and automatically perform both these functions led us to develop DRGEN (Design Rule GENERator). The system allows the user to perform an evaluation of different phase-shifting techniques and then bias the chosen scheme to optimize the exposure-defocus window for all features.

Path (a) in the block diagram of Fig. 3.2 shows how the initial evaluation of a phase-shift technique is accomplished. First, Batman is used to create a database of aerial images of equal width lines or spaces at varying pitch. These aerial images are read by DRGEN, which calculates the E-D trees from a user defined critical dimension and $\pm\%$ CD tolerance and extracts the depth of focus based on the exposure latitude. In the limit

step, certain records are eliminated due to poor performance, such as large side-lobes. Then, the plot command is used to produce a graph of the period versus depth of focus. For most phase-shift features, the depth of focus extracted from the E-D trees is not critically dependent on the bias if the exposure level is allowed to vary. However, for certain techniques, such as the rim phase-shift mask, each feature must be individually biased to obtain the maximum depth of focus. This requires an initial database with a parameterized bias for each feature and the plot command cannot be used directly. The bestED command, path (b), is then used to find the E-D tree and corresponding bias with the largest depth of focus.

The need for biasing features to optimize the depth of focus for the chosen phase-shift method is illustrated in Fig. 3.3 and Fig. 3.4. Fig. 3.3a and 3.3b are the masks used in this example. Fig. 3.4a shows the E-D trees for alternate aperture dense lines and spaces with CD of $0.35\mu\text{m}$ and $\pm 10\%$ CD control. The image simulations use a wavelength of 365nm , 0.5 NA, and 0.5 partial coherence. The mask is biased from $0.3\mu\text{m}$ to $0.4\mu\text{m}$ to generate the ten E-D trees shown for this feature. Note that the E-D trees shift to the right as the bias on the mask is increased, which indicates a change in the nominal exposure is needed to obtain the desired critical dimension for the feature. Fig. 3.4b is a similar graph, except the feature is a $0.35\mu\text{m}$ space with a pitch of $1.2\mu\text{m}$. The E-D trees show a similar behavior with bias; however, the nominal exposure level starts at a lower value. To print both these features at the same exposure level, it is necessary for the E-D trees to overlap. Fig. 3.4c shows the overlapping E-D trees for the case where the bias on both features is identical. Note that the area of overlap is very small which implies that the effective exposure latitude and depth of focus are negligible. An improvement is achieved by biasing the dense lines differently from the more isolated ones. The result of biasing the mask in this way is shown in Fig. 3.4d. The overlap of the E-D trees is much larger which indicates an increase in the depth of focus for printing both features together.

Block Diagram of DRGEN



| Command | Function |
|---------|----------------------------------------------------------------------------------------------------------------------------------------------|
| bestED | Check every E-D tree of a particular feature and return the one which has the best depth of focus. |
| limit | Eliminate E-D trees which are unacceptable for some reason, such as having side-lobe intensity above the 30% level. |
| plot | Plot various parameters calculated by DRGEN (such as depth of focus or nominal exposure) as a function of a parameterization of the feature. |

Figure 3.2 Block diagram of DRGEN. The main database is created by Batman. It is read into DRGEN, which constructs E-D trees and extracts depth of focus and nominal exposure. The limit step removes any unacceptable E-D trees. There are two main analysis paths after the limit command. (a) The plot command will graph image quality metrics such as depth of focus versus the mask parameters. (b) The bestED command calculates the bias which gives the largest E-D window.

Alternate Aperture Phase-Shifting Masks Used to Show Proximity Effect

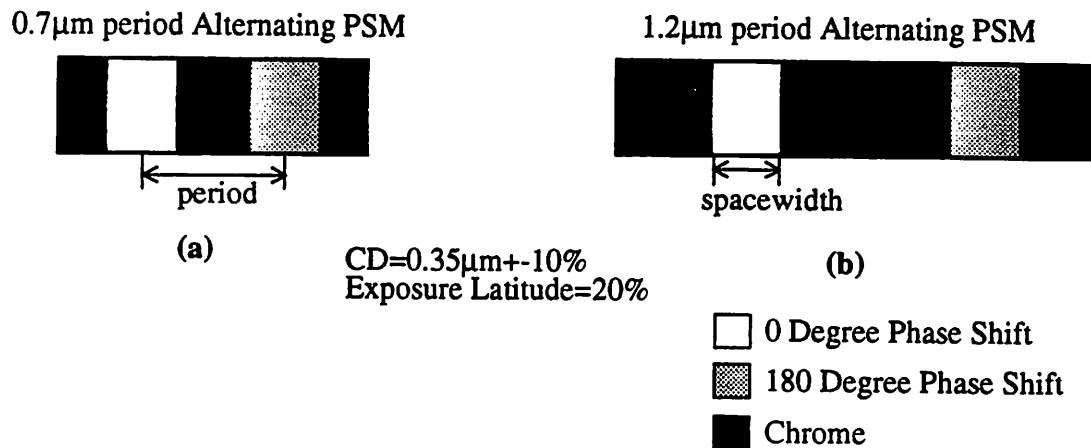


Figure 3.3 (a) Mask of 0.35 μm dense lines and spaces. (b) Mask of 0.35 μm spaces at a period of 1.2 μm .

Finding the optimum bias to achieve this result is somewhat tedious since it is necessary to compare all overlaps of the E-D trees to find the combination which gives the largest overall depth of focus. DRGEN automates the process by extracting the correct biases to obtain overlapping E-D trees. The method is shown in Fig. 3.5. The diagram is similar to Fig. 3.2, except the optimumED command is chosen after the limit step. As before, the first step is to generate a database which contains the bias parameterization for the features. The E-D trees are then calculated and the depth of focus and nominal exposure are extracted. After the limit step, the optimumED command checks all combinations of overlaps for up to three features and outputs the largest E-D tree intersection for them. The bias results are recorded and the E-D tree intersection is fed forward to the next step where optimumED finds the E-D trees for each remaining feature which best overlap the current E-D tree. The bias is output again and the result from the intersection continues to be fed forward to each successive optimumED command until all features are biased.

A simple example using the two alternate aperture features described above should clarify this methodology. As explained earlier, Fig. 3.4a is a plot of the set of E-D trees for

E-D Trees for $0.35\mu\text{m}$ Lines and Spaces at Two Periods, $0.7\mu\text{m}$ and $1.2\mu\text{m}$, Using the Alternate Aperture Mask

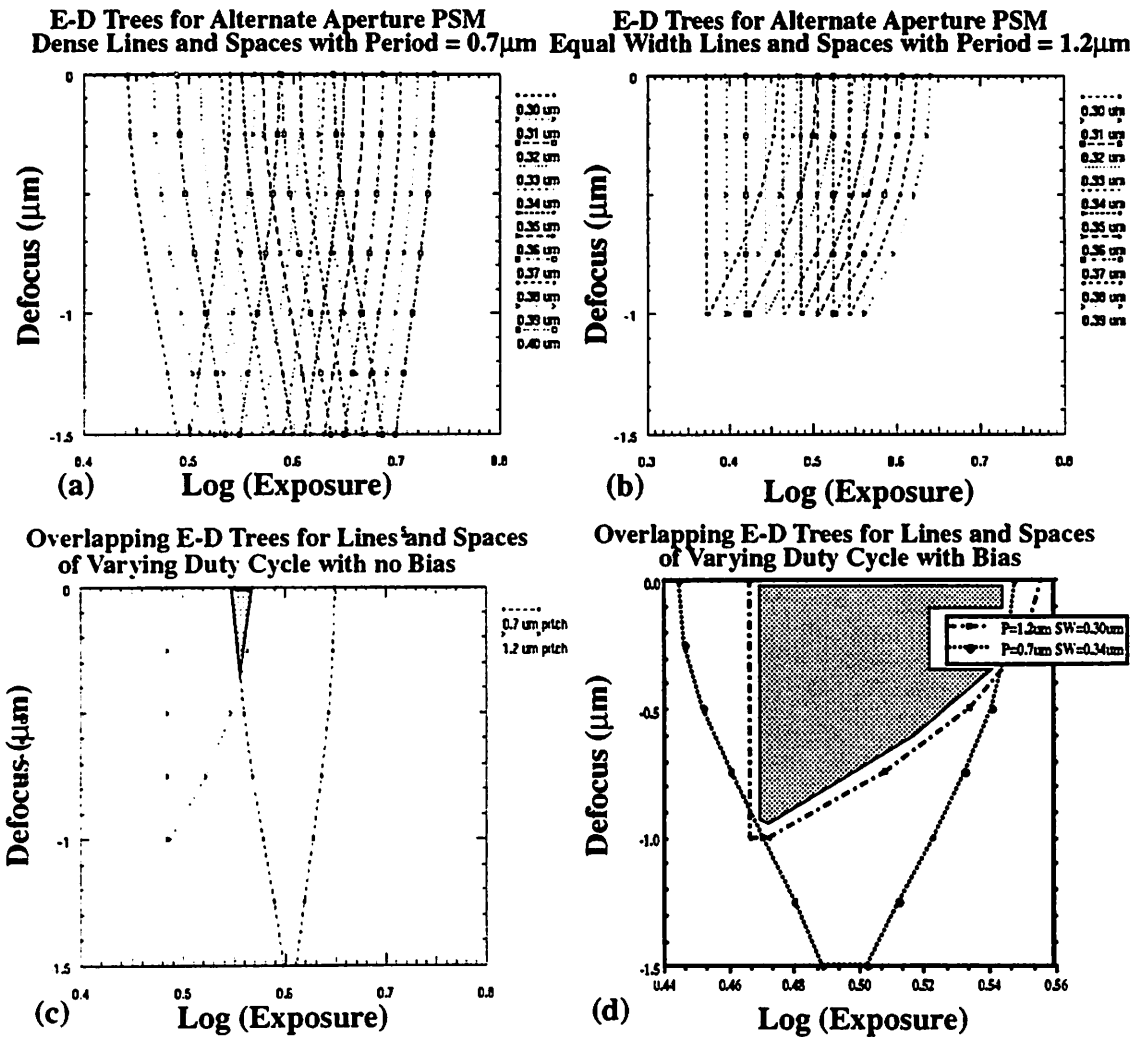
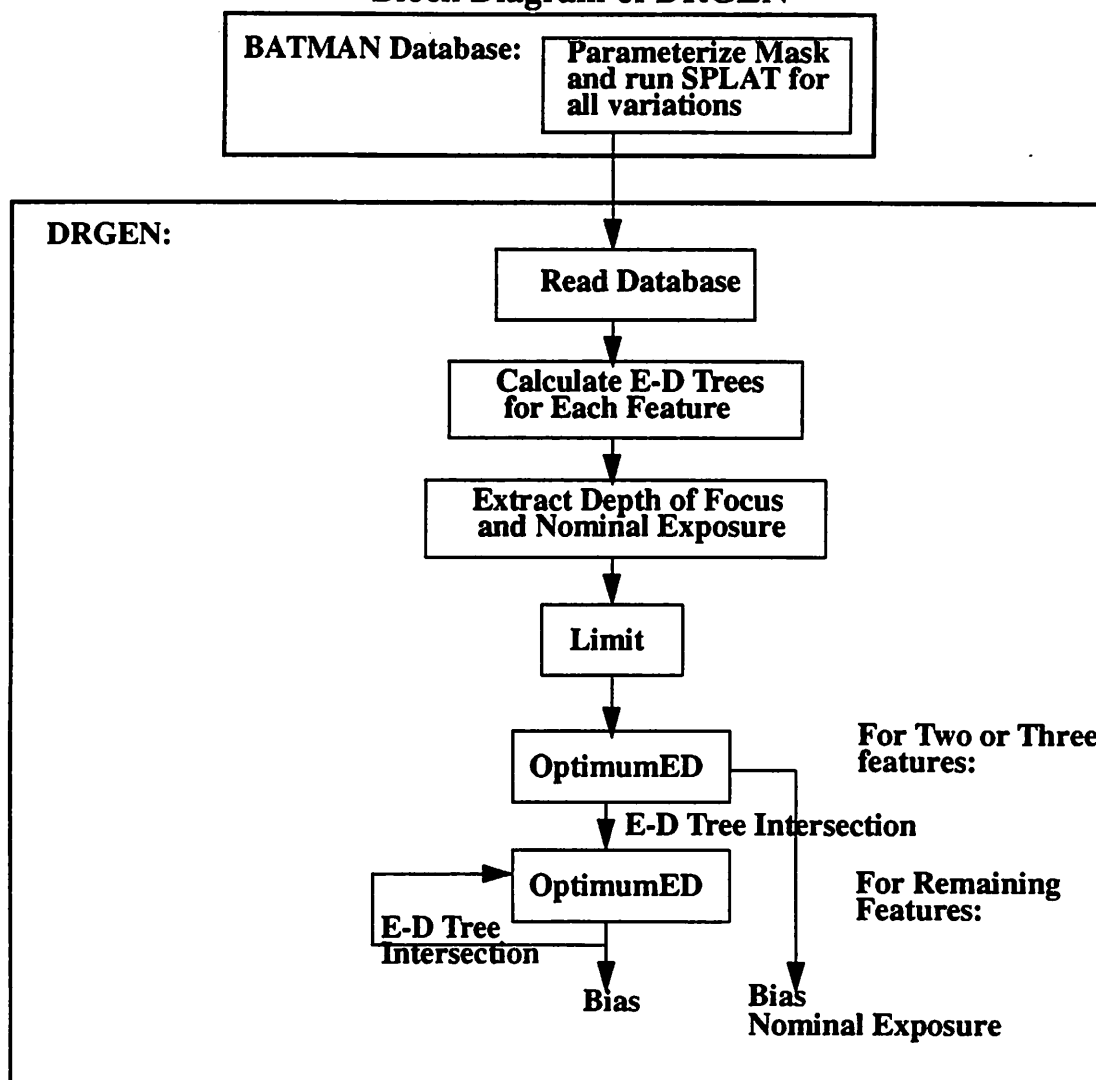


Figure 3.4 Methodology for biasing phase-shift masks using overlapping E-D trees. (a) E-D trees for $0.35\mu\text{m}$ dense lines and spaces in which the space width on the mask is biased from $0.3\mu\text{m}$ to $0.4\mu\text{m}$. (b) E-D trees for mask with $0.35\mu\text{m}$ spaces at a period of $1.2\mu\text{m}$ with space width biased from $0.3\mu\text{m}$ to $0.4\mu\text{m}$. (c) E-D trees for a fixed bias on both features. (d) E-D trees for optimum bias on each feature. Note that the E-D window for optimum bias is much larger than the one for a fixed bias. I-line illumination with $NA = 0.5$ and partial coherence of 0.5 . E-D trees use $\pm 10\%$ CD tolerance.

Block Diagram of DRGEN



| Command | Function |
|-----------|--------------------------------------------------------------------------------------------------------------------------------------------------------------------|
| optimumED | Overlap all the E-D trees among two or three features and pick the biases which give an overlap that has the largest depth of focus for a given exposure latitude. |

Figure 3.5 Block diagram of DRGEN. The main database is created by Batman. It is read into DRGEN, which constructs E-D trees and extracts depth of focus and nominal exposure. The limit step removes any unacceptable E-D trees. The optimumED command calculates the bias needed to obtain overlapping E-D trees.

printing $0.35\mu\text{m}$ dense lines and spaces while Fig. 3.4b is a set of E-D trees for printing $0.35\mu\text{m}$ spaces in positive resist at a period of $1.2\mu\text{m}$. Again, the aerial image simulations use a wavelength of 365nm , NA of 0.5 , and partial coherence of 0.5 . The E-D trees were all generated assuming $\pm 10\%$ CD control. DRGEN can calculate the bias of both features, the optimum resulting E-D tree, and the corresponding nominal exposure and depth of focus for a particular exposure latitude. With the analysis method above, in which optimumED is used to calculate the overlap of all possible combination of the E-D trees for both features, we find that a $-0.01\mu\text{m}$ bias on the dense lines and spaces and a $-0.05\mu\text{m}$ bias on the other feature give the optimum depth of focus of $\pm 0.75\mu\text{m}$. The optimum overlapping E-D trees are illustrated in Fig. 3.4d.

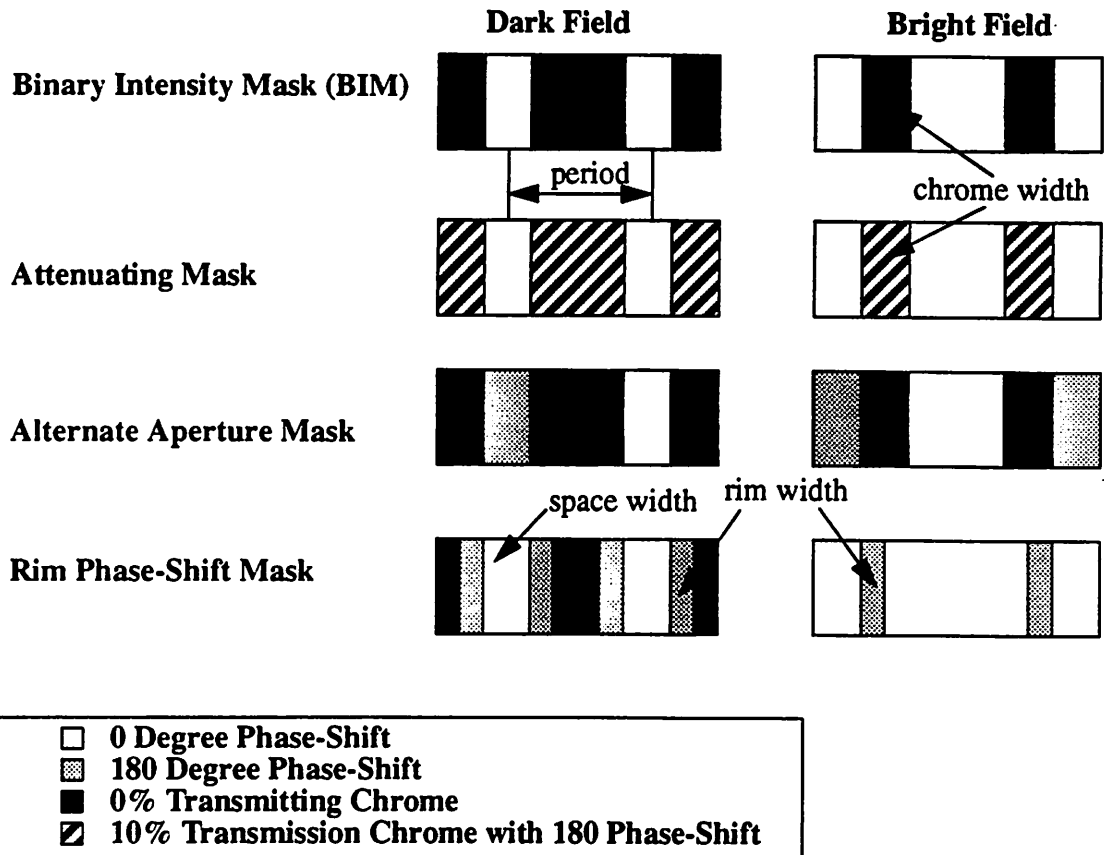
3.4 Initial Evaluation of Resolution Enhancement Techniques

3.4.1 Introduction

As discussed in the description of DRGEN, there are two steps to our design procedure; the first step is the evaluation of different lithography enhancement techniques. The initial simulations are aimed at finding a method which is capable of printing bright and dark field constant width lines and spaces of varying duty cycle that have the largest minimum depth of focus. This criteria translates into finding a technique which reduces the dead zone effect, a point of low depth of focus performance. If such a phase-shift technique, illumination method, or combination exists, it may be useful for random logic designs, which require more than just dense and isolated lines and spaces. The SPLAT aerial image simulations assume i-line illumination, NA of 0.5 , and partial coherence of 0.5 . The E-D trees generated from these aerial images have a CD of $0.35\mu\text{m} \pm 7.5\%$. The depth of focus is calculated at 20% exposure latitude. The phase-shift and illumination types under investigation are shown in Fig. 3.6. A binary intensity mask, attenuating mask, alternate aperture, and rim PSM are considered. These mask types are simulated with both conventional and annular illumination. However, the combination of annular

illumination and an alternate aperture phase-shift mask is not considered since it degrades the depth of focus.

Phase-Shift Masks and Illumination System Studied using Simulation



Illumination Systems



Figure 3.6 The four masks studied with SPLAT simulations are: binary intensity mask, attenuating mask, alternate aperture PSM, and rim PSM. These masks are studied with conventional and annular illumination systems.

3.4.2 Conventional and Alternate Aperture

Fig. 3.7 shows the depth of focus of bright and dark field lines and spaces for conventional and alternate aperture masks with conventional illumination ($\sigma=0.5$). Since biasing does not improve the depth of focus at 20% exposure latitude if the exposure level is not fixed, all features are unbiased. The results of these simulations for a conventional mask clearly illustrate the decrease in the depth of focus for bright field lines of increasing period. This problem is alleviated by phase-shifting which gives a twofold improvement in the depth of focus for bright field features. However, there exists a dead zone at which the depth of focus is reduced 40% from its nominal clear field value. As expected, there is no increase in the depth of focus for dark field features with this phase-shift scheme.

Depth of Focus vs. Period for Alternate Aperture and BIM with Equal Lines and Spaces of Varying Duty Cycle ($CD = 0.35\mu\text{m}$)

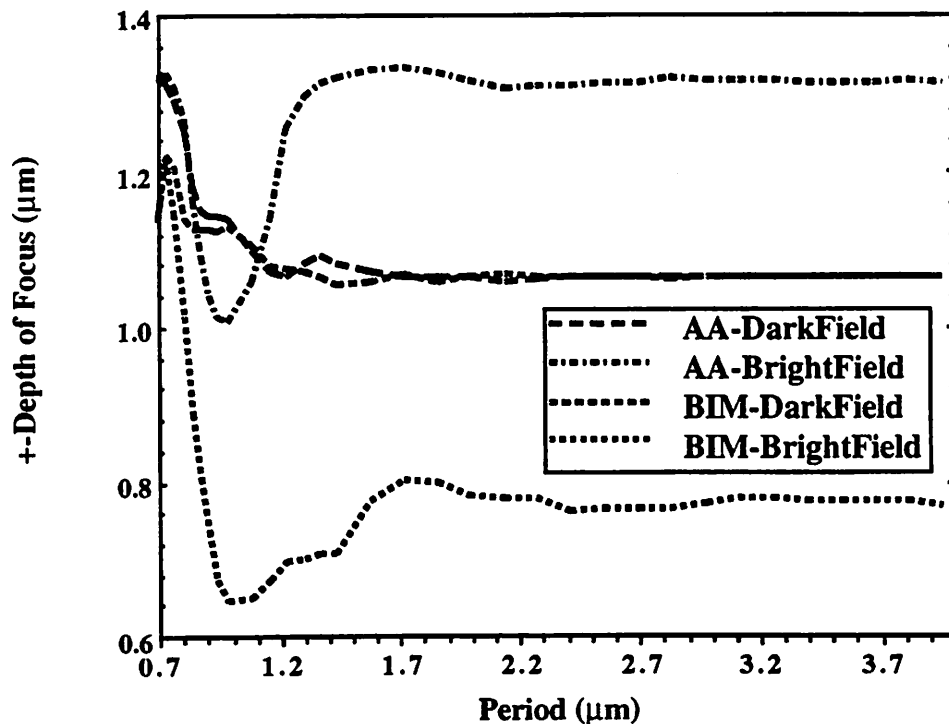


Figure 3.7 Depth of focus for 0.35μm lines and spaces of varying period for alternate aperture and BIM. Simulations are done at i-line with NA=0.5 and partial coherence of 0.5.

3.4.3 Rim and Attenuating

The graph in Fig. 3.8 illustrates the depth of focus for rim and attenuating masks. As a first attempt, the attenuating mask is biased by $0.05\mu\text{m}$ to improve the depth of focus; the rim width on the rim PSM was individually optimized for each feature since the depth of focus is very sensitive to the rim width. Both these PSM techniques show promising results, especially for dark field features; they have at least a 20% improvement in the depth of focus for the dark field patterns. However, the improvement for bright field features is negligible compared to a conventional mask. The failure of an attenuating mask to increase the depth of focus for bright field features can be understood by recognizing the distributed contribution from large attenuating areas to the feature of interest. For example, the mask needed to produce an isolated line in positive resist would have a thin chrome line on the mask which, for small features, intuitively leads to less image enhancement at the edges. The rim mask also fails to increase the depth of focus for bright field features. Finally, for both these techniques, the depth of focus in the dead zone is 20% lower than the depth of focus for an isolated feature.

3.4.4 Annular Illumination

Annular illumination is a promising technique for increasing the depth of focus for high frequency patterns; however, when it is applied to equal lines or spaces of varying duty cycle, there are problems. As illustrated in Fig. 3.9a, a plot of bright field constant width line and space patterns of increasing period for several annulus positions, the minimum depth of focus is not improved over the conventional case regardless of the annulus position. The behavior for dark field lines of constant CD and increasing period, shown in Fig. 3.9b, is more promising, but the depth of focus only recovers to the value for conventional illumination. Here again, the depth of focus in the dead zone is lower than the depth of focus for isolated features.

Depth of Focus vs. Period for Rim PSM and Attenuating Mask with Equal Lines or Spaces of Varying Duty Cycle (CD = $0.35\mu\text{m}$)

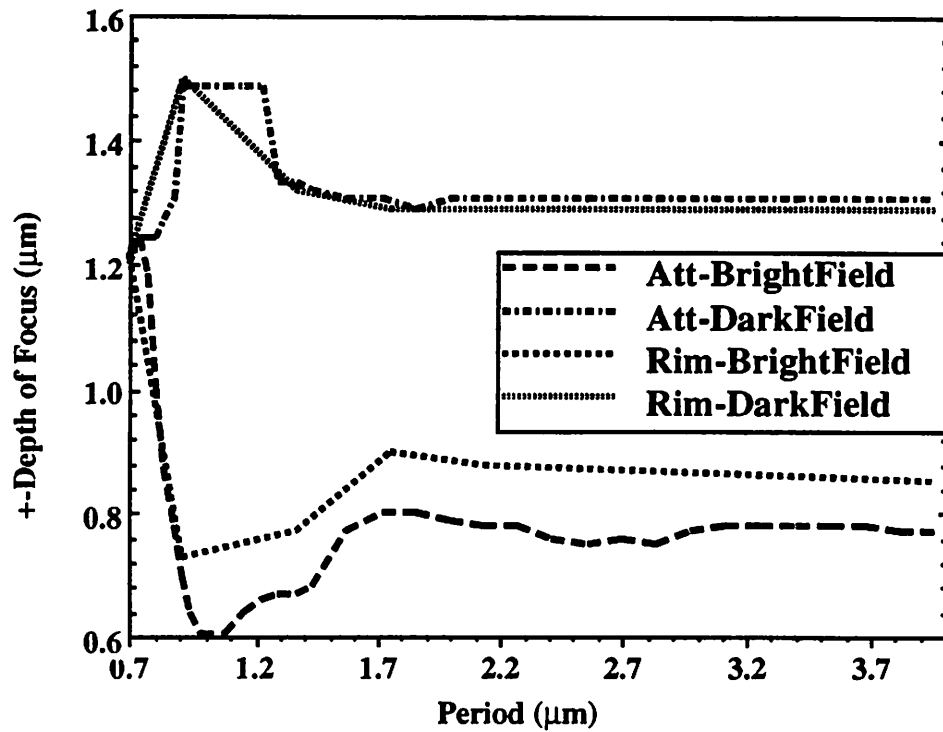
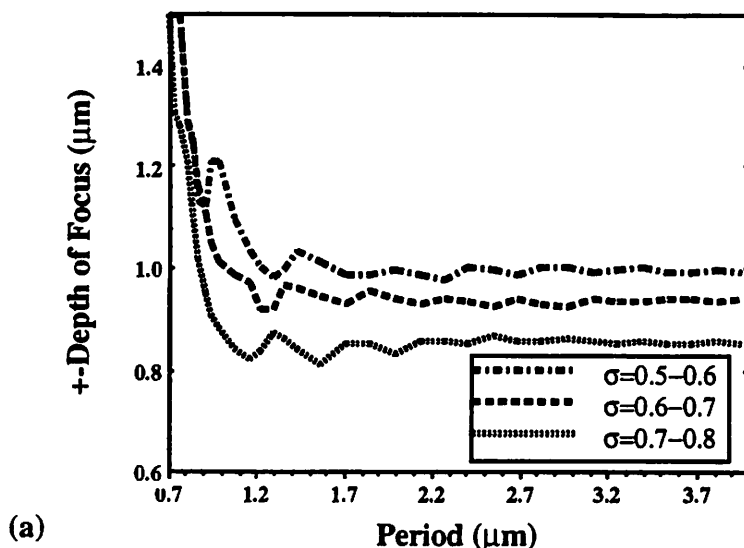


Figure 3.8 Depth of focus for $0.35\mu\text{m}$ lines and spaces of varying period for a rim PSM and Attenuating Mask. Simulations are done at i-line with $\text{NA}=0.5$ and partial coherence of 0.5.

Depth of Focus vs. Period for Dark Field BIM with Equal Lines or Spaces of Varying Duty Cycle (CD = 0.35 μ m)



Depth of Focus vs. Period for Bright Field BIM with Equal Lines or Spaces of Varying Duty Cycle (CD = 0.35 μ m)

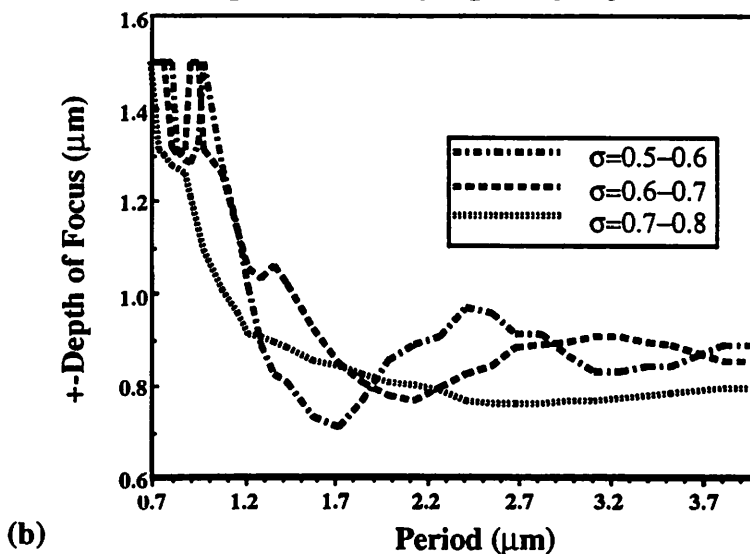


Figure 3.9 Depth of focus for (a) 0.35 μ m lines and (b) 0.3 μ m spaces of varying period for a binary intensity mask with annular illumination. The annulus positions are $\sigma=0.5-0.6$, $\sigma=0.6-0.7$, and $\sigma=0.7-0.8$. The best annulus for dark field is $\sigma=0.5-0.6$, but the best one for bright field is $\sigma=0.7-0.8$: a compromise is necessary if both features occur on the same mask. Simulations use i-line with NA=0.5.

3.4.5 Attenuating Mask with Annular Illumination

In the case of annular illumination with an attenuating mask (not shown), the depth of focus improves by 50% in the bright field over a binary intensity mask with conventional illumination when the annulus is located from 0.7 to 0.8. In the dark field, the depth of focus can also be improved to $\pm 1.0\mu\text{m}$, but the annulus must be 0.5 to 0.6. Thus, some compromise is required to print both types of features and the overall depth of focus improvement will be less.

3.4.6 Rim PSM with Annular Illumination

The results for the attenuating case and the intuition that a rim PSM improves isolated features while an annulus improves dense ones, led us to explore the improvement in depth of focus for annular illumination with a rim phase-shift mask. As shown in Fig. 3.10, the technique improves the bright field depth of focus for more isolated lines and spaces without sacrificing the depth of focus for dense lines and spaces. In fact, for an annulus location of $\sigma = 0.6$ to 0.7 , the depth of focus is greater than $\pm 0.9\mu\text{m}$ for both bright and dark field features. Note that the dead zone depth of focus is improved by 30% over the depth of focus for a rim phase-shift mask with conventional illumination.

3.4.7 Summary

Table 3.1 summarizes the results of the simulation studies for the various phase-shift mask techniques. The table lists the minimum depth of focus for bright and dark field features as well as the depth of focus for dense lines and spaces. Overall, most methods performed well for dense features. The rim and attenuating masks have the least depth of focus increase. The minimum depth of focus measurements distinguish the candidates better. Considering the values alone, the alternate aperture approach looks most promising with large depth of focus for both bright and dark field features although it offers no improvement over a conventional mask for dark field features. Our choice to pursue other

**Depth of Focus vs. Period for Rim PSM and Annular Illumination
for Equal Lines or Spaces of Varying Duty Cycle (CD = 0.35 μ m)**

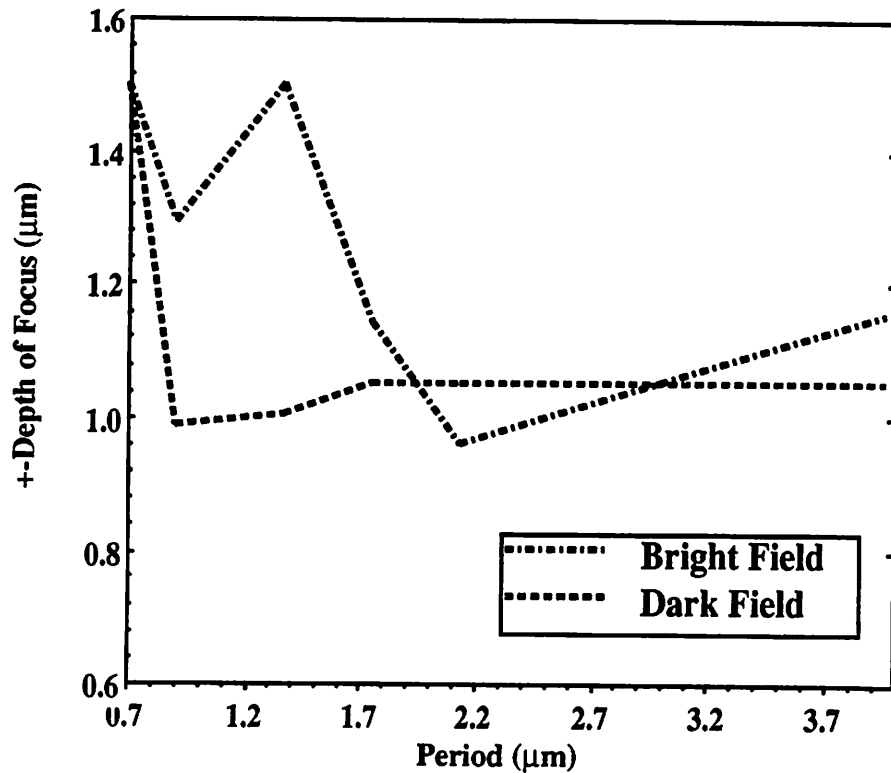


Figure 3.10 Depth of focus for 0.35 μ m lines and 0.35 μ m spaces of varying period for a rim PSM with annular illumination. $\lambda = 365$ nm, NA=0.5, and $\sigma = 0.6-0.7$

methods arises from the difficulty experienced applying this phase-shift technique to non-regular masks. Among the other contenders, the attenuating and rim phase-shift mask with annular illumination are the best ones since they improve the depth of focus for bright field most effectively while only suffering a slight decrease in the dark field. Our choice of a rim phase-shift mask was motivated by a greater knowledge base in mask fabrication and by the slight advantage in bright field depth of focus, which indicates that this technique will have a more uniform depth of focus for all features.

TABLE 3.1. Summary of depth of focus results for initial simulation studies

| Mask and Illumination System | Minimum Depth of Focus ($\pm\mu\text{m}$) | | Depth of Focus for Dense Lines and Spaces |
|-------------------------------------|-------------------------------------------------------------|-------------------|--------------------------------------------------|
| | Bright Field | Dark Field | |
| Binary Intensity Mask | 0.65 | 1.1 | 1.1* |
| Alternate aperture | 1.0 | 1.1 | 1.3 |
| Rim Phase-Shift Mask | 0.75 | 1.2 | 1.2 |
| Attenuating Mask | 0.6 | 1.2 | 1.2 |
| Annular Illumination | 0.75 | 0.95 | 1.5 |
| Att Mask + Annulus | 0.85** | 1.0** | 1.5 |
| Rim PSM + Annulus | 0.95 | 1.0 | 1.5 |

* Simulation overestimates the depth of focus for dense lines and spaces with the binary intensity mask as discussed later.

** The annulus for bright field is 0.7-0.8 and dark field is 0.5-0.6. A compromise would reduce the depth of focus somewhat for both cases if they occurred on the same mask.

References for Chapter 3

- [1] D.M. Newmark, J. Garofalo, S. Vaidya, "Aerial image based design of rim phase-shift mask with annular illumination," *SPIE: Optical/Laser Microlithography VI*, Vol. 1927, March 1993.
- [2] B.J. Lin, "Partially Coherent Imaging in Two Dimensions and the Theoretical Limits of Projection Printing in Microfabrication," *IEEE Trans. Electron Devices*, Vol. ED-27, pp. 931, 1980.
- [3] B.J. Lin, "A Comparison of Projection and Proximity Printings - from UV to X-Ray," *SPIE proceedings*, Vol. 1263, p. 80, 1990.
- [4] Ahmad D. Katnami and B.J. Lin, "Phase and transmission error study for the alternating-element (Levenson) phase-shifting mask." *SPIE Optical/Laser Microlithography III*, March 1990.

Chapter 4 Experimental Verification: Dead-Zones and Bias

4.1 Introduction

The initial goal of our experimental verification is to observe the dead zone effect, the low depth of focus performance observed in Chapter 3, and test the accuracy of the biases predicted by DRGEN. Since the chrome mask and rim phase-shift mask used with annular illumination show such dramatic differences in the depth of focus in the dead zone, these techniques are chosen for experimental evaluation. Ideally, the experimental results will allow us to show that the dead zone is a critically important aspect of off-axis illumination technology. Furthermore, if the biases from experiment agree with simulation, the bias design approach can also be validated.

4.2 Rim Phase-Shift Mask Design

Once the rim phase-shift mask with annular illumination is chosen as the resolution enhancement method, DRGEN is used to find the biases, nominal exposure, and depth of focus for a mask with the small set of constant width line and space features shown in Fig. 4.1. The mask is designed for a GCA DUV stepper with 0.48 NA, partial coherence of 0.45, and annular illuminator of 0.34 to 0.45. The target critical dimension for these particular features is $0.3\mu\text{m}$ ($k_1=0.58$), and the biases are designed for pitches of $0.6\mu\text{m}$, $0.8\mu\text{m}$, $1.0\mu\text{m}$ and $1.5\mu\text{m}$.

The optimum bias required to print all features at the same CD is calculated using DRGEN. As indicated in Chapter 3, the first step in this procedure is to parameterize each mask feature. Table 4.1 shows a subset of the rim widths for the bright field features. The actual simulations use more bias levels than the ones shown in the table. In the second step, all the records are read into DRGEN and the E-D trees for the features are calculated and stored in the internal data structure. Third, the limit command is used to eliminate all

Rim Phase-Shifting Mask Designed for Printing Bright and Dark Field Features

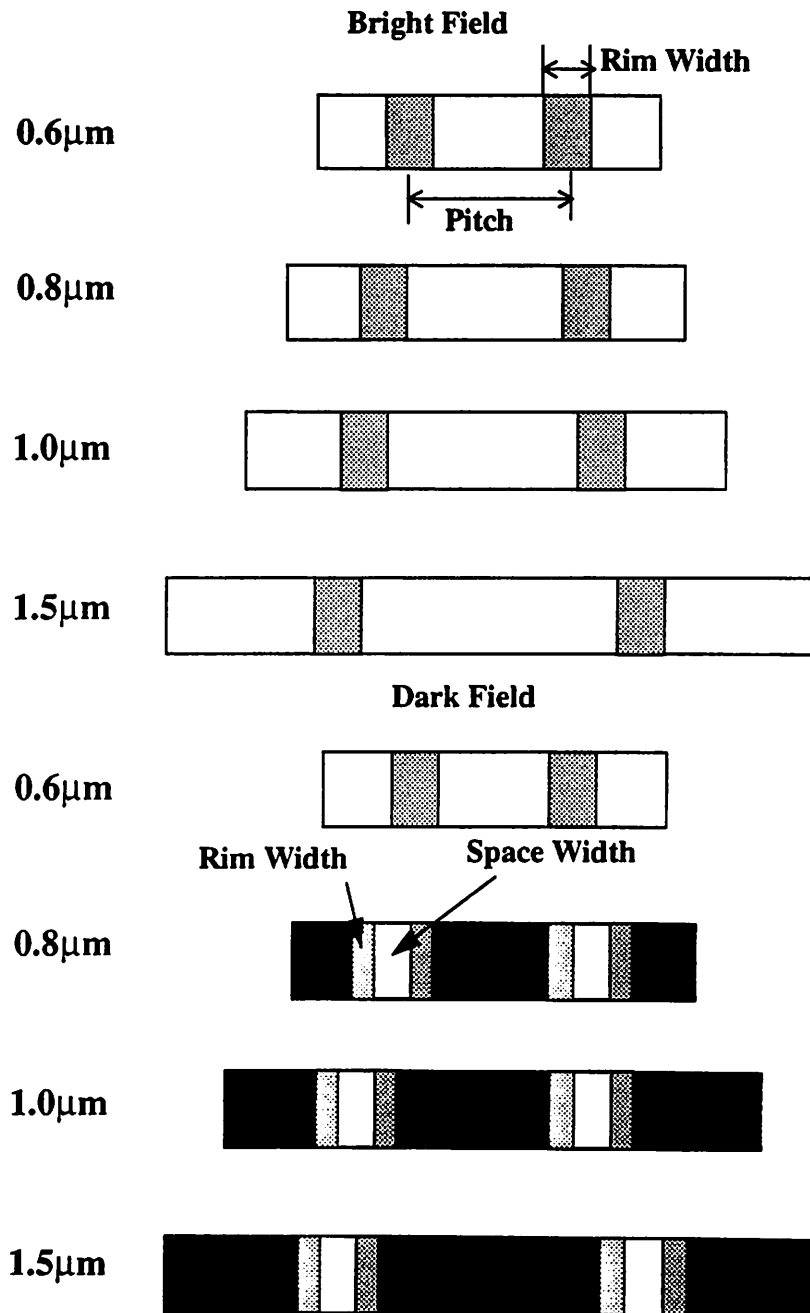


Figure 4.1 Bright and Dark Field Rim Phase-Shifting Mask Features. The CD equals 0.30μm for periods of 0.6μm, 0.8μm, 1.0μm, and 1.5μm. Space width and rim width are varied to bias each feature. The mask is designed for a GCA DUV stepper with $\lambda = 248\text{nm}$, 0.48 NA, and annular illumination of 0.34-0.45.

TABLE 4.1. Coded Rim Sizes for Bright Field Rim PSM Features.

| Feature | Rim Width (μm) | | | |
|---------|--------------------------------|--------------------------------|--------------------------------|--------------------------------|
| | Pitch = $0.6\mu\text{m}$ | Pitch = $0.8\mu\text{m}$ | Pitch = $1.0\mu\text{m}$ | Pitch = $1.5\mu\text{m}$ |
| A | 0.12 | 0.12 | 0.12 | 0.12 |
| B | 0.14 | 0.14 | 0.14 | 0.14 |
| C | 0.16 | 0.16 | 0.16 | 0.16 |
| D | 0.18 | 0.18 | 0.18 | 0.18 |
| E | 0.20 | 0.20 | 0.20 | 0.20 |

TABLE 4.2. Measured Rim Sizes for Bright Field Rim PSM Features.

| Feature | Rim Width (μm) | | | |
|---------|--------------------------------|--------------------------------|--------------------------------|--------------------------------|
| | Pitch = $0.6\mu\text{m}$ | Pitch = $0.8\mu\text{m}$ | Pitch = $1.0\mu\text{m}$ | Pitch = $1.5\mu\text{m}$ |
| A | 0.162 | 0.163 | 0.164 | 0.164 |
| B | 0.180 | 0.189 | 0.185 | 0.183 |
| C | 0.201 | 0.205 | 0.208 | 0.205 |
| D | 0.221 | 0.227 | 0.227 | 0.229 |
| E | 0.240 | 0.247 | 0.247 | 0.249 |

E-D trees in which the rim is large enough to cause side-lobe printing. To avoid checking all possible E-D tree overlaps, a combinatorial problem, we calculate the optimal overlap between two features, which sets the nominal exposure level and the bias for these features. Then, the biases for the remaining features, whose E-D trees overlap that optimum, are calculated. The final design has the biases and overlapping E-D trees shown in Fig. 4.2.

Based on these simulations, a mask was fabricated to study the accuracy of the predictions outlined above. Table 4.2 gives the measured dimensions of the features on the

ED Trees for Bright and Dark Field Lines and Spaces of Varying Duty Cycle for a Rim PSM with Annular Illumination (CD = 0.30 μ m for the Critical Feature)

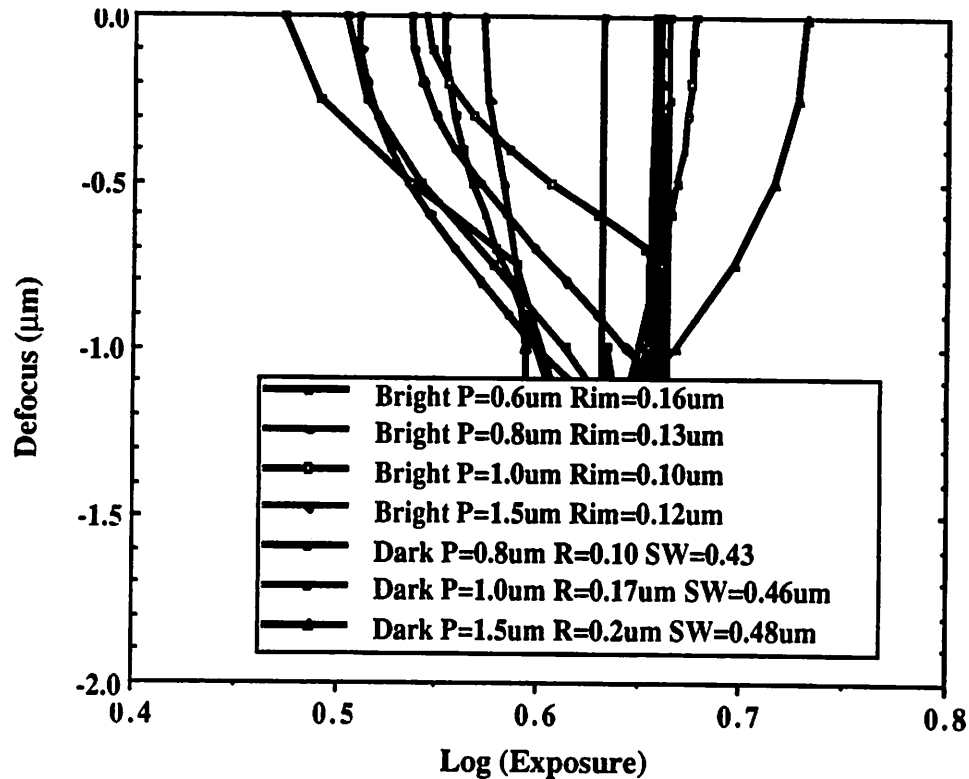


Figure 4.2 Overlapping E-D trees extracted with DRGEN for the bias design of a rim PSM with annular illumination. E-D trees assume 0.3 μ m \pm 7.5% CD control. $\lambda = 248$ nm, NA=0.48, $\sigma = 0.34$ -0.45.

mask. Conventional binary intensity mask patterns are also placed on the reticle. The rims on the reticle were laterally overetched due to an error in the fabrication. Also, note that the conventional mask patterns are etched 180 degrees into the quartz in this fabrication process. They are also over-etched so the space width on the mask for the four conventional bright field features is approximately 0.24 μ m.

4.3 Experimental Evaluation of Resist Lines Printed with Reticle

There are three important objectives in evaluating the performance of the reticle. The first objective is to experimentally verify our approach in choosing a phase-shift mask

TABLE 4.1. Coded Rim Sizes for Bright Field Rim PSM Features.

| Feature | Rim Width (μm) | | | |
|---------|--------------------------------|--------------------------------|--------------------------------|--------------------------------|
| | Pitch = $0.6\mu\text{m}$ | Pitch = $0.8\mu\text{m}$ | Pitch = $1.0\mu\text{m}$ | Pitch = $1.5\mu\text{m}$ |
| A | 0.12 | 0.12 | 0.12 | 0.12 |
| B | 0.14 | 0.14 | 0.14 | 0.14 |
| C | 0.16 | 0.16 | 0.16 | 0.16 |
| D | 0.18 | 0.18 | 0.18 | 0.18 |
| E | 0.20 | 0.20 | 0.20 | 0.20 |

TABLE 4.2. Measured Rim Sizes for Bright Field Rim PSM Features.

| Feature | Rim Width (μm) | | | |
|---------|--------------------------------|--------------------------------|--------------------------------|--------------------------------|
| | Pitch = $0.6\mu\text{m}$ | Pitch = $0.8\mu\text{m}$ | Pitch = $1.0\mu\text{m}$ | Pitch = $1.5\mu\text{m}$ |
| A | 0.162 | 0.163 | 0.164 | 0.164 |
| B | 0.180 | 0.189 | 0.185 | 0.183 |
| C | 0.201 | 0.205 | 0.208 | 0.205 |
| D | 0.221 | 0.227 | 0.227 | 0.229 |
| E | 0.240 | 0.247 | 0.247 | 0.249 |

E-D trees in which the rim is large enough to cause side-lobe printing. To avoid checking all possible E-D tree overlaps, a combinatorial problem, we calculate the optimal overlap between two features, which sets the nominal exposure level and the bias for these features. Then, the biases for the remaining features, whose E-D trees overlap that optimum, are calculated. The final design has the biases and overlapping E-D trees shown in Fig. 4.2.

Based on these simulations, a mask was fabricated to study the accuracy of the predictions outlined above. Table 4.2 gives the measured dimensions of the features on the

ED Trees for Bright and Dark Field Lines and Spaces of Varying Duty Cycle for a Rim PSM with Annular Illumination (CD = 0.30 μ m for the Critical Feature)

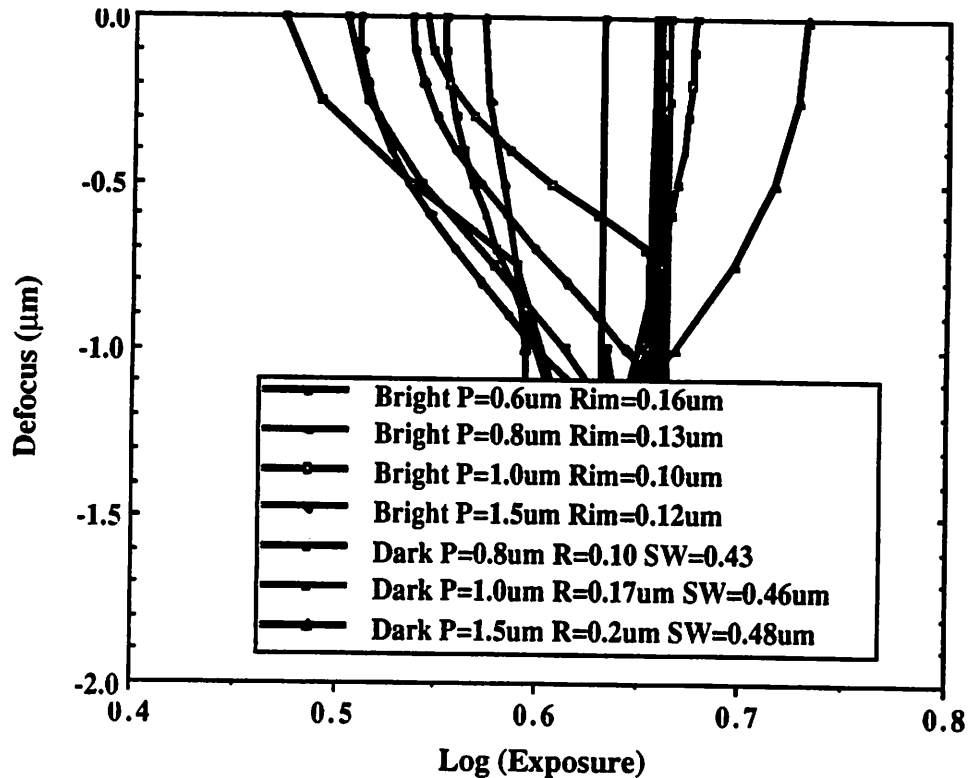


Figure 4.2 Overlapping E-D trees extracted with DRGEN for the bias design of a rim PSM with annular illumination. E-D trees assume 0.3 μ m \pm 7.5% CD control. $\lambda = 248$ nm, NA=0.48, $\sigma = 0.34$ -0.45.

mask. Conventional binary intensity mask patterns are also placed on the reticle. The rims on the reticle were laterally overetched due to an error in the fabrication. Also, note that the conventional mask patterns are etched 180 degrees into the quartz in this fabrication process. They are also over-etched so the space width on the mask for the four conventional bright field features is approximately 0.24 μ m.

4.3 Experimental Evaluation of Resist Lines Printed with Reticle

There are three important objectives in evaluating the performance of the reticle. The first objective is to experimentally verify our approach in choosing a phase-shift mask

TABLE 4.1. Coded Rim Sizes for Bright Field Rim PSM Features.

| Feature | Rim Width (μm) | | | |
|---------|--------------------------------|--------------------------------|--------------------------------|--------------------------------|
| | Pitch = $0.6\mu\text{m}$ | Pitch = $0.8\mu\text{m}$ | Pitch = $1.0\mu\text{m}$ | Pitch = $1.5\mu\text{m}$ |
| A | 0.12 | 0.12 | 0.12 | 0.12 |
| B | 0.14 | 0.14 | 0.14 | 0.14 |
| C | 0.16 | 0.16 | 0.16 | 0.16 |
| D | 0.18 | 0.18 | 0.18 | 0.18 |
| E | 0.20 | 0.20 | 0.20 | 0.20 |

TABLE 4.2. Measured Rim Sizes for Bright Field Rim PSM Features.

| Feature | Rim Width (μm) | | | |
|---------|--------------------------------|--------------------------------|--------------------------------|--------------------------------|
| | Pitch = $0.6\mu\text{m}$ | Pitch = $0.8\mu\text{m}$ | Pitch = $1.0\mu\text{m}$ | Pitch = $1.5\mu\text{m}$ |
| A | 0.162 | 0.163 | 0.164 | 0.164 |
| B | 0.180 | 0.189 | 0.185 | 0.183 |
| C | 0.201 | 0.205 | 0.208 | 0.205 |
| D | 0.221 | 0.227 | 0.227 | 0.229 |
| E | 0.240 | 0.247 | 0.247 | 0.249 |

E-D trees in which the rim is large enough to cause side-lobe printing. To avoid checking all possible E-D tree overlaps, a combinatorial problem, we calculate the optimal overlap between two features, which sets the nominal exposure level and the bias for these features. Then, the biases for the remaining features, whose E-D trees overlap that optimum, are calculated. The final design has the biases and overlapping E-D trees shown in Fig. 4.2.

Based on these simulations, a mask was fabricated to study the accuracy of the predictions outlined above. Table 4.2 gives the measured dimensions of the features on the

**ED Trees for Bright and Dark Field Lines and Spaces of Varying Duty Cycle for a Rim PSM with Annular Illumination
(CD = 0.30 μ m for the Critical Feature)**

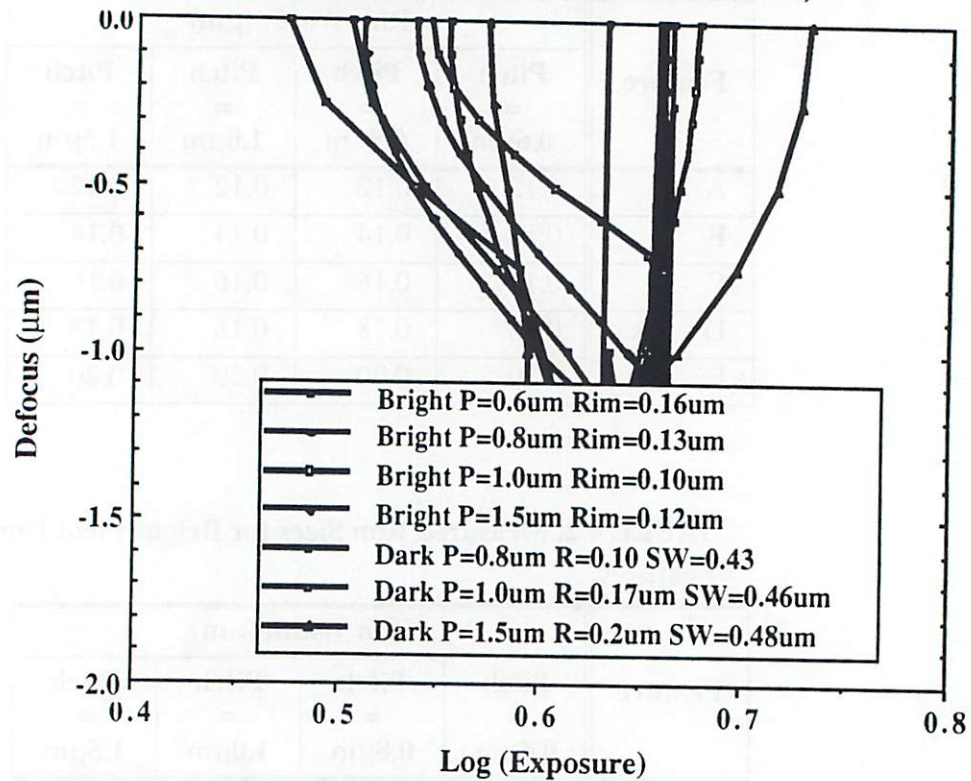


Figure 4.2 Overlapping E-D trees extracted with DRGEN for the bias design of a rim PSM with annular illumination. E-D trees assume 0.3 μ m \pm 7.5% CD control. $\lambda = 248$ nm, NA=0.48, $\sigma = 0.34$ -0.45.

mask. Conventional binary intensity mask patterns are also placed on the reticle. The rims on the reticle were laterally overetched due to an error in the fabrication. Also, note that the conventional mask patterns are etched 180 degrees into the quartz in this fabrication process. They are also over-etched so the space width on the mask for the four conventional bright field features is approximately 0.24 μ m.

4.3 Experimental Evaluation of Resist Lines Printed with Reticle

There are three important objectives in evaluating the performance of the reticle. The first objective is to experimentally verify our approach in choosing a phase-shift mask

technique, which hinges on the prediction of dead zones in performance because the dead zone determines the minimum depth of focus. The second objective is to experimentally compare the performance of the rim phase-shift mask with annular illumination to other methods. Our final objective is to ascertain whether overlapping E-D trees predict the correct bias for printing phase-shift features with the proper CD. Certain mask fabrication errors made it impossible to check the bias predictions for printing all bright field features and all dark field features with the same CD; however, a subset of the features print with a CD of $0.32\mu\text{m} \pm 10\%$, and these features are compared to the simulation predictions.

The exposure tool used for these experiments is a GCA DUV ($\lambda=0.248$) stepper with 0.48 NA. Two sets of exposures are made with the reticle using Shipley XP8931 negative resist. For both sets, the best dose is determined by finding the dose required to print the CD as close as possible to our target of $0.3\mu\text{m}$ for the phase-shift features. Exposures are then done for a focus matrix at this and nearby doses. The experiment is repeated for two illumination configurations. The partial coherence for the stepper is 0.45 for conventional illumination while annular illumination employed a ring from 0.34 to 0.45, which is part of the annular illumination system provided by GCA. In reviewing the experimental results, note that the optimum benefit from the rim PSM with annular illumination occurs for larger σ .

One of the fundamental features of our analyses of various phase-shift mask types has been to alleviate the dead zones; thus, it is necessary to demonstrate the effect and show its importance. To accomplish this task, CD versus defocus plots from aerial images are compared to CD versus defocus plots from resist CD measurements for a specific dose. With this established, the depth of focus for some phase-shift and annular illumination schemes are compared to experimental results, and SEM cross-sections are used to confirm the dead zone effect. Finally, some insight into the meaning of dead zones for lithography engineers is given.

4.3.1 Comparison of Aerial Image Simulations and Experiment

Fig. 4.3 illustrates the accuracy of the SPLAT simulations for predicting the resist CD at a single dose. The four features studied in this example are in Table 3 row A. The features measured on the wafer are minimum sized spaces in negative photoresist at periods of $0.6\mu\text{m}$, $0.8\mu\text{m}$, $1.0\mu\text{m}$ and $1.5\mu\text{m}$. The dose used for the comparison is 18mJ . The experimental CD is extracted using a Hitachi 6000 top-view SEM. To extract the simulated CD, the intensity must be normalized to the experimental dose. The normalization is accomplished by matching the CD measured on the wafer with the CD from an intensity level in the aerial image for the feature with period equal to $1.5\mu\text{m}$. Once the intensity level at which that feature prints is determined, the other critical dimensions are predicted using that level. As shown in Fig. 4.3, the critical dimensions measured from the wafer track the predictions of the aerial images. Notice that the increase in CD from $0.23\mu\text{m}$ to $0.30\mu\text{m}$ as the period changes is predicted by the aerial image.

4.3.2 Depth of Focus Predictions Compared to Experiment

The bar graphs in Fig. 4.4 summarize the comparison between the depth of focus predicted by E-D trees and SMILE (CD vs. focus) plots generated from SPLAT and experimental data. Fig. 4.4a shows the depth of focus for a binary intensity mask with annular illumination. Although the E-D trees over-predict the depth of focus compared to the experiment, the simulations track the experimental results, and they indicate the zone of reduced depth of focus. Fig. 4.4b is a plot of the depth of focus for a rim PSM with annular illumination; it further supports the argument that the depth of focus predicted by E-D trees tracks the depth of focus extracted experimentally.

4.3.3 Dead Zones Confirmed by SEM cross-sections

SEM cross-sections further illustrate the dead zone effect and indicate its importance. Fig. 4.5 shows the SEM cross-sections of a binary intensity mask with conventional illu-

Comparison of CD vs. Defocus Plots Generated from SPLAT with Experimental Measurements of Rim PSM with Annular Illumination.

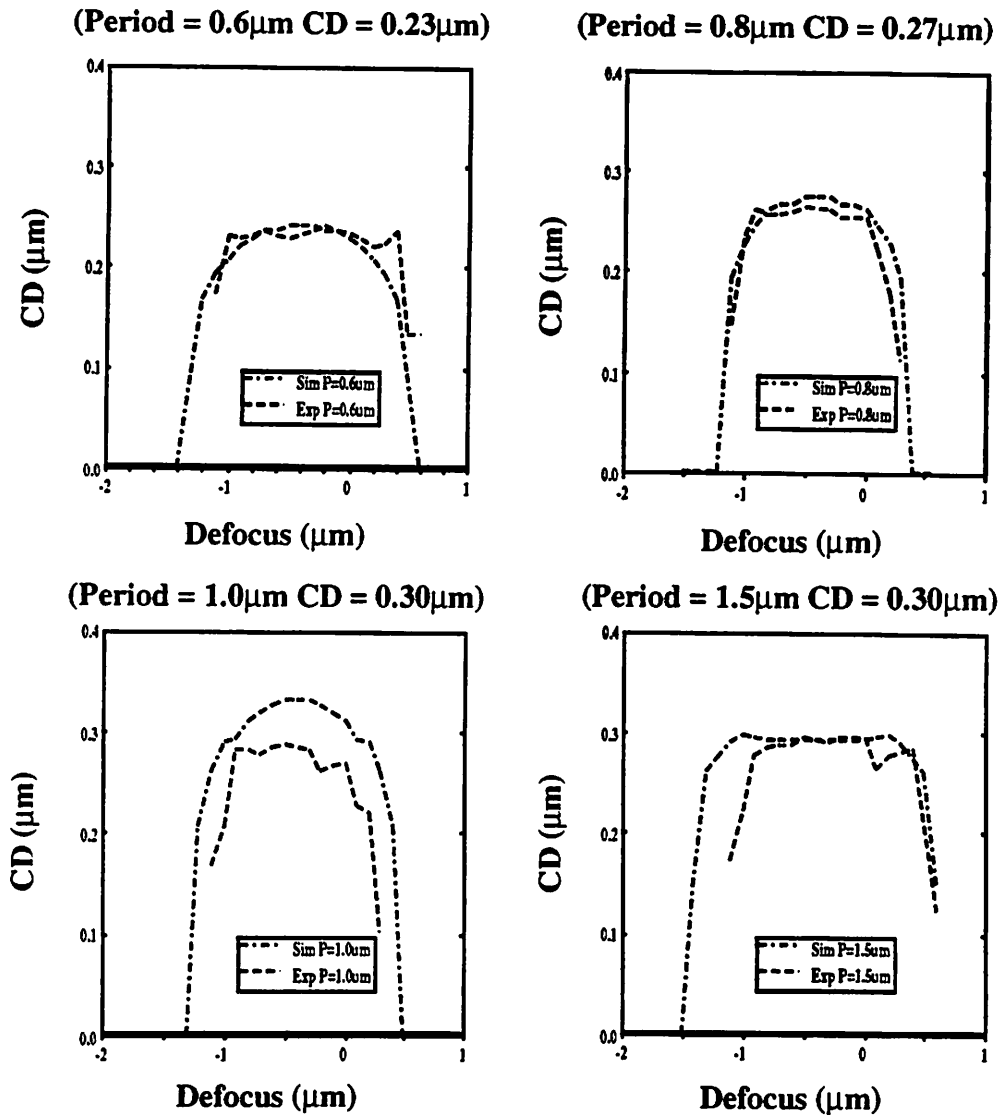
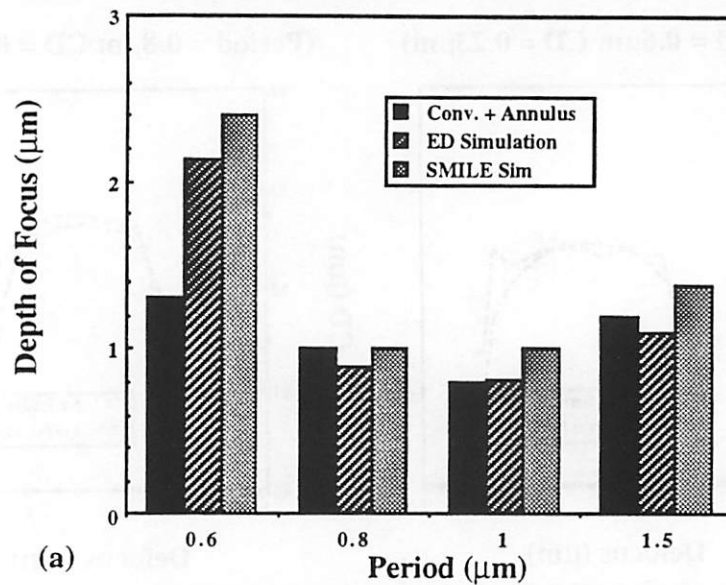


Figure 4.3 CD vs. defocus plots for rim phase-shifting mask with annular illumination. The plots are normalized using the space with a period of $1.5\mu\text{m}$ to find the intensity threshold in the aerial image for printing in the photoresist. (a), (b), and (d) show excellent agreement with simulation and track the observed increase in CD. (c) Deviates from the simulation by 10%. A constant rim width of $0.16\mu\text{m}$ is used for all features. $\lambda = 248\text{nm}$, 0.48 NA , and annular illumination from 0.34 to 0.45 .

Experimental and Simulated Depth of Focus for Bright Field Spaces of Varying Duty Cycle with BIM and Annular Illumination



Experimental and Simulated Depth of Focus for Bright Field Spaces of Varying Duty Cycle with Rim = 0.16 μm and Annular Illumination

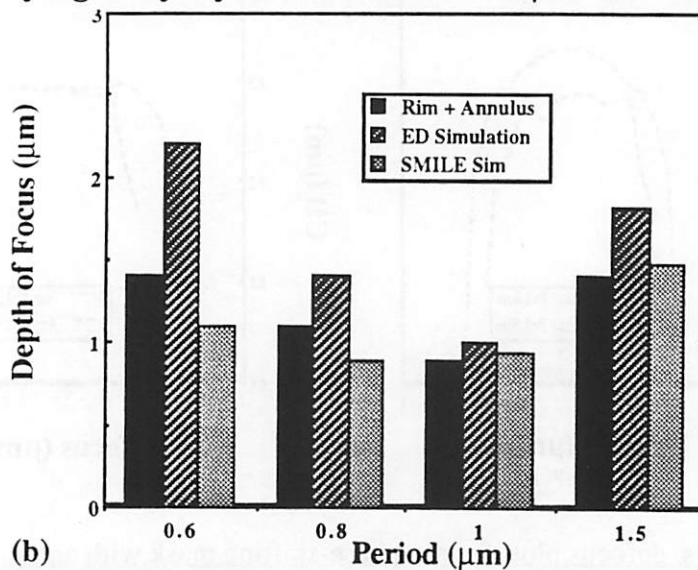


Figure 4.4 Experimental and simulate depth of focus measurements for bright field spaces of varying duty cycle with (a) BIM and annular illumination and (b) rim = 0.16 μm and annular illumination. The E-D trees are generated based on CD = 0.3 μm ± 7.5% and the depth of is extracted based on 20% exposure latitude. The simulated SMILE plots are normalized to the period = 1.5 μm features to find the intensity threshold for printing in the resist. (a) CD = 0.30 μm (b) CD is 0.23 μm for 0.6 μm period, 0.27 μm for 0.8 μm period and 0.30 μm for 1.0 μm and 1.5 μm periods.

mination for bright field spaces with a critical dimension of $0.3\mu\text{m}$ and periods of $0.6\mu\text{m}$, $0.8\mu\text{m}$, $1.0\mu\text{m}$ and $1.5\mu\text{m}$ at a defocus of $-0.2\mu\text{m}$ and $-0.6\mu\text{m}$. The indication from the pictures is that the dense features are the hardest to print and have the lowest depth of focus; this behavior is expected and explains why traditional lithography characterization techniques concentrate on only dense and isolated lines and spaces. Fig. 4.5 also shows the SEM photos for a rim phase-shift mask with conventional illumination at $+0.3\mu\text{m}$ defocus to illustrate its poor performance for dense features. Fig. 4.6 shows the SEM cross-sections for a binary intensity mask with annular illumination at defocus levels of $0.4\mu\text{m}$, $0.6\mu\text{m}$ and $0.7\mu\text{m}$ for a dose of 18mJ . The figure illustrates the depth of focus reduction in the dead zone. Features with a period of $0.6\mu\text{m}$ and $1.5\mu\text{m}$ have a larger depth of focus than the features with periods of $0.8\mu\text{m}$ and $1.0\mu\text{m}$. Our results indicate that this effect is symmetric around best focus, so the depth of focus is decreased by $0.4\mu\text{m}$ from a total of $1.4\mu\text{m}$, a 30% reduction. Therefore, for annular illumination with a binary intensity mask, the dead zone reduces the depth of focus significantly, and it is no longer sufficient to characterize only dense and isolated lines and spaces. The dead-zone is the limiting factor for depth of focus calculations. Fig. 4.7 illustrates the cross sections for a rim phase-shift mask with annular illumination and indicates a slightly reduced dead zone. The depth of focus is $1.2\mu\text{m}$ for dense features and $1.0\mu\text{m}$ for isolated ones so the reduction is 15%. The rim tends to level out the dead zone, and simulations suggest that a more significant reduction in the dead zone and an increase in the depth of focus occurs with a larger annulus, but our stepper was limited to an outer partial coherence of 0.45. Simulations suggest that the dead zone becomes worse for lower k_1 , so we expect a larger decrease in the depth of focus in the dead zone for conventional masks with annular illumination and a greater improvement with a rim phase-shift mask.

SEM Cross-Sections for Rim Phase-Shift Mask and Binary Intensity Mask Conventional Illumination

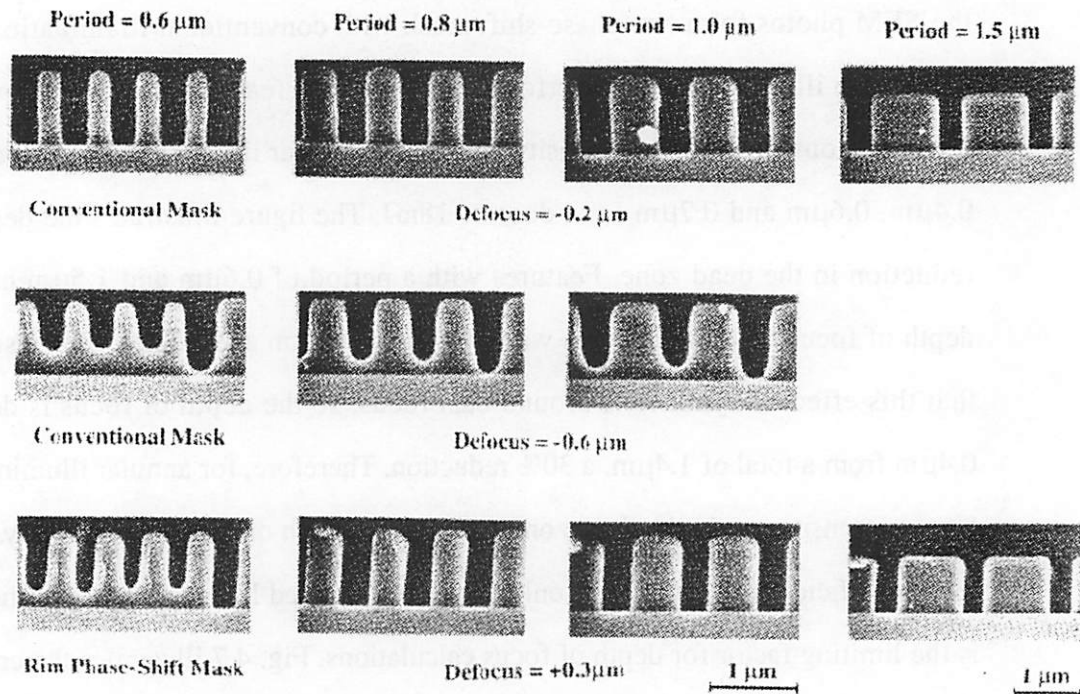


Figure 4.5 SEM cross-sections for a conventional mask and a rim phase-shifting mask for 0.3μm spaces in Shipley XP89131 negative resist. A GCA stepper with $\lambda = 248\text{nm}$ and 0.48 NA is used to expose the wafers. The 0.3μm spaces are shown for periods of 0.6μm, 0.8μm, 1.0μm, and 1.5μm. The two defocus levels of -0.2μm and -0.6μm for the conventional mask illustrate that the dense features are the most difficult ones to print. The photos for the rim phase-shifting mask at a defocus of +0.3μm show its poor performance for dense features.

SEM Cross-Sections for Binary Intensity Mask with Annular Illumination

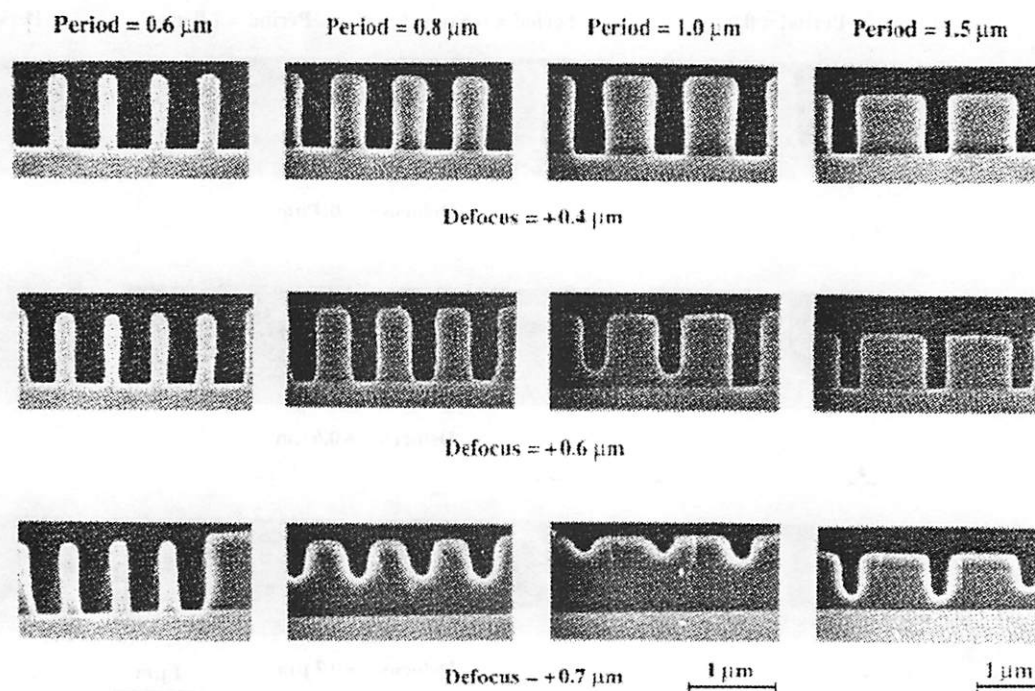


Figure 4.6 SEM cross-sections for a binary intensity mask with annular illumination for 0.3 μm spaces in Shipley XP89131 negative resist. A GCA stepper with $\lambda = 248\text{nm}$ and 0.48 NA is used to expose the wafers. The 0.3 μm spaces are shown for periods of 0.6 μm, 0.8 μm, 1.0 μm, and 1.5 μm. The three defocus levels of 0.4 μm, 0.6 μm, and 0.7 μm illustrate the dead zone since the depth of focus for the 0.8 μm and 1.0 μm features is less than the depth of focus for the 0.6 μm and 1.5 μm features.

SEM Cross-Sections for Rim Phase-Shift Mask with Annular Illumination

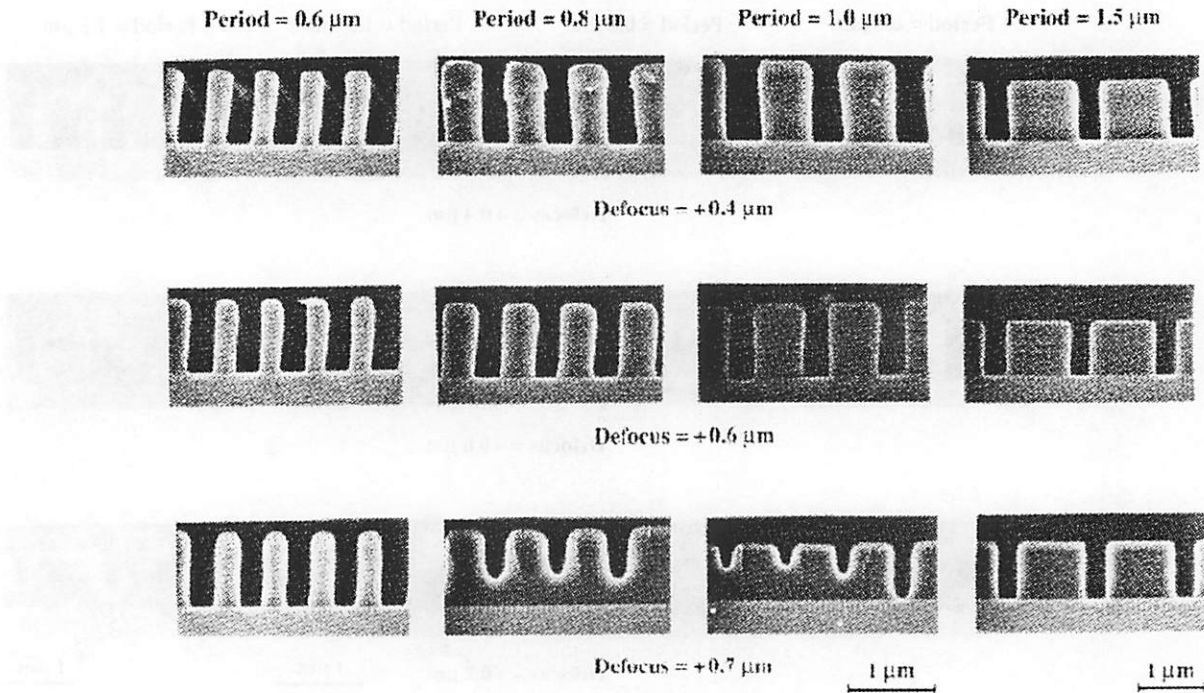


Figure 4.7 SEM cross-sections for a rim phase-shifting mask with annular illumination for 0.3 μm spaces in Shipley XP89131 negative resist. A GCA stepper with $\lambda = 248\text{nm}$ and 0.48 NA is used to expose the wafers. The 0.3 μm spaces are shown for periods of 0.6 μm, 0.8 μm, 1.0 μm, and 1.5 μm. The three defocus levels of 0.4 μm, 0.6 μm, and 0.7 μm illustrate the dead zone as in the previous figure. However, the depth of focus reduction in the dead zone is less.

4.3.4 Comparison of Rim PSM with Annular Illumination to other PSM Techniques

A more complete comparison of the depth of focus of a rim phase-shift mask with annular illumination to other methods is shown in the bar graph of Fig. 4.8. The depth of focus of a rim phase-shift mask with annular illumination is compared to the depth of focus of a rim phase-shift mask with conventional illumination, a conventional binary intensity mask, and a conventional binary intensity mask with annular illumination. As shown by others evaluating annular illumination, the depth of focus for dense features is vastly improved over the depth of focus for a binary intensity mask with conventional illumination. However, the depth of focus is reduced in the dead zone. The rim phase-shift mask alone has a reasonable depth of focus for more isolated bright field features, but the rim degrades the depth of focus for dense features. The depth of focus for a rim phase-shift mask with annular illumination is close to the depth of focus of a binary intensity mask with annular illumination for dense as well as more isolated lines. However, the rim improves the depth of focus in the dead zone and reduces the dead zone degradation. Thus, the rim phase-shift mask with annular illumination is a promising technique for printing dense and isolated lines without suffering the degradation in depth of focus that occurs with a rim mask used for dense lines or a binary intensity mask with annular illumination in the dead zone. We expect to see more improvements of the rim PSM with annular illumination over a BIM with annular illumination for lower k_1 .

4.3.5 Overlapping E-D Trees Predict the Correct Bias

An unintended bias introduced during fabrication of the phase-shift reticle made it impossible to print $0.3\mu\text{m}$ features for all bright and dark field patterns. However, it is possible to print $0.32\mu\text{m}$ lines for $0.8\mu\text{m}$ and $1.5\mu\text{m}$ periods and a $0.32\mu\text{m}$ space at a $1.5\mu\text{m}$ period with the rim phase-shift mask and annular illumination. These features are used to confirm our phase-shift mask design criteria that overlapping E-D trees correctly predict the bias needed to print features at the same CD. The E-D trees for the three fea-

Depth of Focus for Bright and Dark Field Features at Their Nominal CD and Varying Duty Cycle

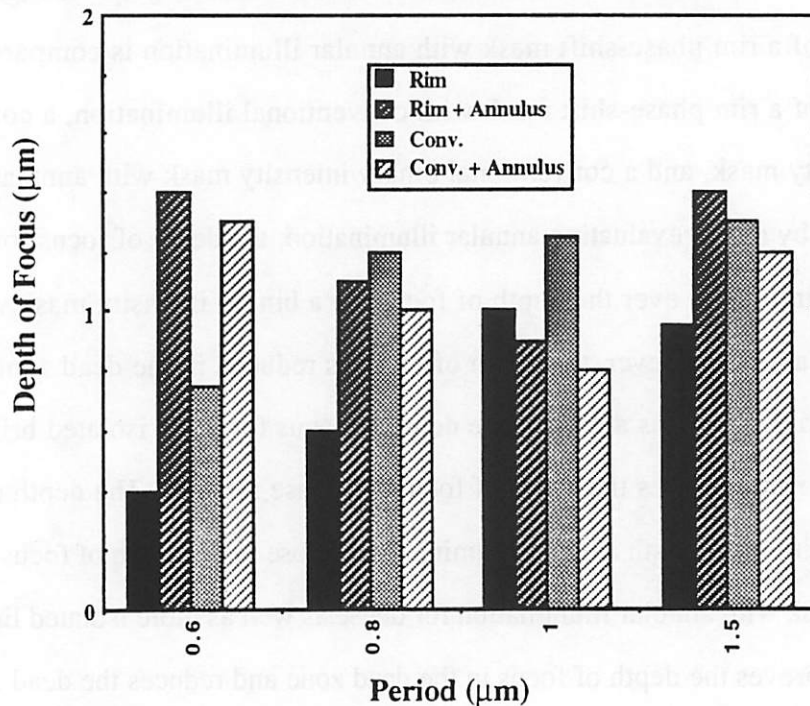
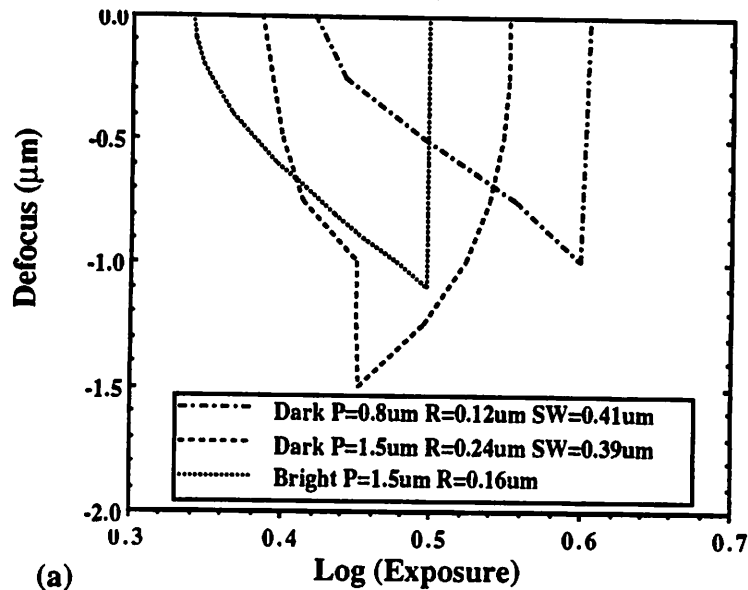


Figure 4.8 Comparison of depth of focus measurements for rim PSM, rim PSM with annular illumination, binary intensity mask, and binary intensity mask with annular illumination. When the target CD is not achieved, the measured CD is used to get a depth of focus measurement. The features have a target CD of $0.3\mu\text{m}$. The bright field features are spaced at periods of $0.6\mu\text{m}$, $0.8\mu\text{m}$, $1.0\mu\text{m}$, and $1.5\mu\text{m}$. $\lambda = 248\text{nm}$, $\text{NA} = 0.48$, $\sigma = 0.34-0.45$ for annular illumination, and $\sigma = 0.45$ for conventional illumination.

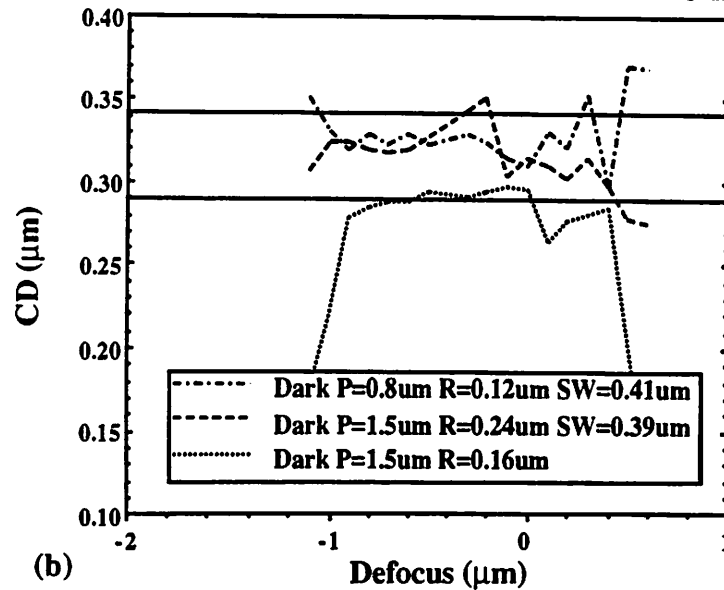
tures are shown in Fig. 4.9a, and the SMILE plot for the dose of 18mJ is shown in Fig. 4.9b. The critical dimension for the three features are within $\pm 10\%$ as shown in the SMILE plot, and the E-D trees overlap at a specific dose. Further confirmation of the depth of focus predicted by overlapping E-D trees requires a significant investment in SEM time to evaluate a sufficient number of features at enough exposure and defocus levels.

Simulated ED Trees of Bright and Dark Field Features for $CD = 0.32\mu\text{m} \pm 7.5\%$



(a)

Experimental CD vs. Defocus for Rim PSM with Annular Illumination - Dose = 18mJ



(b)

Figure 4.9 (a) Simulated E-D trees for three features: Line = $0.32\mu\text{m}$ at a period of $0.8\mu\text{m}$ and $1.5\mu\text{m}$ and space = $0.3\mu\text{m}$ at a period of $1.5\mu\text{m}$. (b) These features print within the $\pm 10\%$ CD tolerance bands indicating that the E-D trees for the features should overlap for some dose, which agrees with the simulation prediction. $\lambda = 248\text{nm}$, $NA = 0.48$, and $\sigma = 0.34-0.45$

4.4 Summary

A design system, DRGEN, that utilizes E-D trees to find a phase-shift mask technique and bias the mask to print features at the desired critical dimension, has been developed and tested for one-dimensional patterns. The system is first used to analyze a variety of phase-shift mask methods and illumination schemes, such as binary intensity masks, alternate aperture masks, attenuating masks, and rim phase-shift masks with conventional and annular illumination. Due to its better overall performance for constant width lines of varying duty cycle, the rim phase-shift mask with annular illumination is chosen as a candidate technique for biasing. A mask is designed using DRGEN to print $0.3\mu\text{m}$ lines and spaces of varying duty cycle. Experimental evaluation of the focus matrices printed using the reticle confirm that our design criteria of improving the depth of focus in the dead zone is important. In fact, the results indicate that values of the depth of focus for only dense and isolated lines and spaces using modified illumination techniques are misleading, since they do not show the decrease in the depth of focus for certain line-space ratios. Furthermore, our results show that the rim phase-shift mask offers a more uniform depth of focus compared to other phase-shift mask and illumination techniques. Finally, the bias obtained from overlapping E-D trees predicts the correct bias for designing phase-shift features.

Chapter 5 Experimental Verification: Effects at Low k_1

5.1 Introduction

As features become smaller, the advantages of annular illumination and rim phase-shifting masks becomes more impressive, but the gains are not achieved without some trade-offs. The benefits are twofold. First, there is a significant depth of focus improvement of rim phase-shifting masks over binary intensity masks for dense lines and spaces. Second, rim phase-shifting masks provide the capability of printing isolated lines. The basic trade-off is that proximity effects cause a dense isolated line split, a difference between the linewidth of dense versus isolated lines, which can be as large as 30% of the total linewidth. The 30% linewidth change is a grave concern and the underlying reasons for the problem are addressed in this chapter. The chapter also explores the advantages and disadvantages of rim phase-shifting masks and annular illumination at low k_1 using experimental results from a scaled version of the rim phase-shifting mask described in Chapter 4. The mask is shrunk by 0.72 to enable printing of $0.22\mu\text{m}$ features at pitches of $0.44\mu\text{m}$, $0.56\mu\text{m}$, $0.72\mu\text{m}$, and $1.08\mu\text{m}$. These features correspond to a k_1 of 0.47, which is much more aggressive than the value of 0.6 used for the experiments in Chapter 4.

5.2 Dense Features

To understand the large depth of focus improvements for dense lines and spaces, it is necessary to revisit the explanation of diffraction limited projection printing discussed in Chapter 2. As described there, 2-beam versus 3-beam imaging explains the depth of focus enhancement for annular illumination with binary intensity masks and rim phase-shifting masks [1,2]. In conventional illumination, the 0, +1, and -1 orders fall within the aperture of the projection lens and the aerial image is created by the interference of these orders (see also Fig. 2.3). In off-axis illumination, the 0 order passes through the mask and falls

on one edge of the aperture while the +1 order is diffracted to the other edge of the aperture; these two orders interfere to produce the image (see also Fig. 2.7). Decomposing a line and space pattern into a Fourier series gives the magnitude of the 0 and +1 orders. For a binary intensity mask, these values are 0.5 and 0.32 respectively. Since the orders are unequal, the background noise level is high and the contrast is less than 100%. By boosting the +1 order, the aerial image contrast improves and the depth of focus increases. For the rim used in our experimental results, the central order is 0.44 while the first order is 0.49. These values are obtained for a $0.14\mu\text{m}$ rim used to print a $0.25\mu\text{m}$ feature on a $0.5\mu\text{m}$ pitch.

A rim phase-shifting mask and annular illumination also improves the depth of focus for isolated lines. This result is accomplished in two ways. First, the energy distribution over the pupil is altered to reduce the zero order and increase the amount of modulated energy. A comparison of the magnitude of the Fourier components for a binary intensity mask and rim PSM is shown in Fig. 5.1 for a $0.22\mu\text{m}$ line with a pitch of $1.08\mu\text{m}$. Notice that the zero order is slightly reduced and the amount of modulated energy is increased for the rim PSM. Second, a rim PSM requires a much lower dose for dense lines and spaces, so a lower effective dose is used for the isolated lines. At low doses, isolated features are much easier to print. Thus, rim phase-shifting masks used with annular illumination overcome the loss in process window by utilizing a lower dose and a less intense zero order to print isolated lines.

5.3 Mask Design

To test the theory that rim phase-shifting masks and annular illumination can be used synergistically, a rim PSM was fabricated and exposed on a DUV stepper. The mask is actually a scaled version of the one described in Chapter 4. The pertinent features on the mask are shown in Fig. 5.2. As discussed previously, in rim PSM design, the chrome

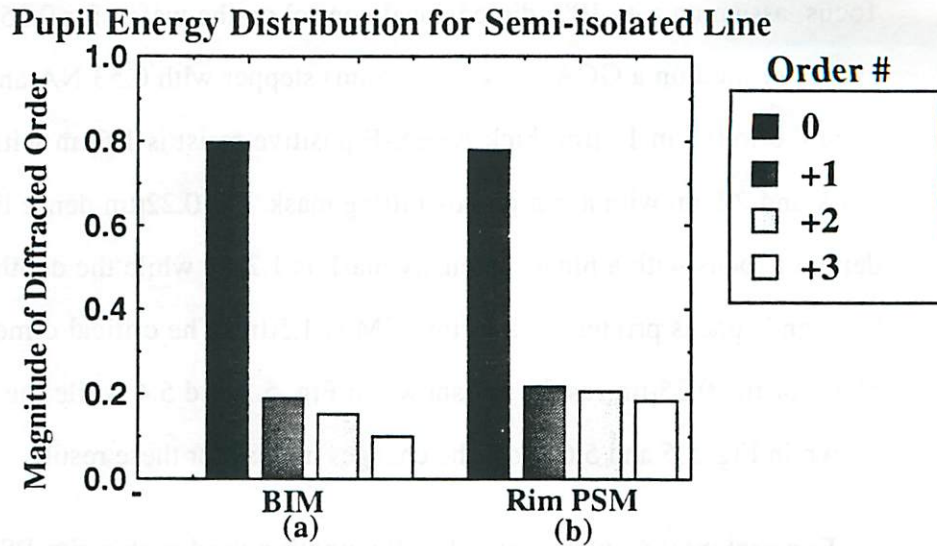


Figure 5.1 Magnitude of diffracted orders for $0.22\mu\text{m}$ lines on a $1.08\mu\text{m}$ pitch using (a) binary intensity mask and (b) rim phase-shifting mask.

width decreases as the line becomes narrower. For these features, the chrome width shrinks to zero, leaving only a chrome-less phase shift line. The rim width (assuming 1X dimensions on the mask) is $0.16\mu\text{m}$, and the rims are spaced at pitches of $0.44\mu\text{m}$, $0.58\mu\text{m}$, $0.72\mu\text{m}$, and $1.08\mu\text{m}$ to test proximity effects.

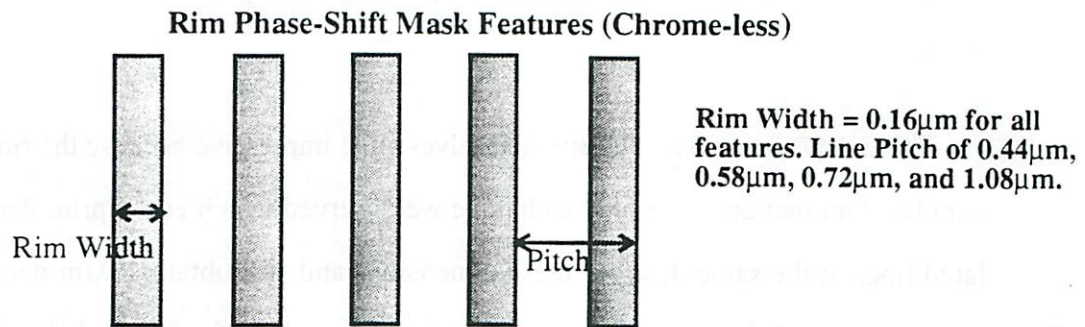


Figure 5.2 Line and space patterns of varying pitch used to test proximity effects for a rim phase-shift mask with annular illumination.

5.4 Experimental Results

Experimental results confirm the prediction that the depth of focus of dense and isolated lines increases for a rim phase-shifting mask and annular illumination. The depth of

focus, assuming a $\pm 10\%$ dimensional control on the wafer, for $0.25\mu\text{m}$ dense lines and spaces printed on a GCA DUV ($\lambda=248\text{nm}$) stepper with 0.53 NA and partial coherence from 0.6 to 0.7 in $1.0\mu\text{m}$ thick APEX-E positive resist is $1.6\mu\text{m}$ with a binary intensity mask and $2.5\mu\text{m}$ with a rim phase-shifting mask. For $0.22\mu\text{m}$ dense lines and spaces, the depth of focus with a binary intensity mask is $1.2\mu\text{m}$ while the depth of focus for dense lines and spaces printed with a rim PSM is $1.5\mu\text{m}$. The critical dimension versus focus plots for the $0.25\mu\text{m}$ results are shown in Fig. 5.3 and 5.4 while the $0.22\mu\text{m}$ results are shown in Fig. 5.5 and 5.6. Note the changes in dose for these results.

Experimental results of annular illumination used with a rim PSM to print isolated lines also show the expected depth of focus improvement. Fig. 5.7 illustrates that the depth of focus for an isolated line (pitch $1.08\mu\text{m}$) is approximately $1.2\mu\text{m}$ for two different rim sizes. Our hypothesis that the depth of focus improvement for isolated lines is influenced by a dose change is evident in the fact that the rim PSM requires a much lower dose to resolve dense lines and spaces. Thus, the isolated lines printed with the rim PSM utilize a much lower dose than the corresponding lines printed with a binary intensity mask.

These experimental results are themselves quite impressive because the rim PSM with annular illumination is the only technique we observed which could print dense and isolated lines at the same dose for these dimensions and still obtain $1.0\mu\text{m}$ depth of focus. For example, while conventional illumination is capable of printing dense and isolated lines, the depth of focus is only $0.4\mu\text{m}$. Annular illumination can be used to print dense lines and spaces with $1.0\mu\text{m}$ depth of focus, but isolated lines can not be resolved. Finally, a rim phase-shifting mask and conventional illumination can resolve $0.22\mu\text{m}$ isolated lines, but not dense lines and spaces.

Critical Dimension versus Defocus

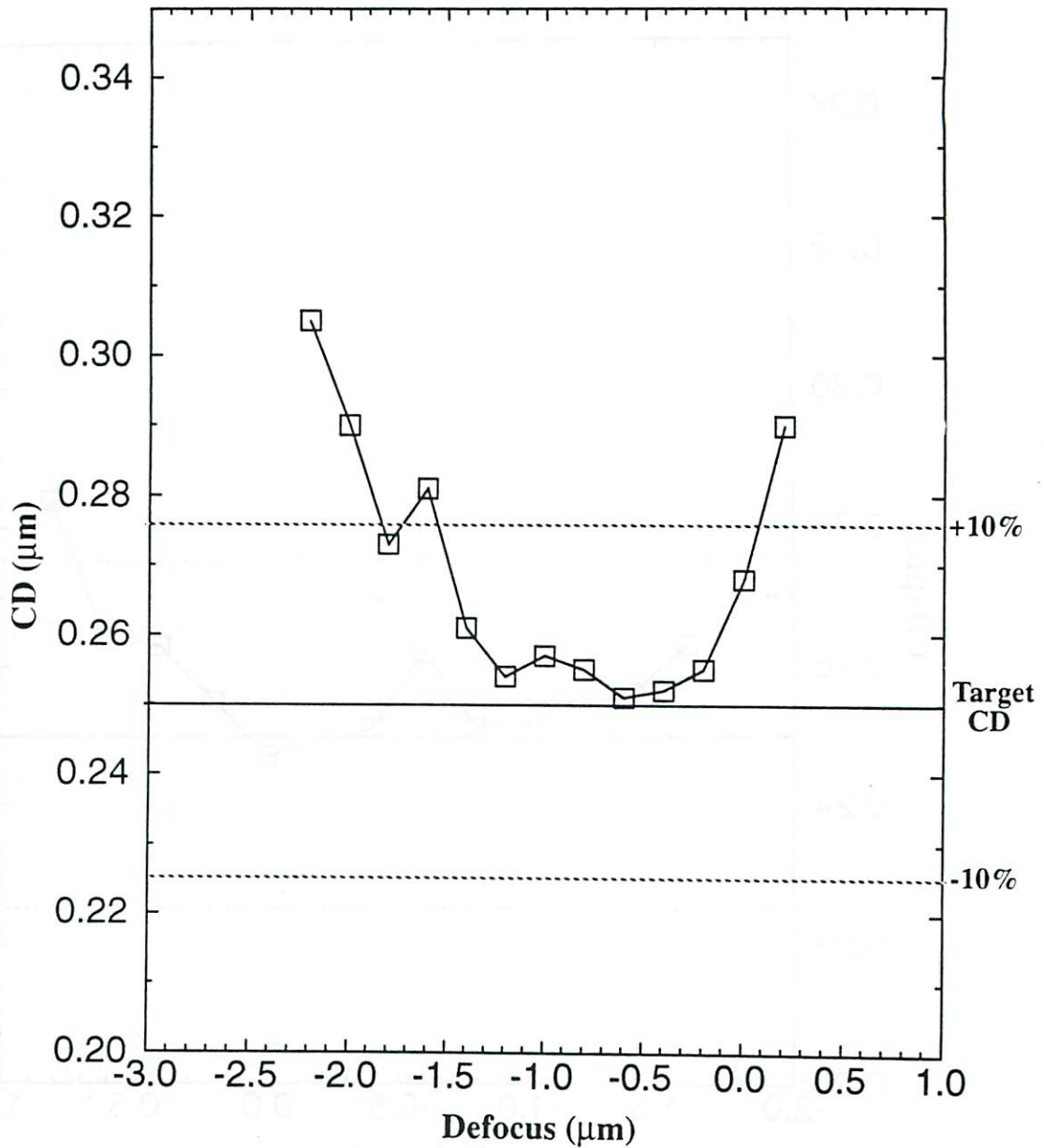
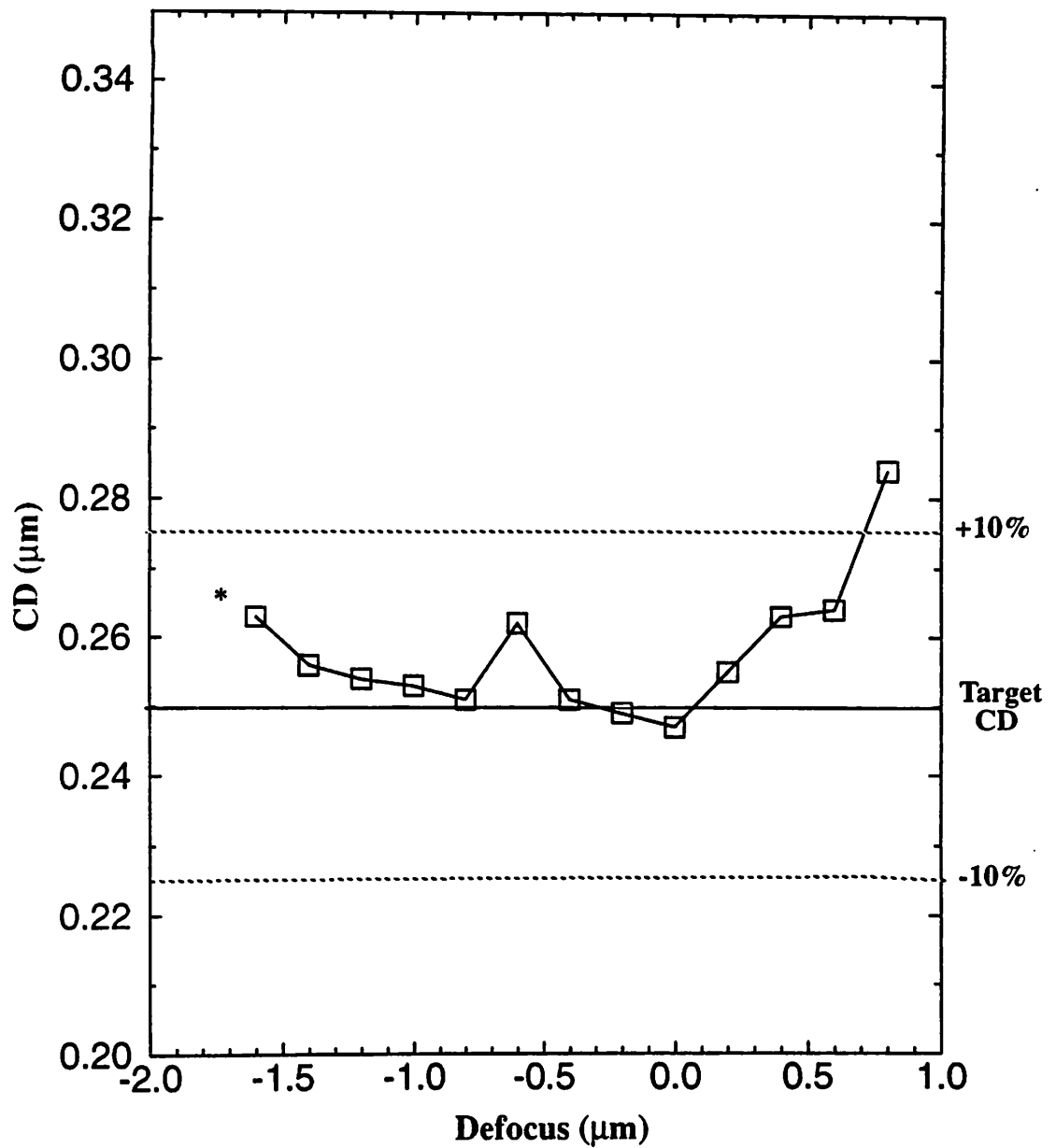


Figure 5.3 Critical dimension of dense lines and spaces versus defocus for a binary intensity mask with annular illumination in 1.0μm thick APEX-E. ($\sigma = 0.6-0.7$, $\lambda = 248\text{nm}$, $\text{NA} = 0.53$, Target CD = $0.25\mu\text{m}$, Dose = 21.2mJ .)

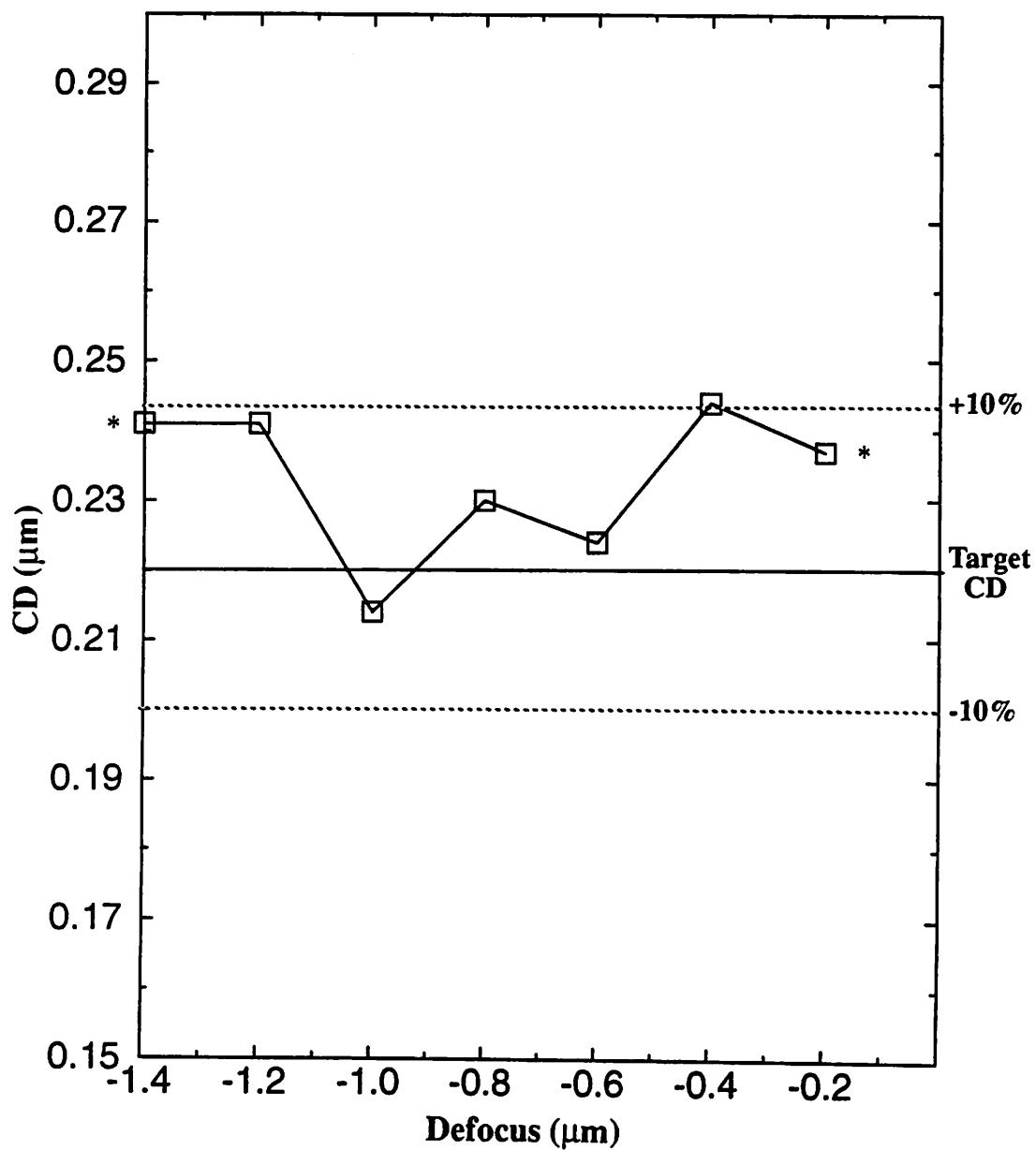
Critical Dimension versus Defocus



* The next focus setting was not resolved

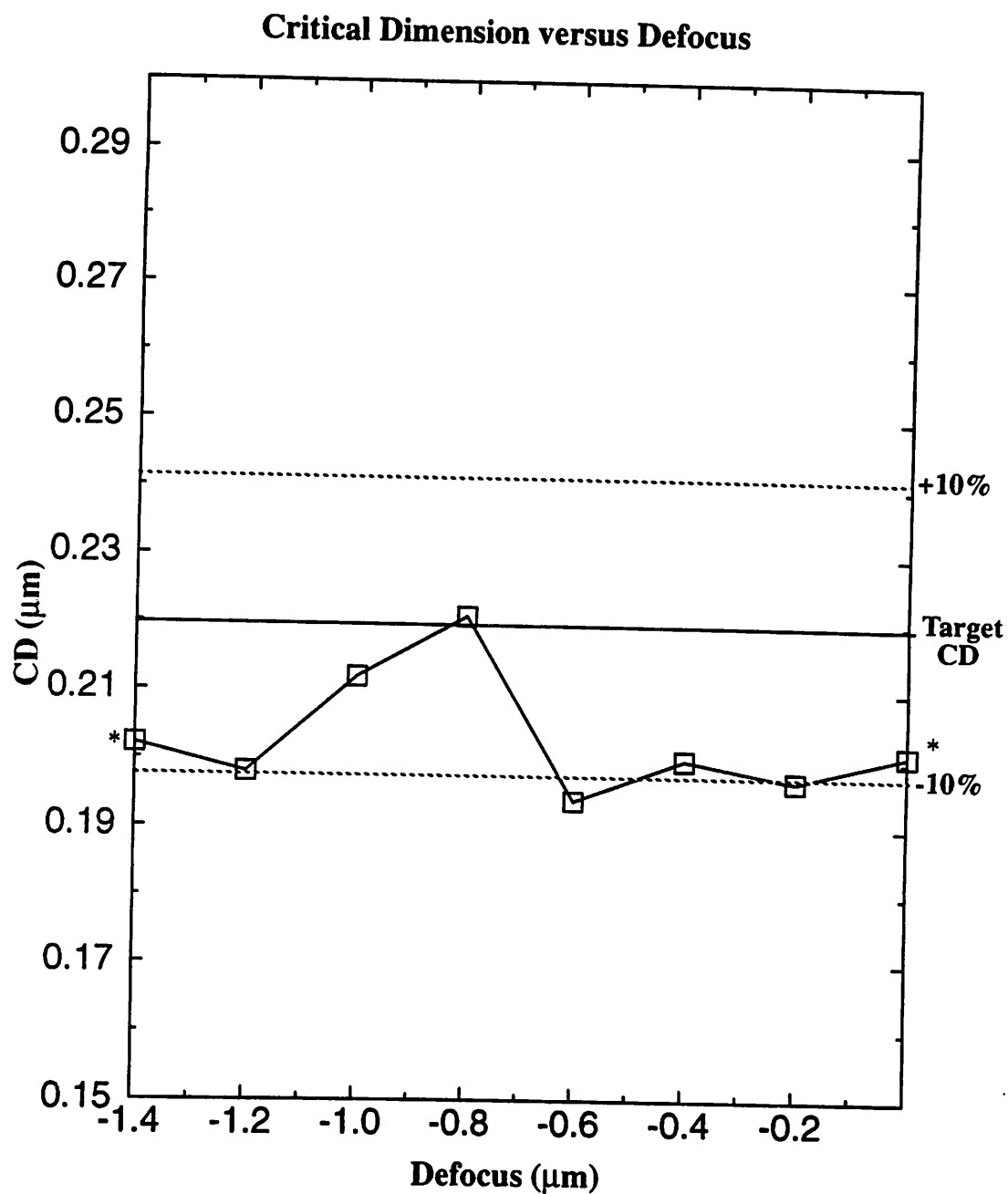
Figure 5.4 Critical dimension of dense lines and spaces versus defocus for a rim phase-shifting mask with annular illumination using 1.0 μm thick APEX-E. ($\sigma = 0.6-0.7$, $\lambda = 248\text{nm}$, $\text{NA} = 0.53$, Target CD = 0.25 μm , Dose = 16.4mJ.)

Critical Dimension versus Defocus



* The next focus setting was not resolved

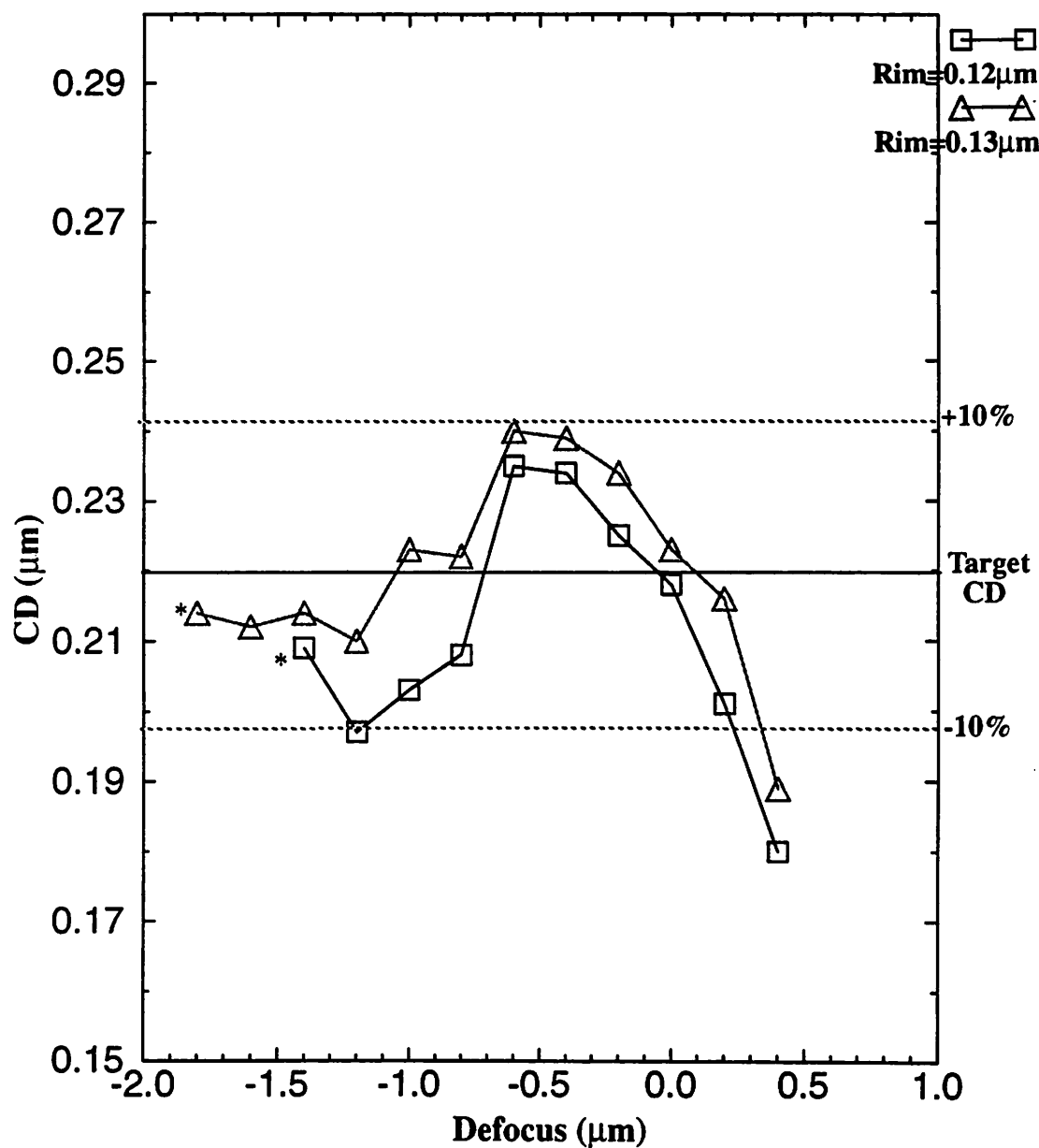
Figure 5.5 Critical dimension of dense lines and spaces versus defocus for a binary intensity mask with annular illumination using 1.0 μm thick APEX-E. ($\sigma = 0.6-0.7$, $\lambda = 248\text{nm}$, $\text{NA} = 0.53$, Target CD = 0.22 μm , Dose = 23.2mJ.)



* The next focus setting was not resolved

Figure 5.6 Critical dimension of dense lines and spaces versus defocus for a rim phase-shifting mask with annular illumination using 1.0 μm thick APEX-E. ($\sigma = 0.6$ - 0.7 , $\lambda = 248\text{nm}$, $\text{NA} = 0.53$, Target CD = $0.22\mu\text{m}$, Dose = 14.8mJ)

Critical Dimension versus Defocus



* The next focus setting was not resolved

Figure 5.7 Critical dimension of 0.22 μm line with pitch of 1.08 μm versus defocus for a rim phase-shifting mask with annular illumination and two rim sizes. ($\sigma = 0.6-0.7$, $\text{NA} = 0.53$, $\lambda = 248\text{nm}$, Dose = 14.8mJ).

5.5 Proximity Effects

It is well known that proximity effects are quite severe for annular illumination and detract from its usefulness for real integrated circuit layouts [3]. Feature dependent biasing is necessary since dense features printed at the correct dimension cause under or over-sizing of isolated features. Using a rim phase-shifting mask with annular illumination can exacerbate the problem. Fig. 5.8 shows the CD versus pitch at best focus and dose for a rim size of $0.10\mu\text{m}$. Experimentally, the feature size can be corrected by biasing the rim. However, as we shall see later, the required bias is not accurately predicted by the aerial image simulations alone.

5.6 Using Simulation to Understand the Severity of the Proximity Effect

Although it is important to know that proximity effects can be corrected by experimentally determining the bias, the fact that the aerial image simulation does not accurately predict the appropriate bias and that it must be chosen experimentally, motivates a closer look at proximity effects. The SEM photographs in Fig. 5.9 illustrate the proximity effect more clearly. The SEM cross-sections show $0.22\mu\text{m}$ features printed in $1.0\mu\text{m}$ of APEX-E using a GCA DUV stepper with 0.53 NA and $0.6-0.7 \sigma$. A constant rim size of $0.16\mu\text{m}$ is used for all pitches. The size of the lines varies from $0.21\mu\text{m}$ when the pitch is $0.44\mu\text{m}$ to $0.15\mu\text{m}$ when the pitch is $1.08\mu\text{m}$. This shrinkage corresponds to a 30% line-width error, even at best focus. The depth of focus for the dense lines and spaces is approximately $1.0\mu\text{m}$, or 1.13 RU. If the dimensions of the other features were on target, their depth of focus would also be $1.0\mu\text{m}$.

Although a large depth of focus for varying pitch lines is obtained with the rim phase-shifting mask and annular illumination technique, the dimensional control of the semi-isolated lines is a problem. By referring to the CD vs. focus plot in Fig. 5.10, which was obtained by measuring the CD at the base of the resist in Fig. 5.9, one can see that the lin-

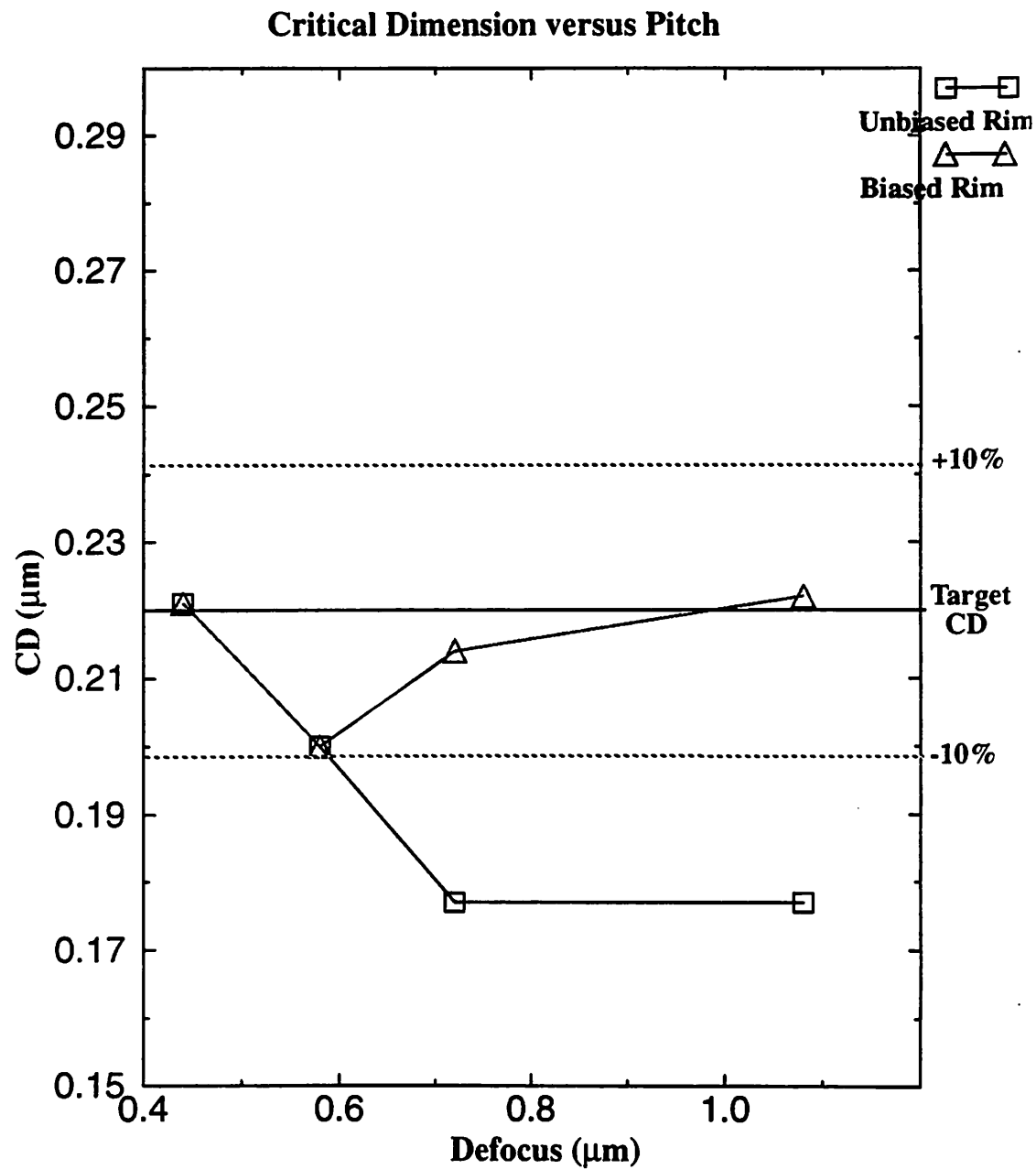


Figure 5.8 Critical dimension versus pitch to illustrate the proximity effect for 0.22 μm lines of varying pitch. The correct CD is obtained by experimentally choosing an appropriately sized rim from those available on the reticle. ($\sigma = 0.6-0.7$, $\text{NA} = 0.53$, $\lambda = 248\text{nm}$, Dose = 14.8mJ).

Rim Phase-Shifting Mask with Annular Illumination, Lines of Varying Pitch
 0.22 μm Features (Bright Field)
 DUV; 0.53 NA; 0.6-0.7 σ

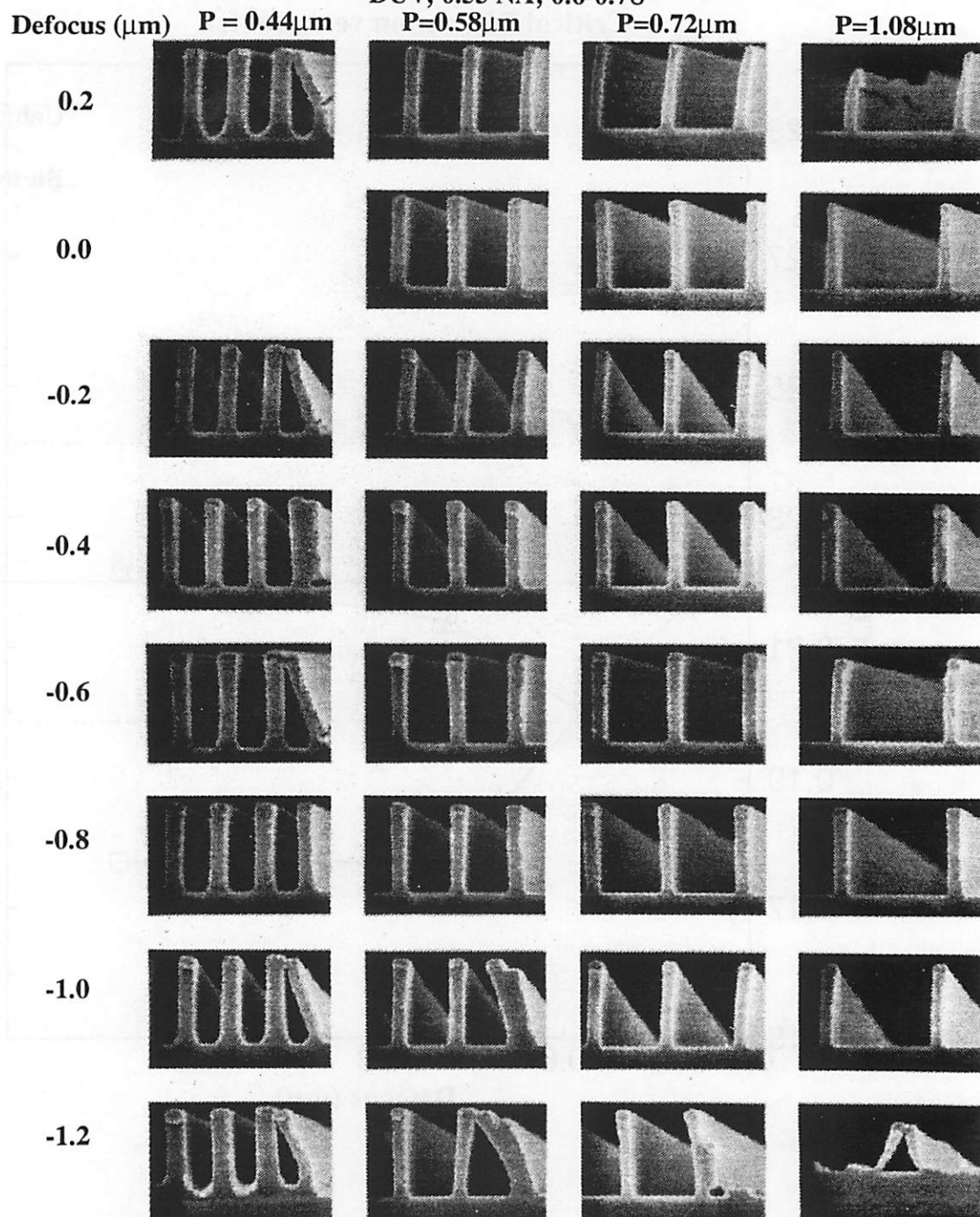


Figure 5.9 SEM cross-sections of 0.22 μm bright field lines of varying pitch illustrates the severity of the proximity effect. At best focus, the linewidth varies from 0.21 μm for dense lines and spaces to 0.15 μm for the more isolated lines as measured at the base of the resist profile. The lines were printed in 1.0 μm of APEX-E (IBM) using a GCA DUV stepper ($\lambda=248\text{nm}$, 0.53 NA, $\sigma=0.6-0.7$, Dose = 16.8mJ).

ewidth change between dense and isolated features is ~30% or 60nm. This proximity effect is extremely serious and needs to be understood theoretically if it is to be corrected by biasing the mask.

**CD vs. Focus ($\lambda = 248\text{nm}$, $\sigma = 0.6-0.7$, 0.53NA , $1.0\mu\text{m}$ thick APEX-E)
Nominal linewidth = $0.22\mu\text{m}$**

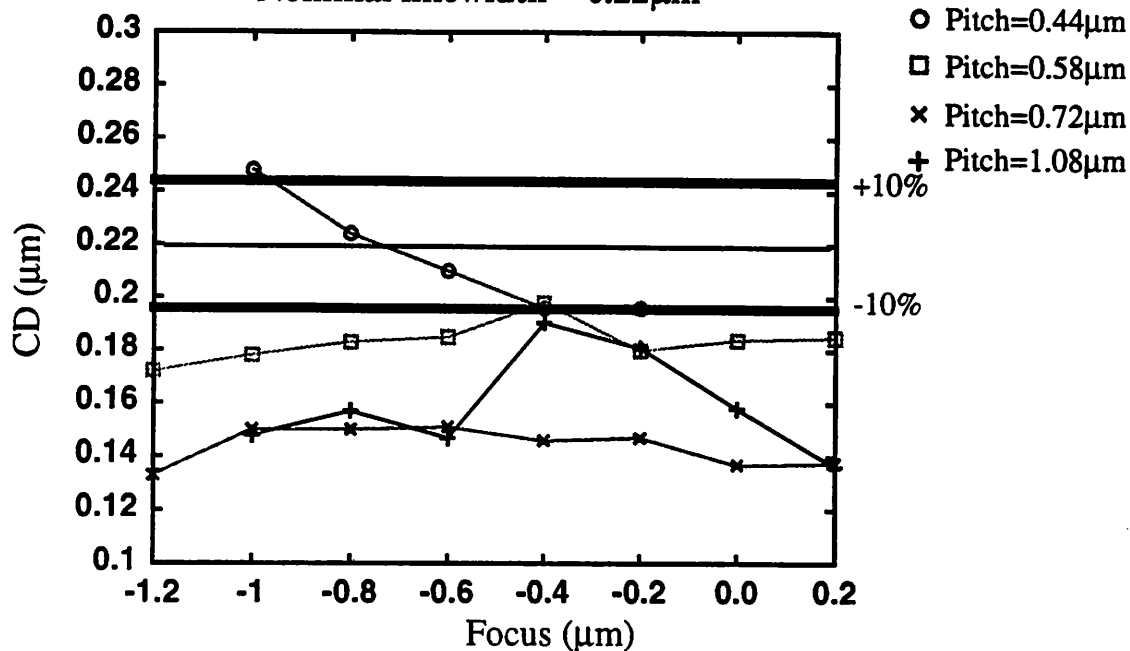


Figure 5.10 CD vs. focus for the SEM cross-sections in Fig. 5.9. The values are obtained by measuring the critical dimension of the features at the base of the resist. ($\lambda = 248\text{nm}$, $0.6-0.7 \sigma$, 0.53NA , $1.0\mu\text{m}$ thick APEX-E)

5.7 Physical Explanation of the Proximity Effect

One clue to the proximity effect can be found by examining the aerial image. The CD vs. focus plot predicted by SPLAT is shown in Fig. 5.11. The change in critical dimension predicted by this analysis is approximately 10nm. Although the basic aerial image is certainly part of the problem, the fact that only 1/6 of the effect can be explained means that other physical phenomena are important.

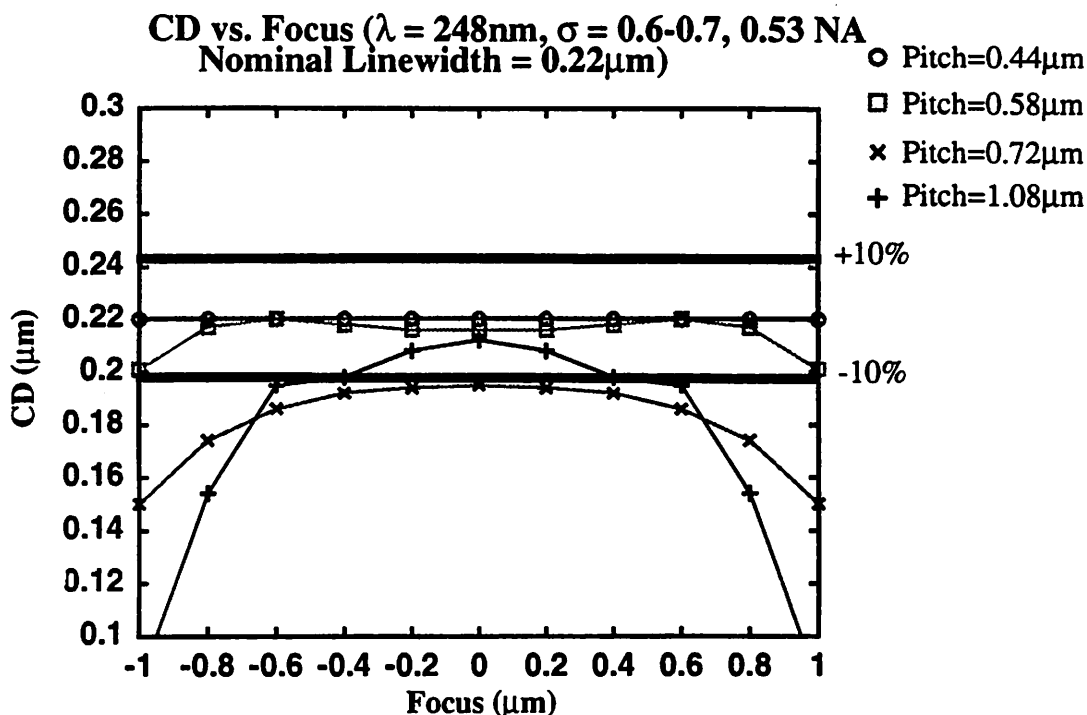


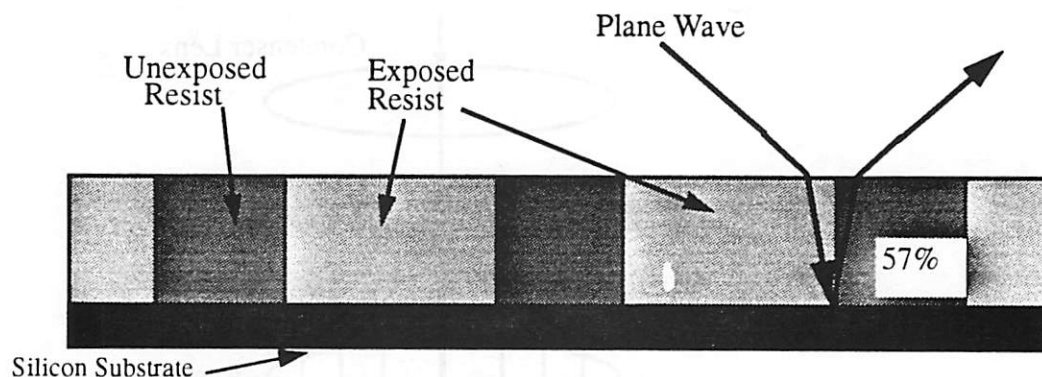
Figure 5.11 CD vs. focus from SPLAT simulations of a rim phase-shifting mask with annular illumination. ($\lambda = 248\text{nm}$, $0.6-0.7\sigma$, 0.53NA)

5.8 Silicon Substrate Reflections

Although several explanations for the poor performance of isolated features have been hypothesized [2], we suggest that a high NA effect coupled with the high substrate reflectivity of silicon at DUV wavelengths contributes to the proximity effect for the isolated bright field lines [4]. The key to this explanation is seen by considering the geometrical optics prediction of light propagating from highly oblique angles to the wafer plane. As shown in Fig. 5.12, an off-axis plane wave is incident to the wafer. The off-axis wave will propagate through the resist and reflect at the silicon surface. The reflectance of silicon with a $1.0\mu\text{m}$ thick coating of APEX-E is calculated to be 57% by applying the standard equations found in Born and Wolf [5]. Since the absorption of APEX-E is $0.17/\mu\text{m}$, 84% of the incident light coupled into the resist reaches the silicon surface. The reflected wave, which has ~48% of the original energy, will now expose resist as it propagates back to the surface. Assuming an NA of 0.53, a plane wave from the edge of the aperture stop

will be incident on the wafer with an angle of ~ 32 degrees. After refraction at the resist surface, the angle becomes ~ 17 degrees. Propagation through the $1\mu\text{m}$ thick resist using this ray viewpoint shows that the exiting wave will be as far away as $0.6\mu\text{m}$ from the entry point.

Light Reflecting from Silicon Substrate



- **Reflectance of silicon with a coat of $1\mu\text{m}$ thick APEX-E resist at 248nm is $\sim 57\%$.**

Figure 5.12 The DUV light reflecting from the highly reflective silicon surface may be causing additional exposure of the lines. The effect is stronger for isolated lines than dense lines and spaces since the overall intensity in the clear area near the line is larger. In our experiment, the intensity difference is a factor of 2X.

For conventional illumination, the problem is not serious since the diffracted energy is distributed fairly evenly throughout the pupil; however, the effect is extremely important for off-axis illumination because there is a large concentration of zero order energy in a ring near the edge of the pupil. Conventional illumination of a semi-isolated line is illustrated in Fig. 5.13. As the line becomes more isolated, the number of diffracted orders increases. The amplitudes of each order can be determined from the Fourier decomposition of the mask. The envelope approaches a sinc function as the line becomes completely isolated. The central order, which proceeds through the center of the lens in on-axis illumination, is much stronger than the other diffracted orders. The modulated energy adds just a small background to the zero order. The key difference between on and off-axis illumination is illustrated in Fig. 5.14, which shows that when the illumination source is off-

axis, the central order illuminates points near the edge of the projection lens and consequently approaches the wafer from a point far off-axis. Again, this order has much more energy than the diffracted ones. If a large fraction of the energy arrives from points far off axis, substrate reflection may degrade the linewidth and profiles of isolated features.

Conventional Illumination of Semi-Isolated Line

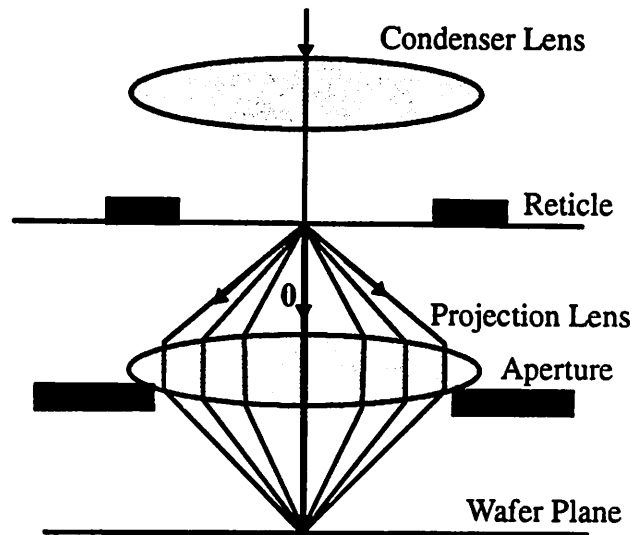


Figure 5.13 Illumination of semi-isolated line. Three diffracted orders are collected within the aperture.

Off-axis Illumination of Semi-Isolated Line

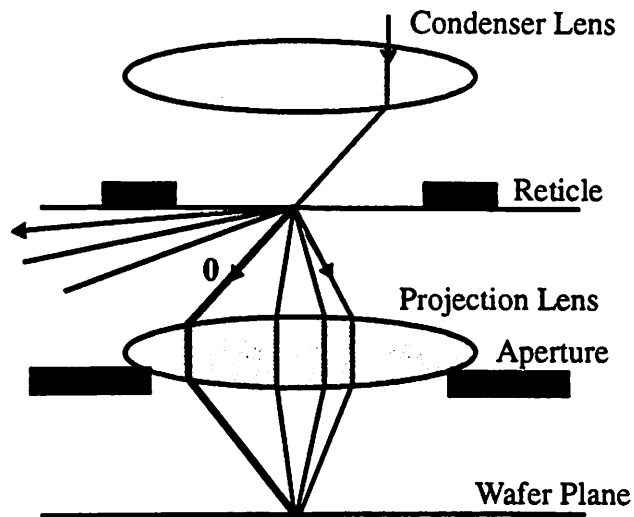


Figure 5.14 Off-axis illumination of semi-isolated line.

To further understand these differences, the energy distribution is calculated across the pupil for both configurations. Fig. 5.15a and 5.15b illustrate the energy distribution in the pupil for conventional illumination with partial coherence of 0.74 and annular illumination with a ring from 0.6-0.7 σ for a 0.16 μm chrome-less rim at a pitch of 1.08 μm . For annular illumination, it is quite obvious that the energy is concentrated in a ring between 0.6 and 0.7. A plane wave originating from this part of the pupil will have an angle of ~ 20 degrees at the surface of the resist and ~ 12 degrees in the resist. Thus, waves at this angle will travel 0.42 μm laterally before leaving the resist. As calculated above, 48% of the light coupled into the resist is reflected at the silicon surface. Since a relatively large exposure is needed to resolve 0.22 μm dense lines and spaces, it is easy to see that the additional exposure caused by the reflected rays could seriously affect the quality of the more isolated lines.

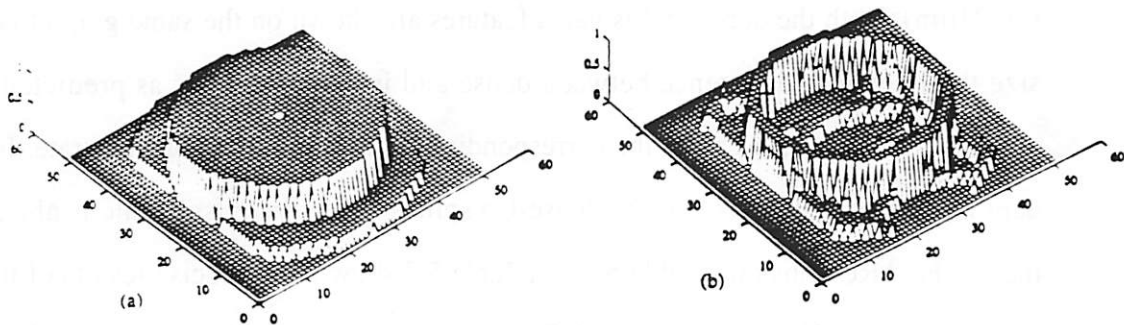


Figure 5.15 (a) Energy distribution in pupil for conventional illumination. (b) Energy distribution for off-axis illumination. The pupil energy is determined by the magnitude of the diffracted orders (see Fig. 5.1) and the distribution of light in the illuminator.

This hypothesis is supported qualitatively by our experimental measurements and SEM micrographs of 0.22 μm lines produced by annular illumination with a binary intensity mask. With annular illumination, isolated 0.22 μm lines break off during develop-

ment, even at best focus. The same size lines with conventional illumination do not break off, although their focus latitude is only $0.4\mu\text{m}$. The combination of these two observations suggests that substrate reflections are indeed important.

Simulation can provide additional understanding of substrate reflections and more quantitative results, so it is used to study this phenomenon in greater detail. Fig. 5.16 shows simulations of the aerial image in $1.0\mu\text{m}$ of APEX-E for an anti-reflective coated (ARC) substrate while Fig. 5.17 illustrates a similar set of simulations for a silicon substrate. The simulations are obtained using Thin-Film SPLAT [6]. The image is focused $1/3$ of the way through the resist to simulate best focus. Only a single intensity level is shown in Fig. 5.18 to illustrate the critical dimension difference predicted by the aerial images over the ARC substrate. The intensity level is chosen such that the optical image predicts the actual dimension of the coded $0.22\mu\text{m}$ dense lines and spaces at best focus ($-0.21\mu\text{m}$). Both the dense and isolated features are shown on the same graph to emphasize the linewidth difference between dense and isolated features as predicted by the aerial image. Fig. 5.19 shows the corresponding result for the silicon substrate. It is evident in these simulations that the dense-iso split for the silicon substrate is about twice that of the ARC substrate. Table 5.1 and Table 5.2 show more precise results of the critical dimension differences for the ARC substrate and silicon substrate, respectively. The CD difference at the bottom of the resist for dense and isolated lines is 8nm for the ARC substrate while it increases to 21nm for the silicon substrate. Thus, surface reflections caused by the silicon substrate account for 13nm or $1/6$ of the proximity effect, and, in total, aerial image effects account for $1/3$ of the proximity effect, or 21nm .

Contour Plot of Aerial Image Simulations in 1.0 μm APEX-E for ARC Coated Wafer

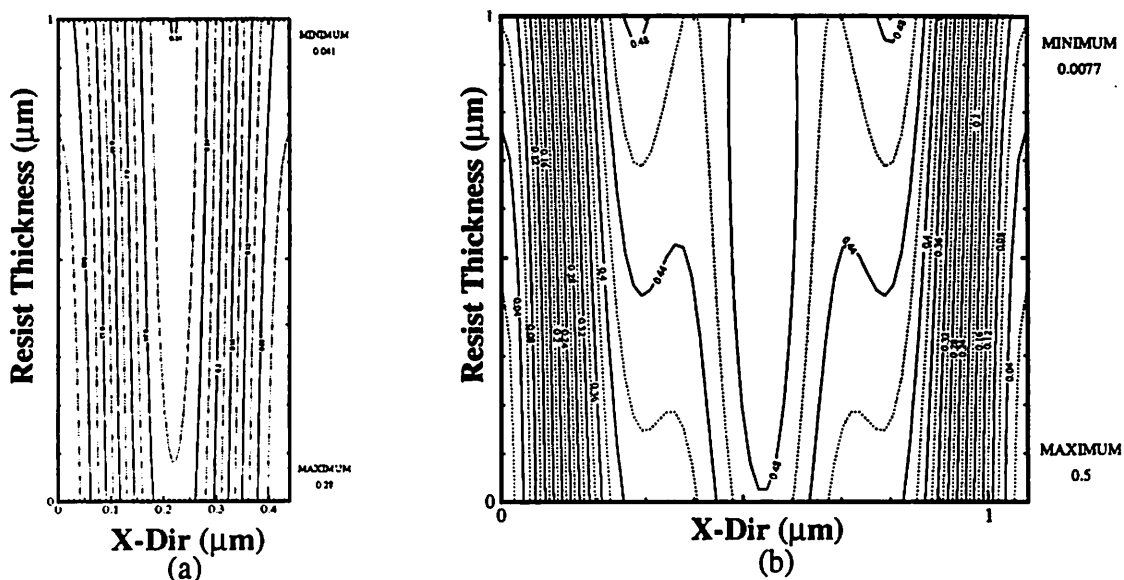


Figure 5.16 Contour plots of aerial image simulations in 1.0 μm of APEX-E for anti-reflective coated substrate. (a) Dense 0.22 μm lines and spaces. (b) 0.22 μm line at a pitch of 1.08 μm . ($\lambda = 248\text{nm}$, 0.6-0.7 σ , 0.53NA, image focused 1/3 through the resist)

Contour Plot of Aerial Image Simulations in 1.0 μm APEX-E for Silicon Wafer

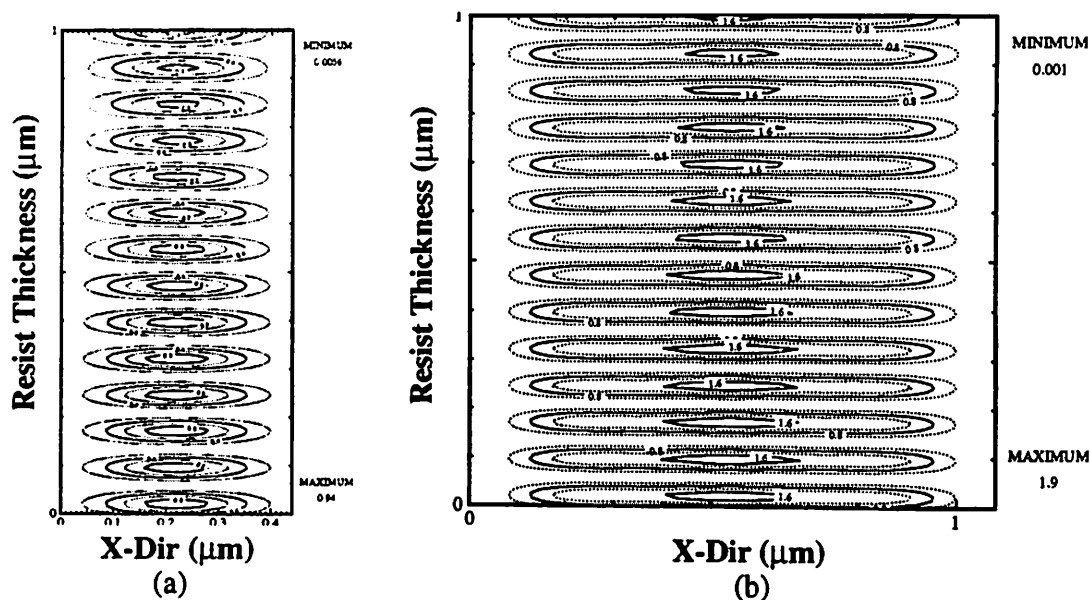


Figure 5.17 Contour plots of aerial image simulations in 1.0 μm of APEX-E for silicon wafers. (a) Dense 0.22 μm lines and spaces. (b) 0.22 μm line at a pitch of 1.08 μm . ($\lambda = 248\text{nm}$, 0.6-0.7 σ , 0.53NA, image focused 1/3 of the way through the resist)

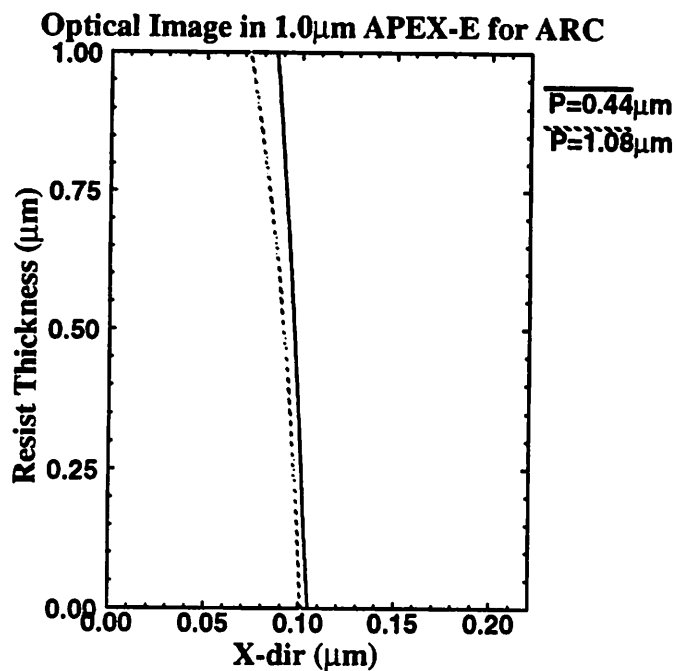


Figure 5.18 Optical image of dense and semi-isolated lines for a rim phase-shifting mask with annular illumination in 1.0 μm of APEX-E for a non-reflecting substrate at a specific intensity level. The linewidth difference at the bottom of the image predicts almost no dense-iso split.

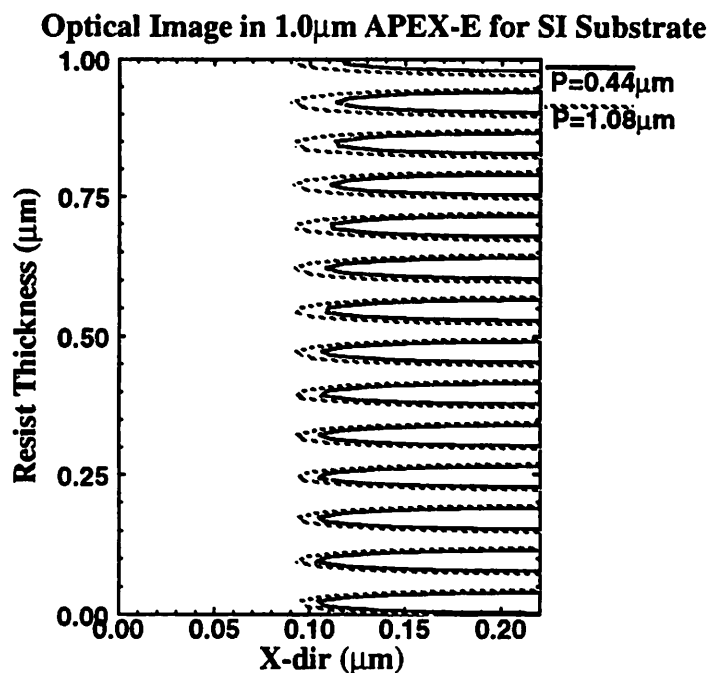


Figure 5.19 Optical image of dense and semi-isolated lines for a rim phase-shifting mask with annular illumination in 1.0 μm of APEX-E for a silicon substrate at a specific intensity level. The linewidth difference at the bottom of the image predicts a larger dense-iso split for the silicon substrate compared to the ARC substrate.

Table 5.1. Optical Simulation Prediction of Dense-Iso Split on ARC Substrate

| Resist Level | Intensity Contour | CD (μm) | |
|--------------|-------------------|---------------------------|---------------------------|
| | | Pitch= 0.44 μm | Pitch= 1.08 μm |
| middle | 0.153 | 0.210 | 0.194 |
| bottom | 0.141 | 0.210 | 0.202 |

Table 5.2. Optical Simulation Prediction of Dense-iso Split on Silicon Substrate

| Resist Level | Intensity Contour | CD (μm) | |
|--------------|-------------------|---------------------------|---------------------------|
| | | Pitch= 0.44 μm | Pitch= 1.08 μm |
| middle | 0.495 | 0.210 | 0.185 |
| bottom | 0.504 | 0.210 | 0.189 |

5.9 Acid Diffusion in APEX-E

Although substrate reflections partially explain the proximity effects, the difference between image simulation and resist profiles is still not fully resolved. In fact, 2/3 of the proximity effect cannot be explained using the substrate reflection model. However, it is possible that acid diffusion in APEX-E can explain the remainder of the proximity effect [7]. Zuniga observed enhanced diffusion in APEX-E for increasing bake times. In fact, linewidth changes of 50% were observed for 45 versus 240 second bake times [8]. Typically, one would expect acid diffusion to affect all features uniformly; hence, it would not play a role in the proximity effect, which is the difference in linewidth between feature dimensions for the same processing conditions. However, for aggressive phase-shifting and annular illumination techniques, there may be significantly different initial acid concentrations for dense versus isolated lines. As shown previously in Fig. 5.17, the peak aerial image intensity of the dense lines is only 0.9 while the peak of the isolated lines is 1.9, a factor of nearly 2X. Since the acid concentration is proportional to the peak aerial image intensity, there are dramatically different acid concentrations between these two features. If a type II diffusion front moves through t-BOC material during post exposure bake, variations in initial acid concentration could influence the eventual feature dimensions. This possibility is examined using the APEX-E resist model in [8] with exponentially dependent diffusion.

The 2-D acid diffusion effects for APEX-E are simulated using the aerial images of Fig. 5.17. A sample set of results is shown in Fig. 5.20. The simulation gives the activated sites for dense and isolated lines for a bake time of 30 seconds. The deprotection level corresponding to the actual dimension of the dense lines and spaces, $0.21\mu\text{m}$ at best focus, is extracted and used to calculate the linewidth for the isolated line. Using this technique, Fig. 5.21 is created to illustrate the predicted linewidth difference between dense and isolated features for a bake time of 30 seconds. Fig. 5.22 shows that the prox-

imity effect increases with bake time. Since acid diffusion is believed to be the primary factor in the linewidth change between dense and isolated features, we compared acid diffusion results for no diffusion and exponential diffusion in Table 5.3 and Table 5.4. Table 5.3 shows the calculated dense-iso split for no acid diffusion. The results clearly show that the dense-iso split remains unchanged. On the other hand, Table 5.4, which summarizes the dense-iso split for exponential diffusion, illustrates the increasing severity of the proximity effect with bake time.

Contour Plots of Activated Sites for 1.0 μm of APEX-E on Silicon Wafer

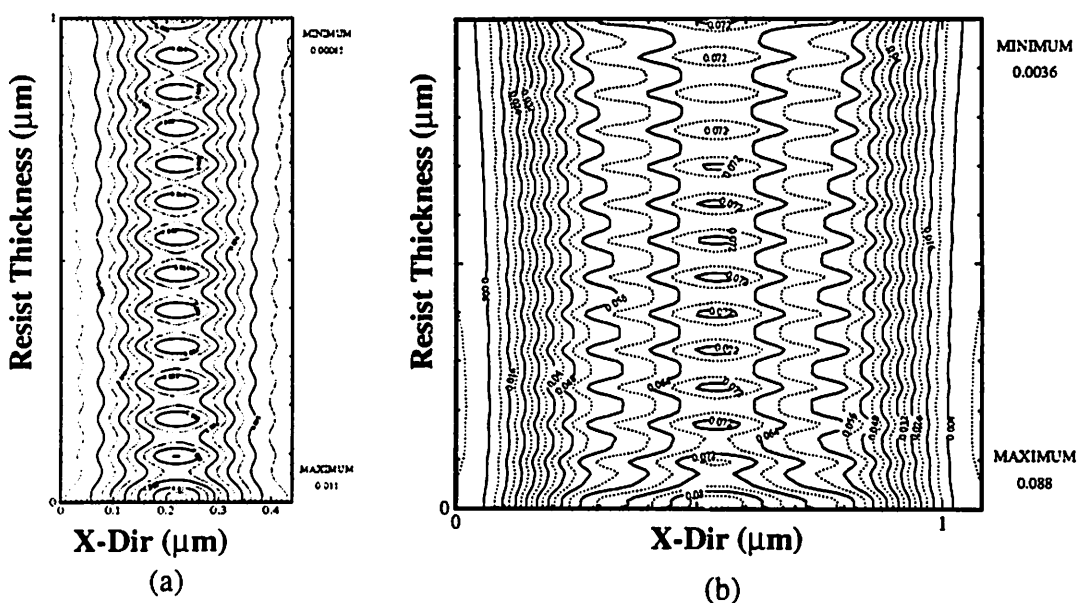


Figure 5.20 Contour plots of the activated sites for 1.0 μm of APEX-E on a silicon wafer. (a) 0.44 μm dense lines and spaces. (b) 0.22 μm line at pitch of 1.08 μm .

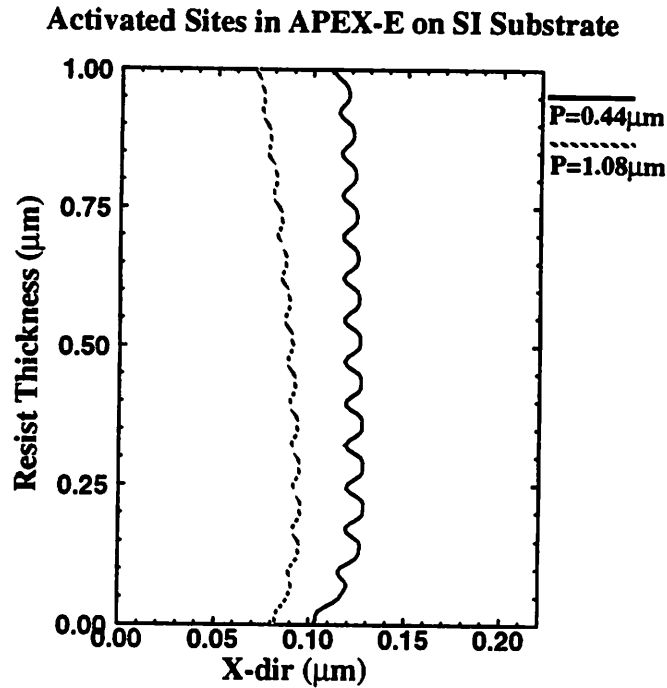


Figure 5.21 Critical dimension change between dense and isolated lines for $0.22\mu\text{m}$ features for 30 second bake time.

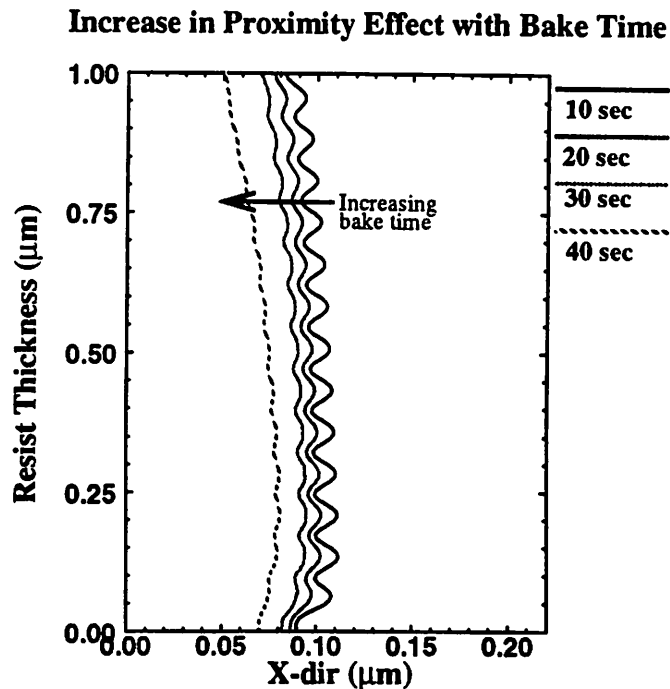


Figure 5.22 Change in the critical dimension of the isolated line (pitch = $1.08\mu\text{m}$) with increasing bake time for a deprotection level which corresponds to that of $0.21\mu\text{m}$ lines for dense lines and spaces.

TABLE 5.3. Dense-Iso Split for No Acid Diffusion

| Bake Time (sec) | Resist Level | Contour Level | CD (μm) | |
|-----------------|--------------|---------------|--------------------------|--------------------------|
| | | | pitch=0.44 μm | pitch=1.08 μm |
| 10 | middle | 0.00864 | 0.210 | 0.184 |
| | bottom | 0.00888 | 0.210 | 0.188 |
| 20 | middle | 0.0172 | 0.210 | 0.184 |
| | bottom | 0.0177 | 0.210 | 0.188 |
| 30 | middle | 0.0257 | 0.210 | 0.184 |
| | bottom | 0.0298 | 0.210 | 0.188 |
| 50 | middle | 0.0425 | 0.210 | 0.184 |
| | bottom | 0.0436 | 0.210 | 0.188 |

TABLE 5.4. Dense-Iso Split for Exponential Acid Diffusion

| Bake Time (sec) | Resist Level | Contour Level | CD (μm) | |
|-----------------|--------------|---------------|--------------------------|--------------------------|
| | | | pitch=0.44 μm | pitch=1.08 μm |
| 10 | middle | 0.00316 | 0.210 | 0.176 |
| | bottom | 0.00451 | 0.210 | 0.182 |
| 20 | middle | 0.00656 | 0.210 | 0.167 |
| | bottom | 0.00843 | 0.210 | 0.175 |
| 30 | middle | 0.0100 | 0.210 | 0.154 |
| | bottom | 0.0123 | 0.210 | 0.166 |
| 50 | middle | 0.0169 | 0.210 | 0.123 |
| | bottom | 0.0197 | 0.210 | 0.141 |

References for Chapter 5

- [1] T.A. Brunner, "Rim phase-shift mask combined with off-axis illumination: a path to $0.5 \lambda/NA$ geometries," *SPIE: Optical/Laser Microlithography VI*, pp. 54-62, March 1993.
- [2] K. Kamon et al., "Photolithography system using a combination of modified illumination and PSM," *Jpn. J. Appl. Phys.*, Vol. 31, p. 4131, 1992.
- [3] W.N. Partlo, P.J. Tompkins, P.G. Dewa, P.F. Michaloski, "Depth of Focus and Resolution Enhancement for i-line and deep-UV Lithography Using Annular Illumination," *SPIE: Optical/Laser Microlithography VI*, pp. 137-157, March 1993.
- [4] D. L. Fehrs, H. B. Lovering, R. T. Scruton, "Illuminator Modification of an Optical Aligner," *Proceedings of the KTI Microlithography Seminar Interface '89* (KTI Chemicals, San Diego, 1989), p. 217.
- [5] M. Born and E. Wolf, *Principles of Optics*, Pergamon Press, New York, (1980), p. 51-66.
- [6] Michael S. Yeung, Derek Lee, Robert Lee, and A.R. Neureuther, "Extension of the Hopkins theory of partially coherence imaging to include thin-film interference effects," *SPIE: Optical/Laser Microlithography VI*, March 1993, pp. 452-460.
- [7] David. M. Newmark, Eric Tomacruz, Sheila Vaidya, Andrew R. Neureuther, "Investigation of Proximity Effects for a Rim Phase-Shifting Mask Printed with Annular Illumination," *SPIE Optical/Laser Microlithography VII*, March 1994.
- [8] M. Zuniga, G. Wallraff, E. Tomacruz, B. Smith, C. Larson, W.D. Hinsberg, "Simulation of Locally-Enhanced 3-D Diffusion in Chemically Amplified Resists," *J. of Vac. Sci. and Technol.*, Nov/Dec, 1993.

TABLE 5.3. Dense-Iso Split for No Acid Diffusion

| Bake Time (sec) | Resist Level | Contour Level | CD (μm) | |
|-----------------|--------------|---------------|--------------------------|--------------------------|
| | | | pitch=0.44 μm | pitch=1.08 μm |
| 10 | middle | 0.00864 | 0.210 | 0.184 |
| | bottom | 0.00888 | 0.210 | 0.188 |
| 20 | middle | 0.0172 | 0.210 | 0.184 |
| | bottom | 0.0177 | 0.210 | 0.188 |
| 30 | middle | 0.0257 | 0.210 | 0.184 |
| | bottom | 0.0298 | 0.210 | 0.188 |
| 50 | middle | 0.0425 | 0.210 | 0.184 |
| | bottom | 0.0436 | 0.210 | 0.188 |

TABLE 5.4. Dense-Iso Split for Exponential Acid Diffusion

| Bake Time (sec) | Resist Level | Contour Level | CD (μm) | |
|-----------------|--------------|---------------|--------------------------|--------------------------|
| | | | pitch=0.44 μm | pitch=1.08 μm |
| 10 | middle | 0.00316 | 0.210 | 0.176 |
| | bottom | 0.00451 | 0.210 | 0.182 |
| 20 | middle | 0.00656 | 0.210 | 0.167 |
| | bottom | 0.00843 | 0.210 | 0.175 |
| 30 | middle | 0.0100 | 0.210 | 0.154 |
| | bottom | 0.0123 | 0.210 | 0.166 |
| 50 | middle | 0.0169 | 0.210 | 0.123 |
| | bottom | 0.0197 | 0.210 | 0.141 |

References for Chapter 5

- [1] T.A. Brunner, "Rim phase-shift mask combined with off-axis illumination: a path to 0.5 λ /NA geometries," *SPIE: Optical/Laser Microlithography VI*, pp. 54-62, March 1993.
- [2] K. Kamon et al., "Photolithography system using a combination of modified illumination and PSM," *Jpn. J. Appl. Phys.*, Vol. 31, p. 4131, 1992.
- [3] W.N. Partlo, P.J. Tompkins, P.G. Dewa, P.F. Michaloski, "Depth of Focus and Resolution Enhancement for i-line and deep-UV Lithography Using Annular Illumination," *SPIE: Optical/Laser Microlithography VI*, pp. 137-157, March 1993.
- [4] D. L. Fehrs, H. B. Lovering, R. T. Scruton, "Illuminator Modification of an Optical Aligner," *Proceedings of the KTI Microlithography Seminar Interface '89* (KTI Chemicals, San Diego, 1989), p. 217.
- [5] M. Born and E. Wolf, *Principles of Optics*, Pergamon Press, New York, (1980), p. 51-66.
- [6] Michael S. Yeung, Derek Lee, Robert Lee, and A.R. Neureuther, "Extension of the Hopkins theory of partially coherence imaging to include thin-film interference effects," *SPIE: Optical/Laser Microlithography VI*, March 1993, pp. 452-460.
- [7] David. M. Newmark, Eric Tomacruz, Sheila Vaidya, Andrew R. Neureuther, "Investigation of Proximity Effects for a Rim Phase-Shifting Mask Printed with Annular Illumination," *SPIE Optical/Laser Microlithography VII*, March 1994.
- [8] M. Zuniga, G. Wallraff, E. Tomacruz, B. Smith, C. Larson, W.D. Hinsberg, "Simulation of Locally-Enhanced 3-D Diffusion in Chemically Amplified Resists," *J. of Vac. Sci. and Technol.*, Nov/Dec, 1993.

Chapter 6 2-D Optical Proximity Correction

6.1 Introduction

Although the issues and problems associated with the use of resolution enhancement techniques for 1-D features are difficult, even more complex and interesting concerns arise when optical proximity correction (OPC) is used for 2-D patterns. As discussed in previous sections, optical lithography has never made extensive use of proximity correction because the path chosen for technology improvement so far has been to reduce the wavelength and increase the numerical aperture, which has made OPC unnecessary as the linewidth decreases. However, continued pressure on wavelength reduction has driven stepper costs up, so it is important to consider alternative means for linewidth reduction. Phase-shifting masks and modified illumination are potential candidates for extending stepper lifetimes since they allow existing steppers to print thinner lines. Unfortunately, these techniques require optical proximity correction. This thesis has already shown several examples of why OPC is necessary. Fundamentally, annular illumination and phase-shifting masks work for lower k_1 factors, which translates to stronger interactions between nearby features. Although annular illumination and phase-shifting masks use these diffraction effects to improve the depth of focus and process latitude, they also enhance proximity effects among features.

The linewidth variations caused by optical proximity effects are often greater than the tolerance limits set by process engineers. In many cases, it is necessary to correct the variations by biasing the reticle or adjusting the feature edges differently than the designed mask. The bias is often pattern dependent which means that it is related to the shape of the features and the spatial relation between them. For example, elbow's and T's may be biased differently. Since simulation is currently the only way to calculate image intensity

profiles and predict biases for all types of features, it is necessary to run aerial image simulations of many patterns on the reticle to determine the bias.

6.2 E-beam 2-D Proximity Correction

Since proximity correction in 2-D has been used for many years in e-beam lithography to correct the over-exposure caused by back-scattered electrons from the substrate, it is useful to examine the technique to understand any similarities. In e-beam lithography, “proximity effects” refer to the nonuniform electron exposure received in the resist due to a wide backscattered electron distribution initiated by incident electrons. Thus, the finely focused beam of electrons exposes resist not only in the area intended but also in adjacent areas. The gaussian approximation used for the incident electron beam is shown in Eq. 6.1. It models the electron beam as two Gaussians. The first Gaussian (with “width” β_p) is

$$f_p(r) = k \left[\exp\left(\frac{-r^2}{\beta_p^2}\right) + \frac{\eta\beta_p^2}{\beta_b^2} \exp\left(\frac{-r^2}{\beta_b^2}\right) \right] \quad 6.1$$

the contribution due to the primary electrons while the second Gaussian (with “width” β_b) is the contribution of the backscattered electrons. With this proximity model, the e-beam proximity effect can be mathematically characterized explicitly [1,2]. In fact, the equations have been solved to determine the necessary dose corrections using mainframe computers. In the most fundamental sense, the interactions associated with optical lithography can be modeled with airy disk patterns, which could be considered analogous to the Gaussian functions for e-beam proximity correction. However, since the mathematics associated with these effects are incorporated into aerial image simulators, the thrust of this research is to take an empirical tack towards the problem and use simulation tools to predict the optical equivalent of the interactions calculated in the e-beam case by the two Gaussians.

6.3 Current Research on Optical Proximity Correction

Although the field is still in its infancy and research thrusts may converge over time, current research on optical proximity correction algorithms for large layouts is being pursued along several different avenues with a variety of optimization approaches. The various techniques can be divided into six groups: 1) pixel-based optimization with simulated annealing, 2) edge movement with the bacteria algorithm, 3) large area aerial image simulation, 4) zone-sampling, 5) rule-based, and 6) pattern recognition with polynomial corrections. The pixel-based optimization technique was developed using an algorithm written by Y. Liu at the University of California at Berkeley [3]. That algorithm optimizes the aerial image of a small pattern by dividing it into small pixels which can be phase-shifted by 0, 90, or 180 degrees. Another technique, the bacteria algorithm, also developed by Y. Liu, addresses the fabrication difficulty of pixel patterns [4]. This method only moves edges to create optimized masks. Large area aerial image simulation and optimization is also being studied at Berkeley by N. Cobb. The optimization technique stitches together bias results by moving a window across the layout and optimizing the area inside each window [5]. The disadvantage of this method is that the aerial image simulation program must be sped up by several orders of magnitude to make the technique practical. The zone-sampling technique, developed by Reiger and Stirniman at Precim, relies on sampling theory and H. Gamo's matrix formulation of partial coherence to model the non-linear spatial behavior of the proximity correction. Again, a proximity window is moved across the mask. However, in this algorithm, corrections are made very rapidly for each window since the zone-sampling function can be used to compute the proximity correction directly [6]. The rule-based approach developed at AT&T, Mentor Graphics, and TVT, is based on the notion that any pattern can be corrected from a simple collection of bias rules which describes how a small set of patterns is biased, depending on the periphery. This method is also very fast since the proximity correction can be calculated for each edge with a simple table lookup operation [7]. Each of these techniques use varying

degrees of mathematical rigor and physics to achieve the desired trade-off in accuracy and performance.

The optimization methods have the common disadvantage that they try to optimize all aspects of every pattern on the mask when it may be necessary to optimize only a small subset of the patterns. In fact, the designer may know exactly which kinds of patterns should be fixed, and it would be useful to use that information since it will reduce mask complexity and optimization time. The last technique, pattern recognition with polynomial corrections was developed to fill this void and can be applied in a way to fully correct a mask. In this chapter, the general pattern recognition method for full mask correction will be described and some interesting observations about the strength and angular dependence of proximity effects will be pointed out. Actual applications of the technique will be discussed in Chapter 7. Since the pattern recognition technique uses results from a pattern optimization algorithm developed specifically for this application, that algorithm will be described first.

6.4 Edge-Nibbler Algorithm for Optical Proximity Correction of Small Layouts

Our approach to optical proximity correction of small layouts was developed because no other optimization method could be easily integrated into the system we planned for full mask correction. The bias algorithm is based on the image alone and therefore assumes a threshold resist model. The intensity threshold corresponds to the pattern the circuit designer expects for the eventual devices. Although the intensity threshold model is inaccurate in some cases, it may be possible to obtain a more exact solution using a resist simulation program such as SAMPLE-3D [8] to find a correction factor which can approximate resist effects to first order. Despite this problem, the algorithm is quite useful since it allows one to calculate a quick bias correction with only five to ten simulations.

The edge-nibbler algorithm consists of two steps or sub-algorithms: pre-bias and local-bias. The need for two steps arose from experimental results which show that when the pre-bias step is left out and the optimization starting point is too far from the desired end point, extraneous features are created in the resulting mask. Therefore, the pre-bias step provides a better starting point for the local-bias algorithm. The diagram describing the pre-bias algorithm is shown in Fig. 6.1. The pre-bias algorithm starts with an initial layout and low pass filters it to remove the sharp edges which cannot be replicated due to diffraction effects. The low pass filter effectively generates a image which is closely related to what one would expect from a high k_1 diffraction limited optical system. Since lithographers currently use these systems to produce extremely high quality images, such images represent a worthwhile objective. Then, SPLAT, the aerial image simulator used in the algorithm, is run to compute the aerial image intensity. A specific intensity threshold is extracted from the SPLAT result, and an error is computed between the mask layout and the extracted intensity threshold at the center of each edge, as shown in Fig. 6.2a. Based on the error, all edges on the mask are moved in the direction that reduces the error. The stopping criteria for the optimization is that either the moving average changes less than a specified tolerance or a limit in the number of iterations is reached.

In the local-bias step, the pre-biased mask pattern is entered into a similar algorithm which divides the edges into smaller segments and adds corner pixels to more closely approximate the desired pattern. Fig. 6.2b shows how the edges are divided into smaller segments which are each biased independently according to the error at the center of each segment. As in the previous case, all corner pixels and edge segments are biased during each iteration to reduce the error at the center of every segment. Convergence is determined by a reduced change in the moving average of the total error. The block diagram for the algorithm is basically the same as the one in Fig. 6.1, except the pre-bias step is replaced by two steps which perform the local-bias of the edges.

Edge-Nibbler Algorithm for Biasing 2-D Mask Patterns

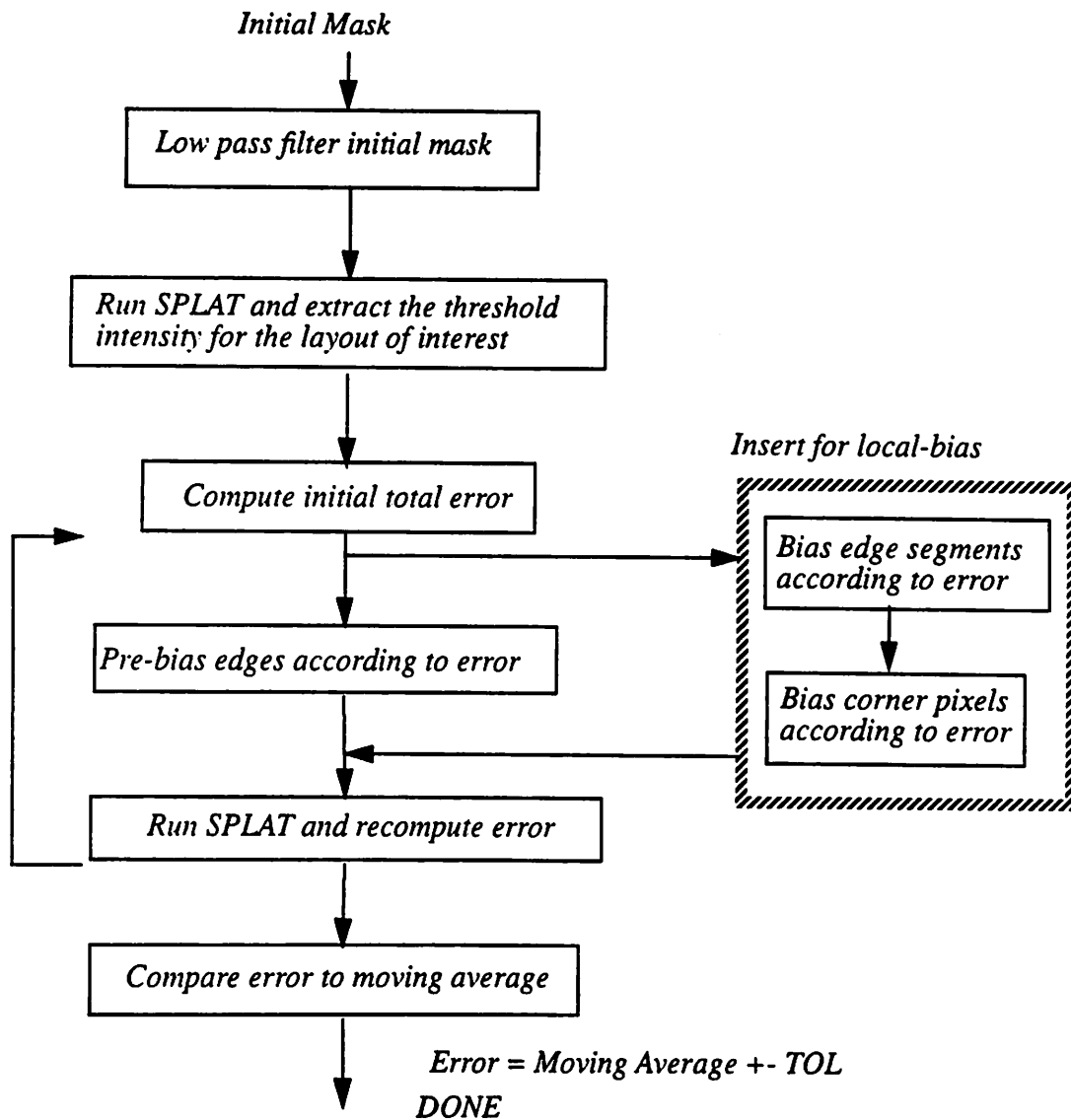


Figure 6.1 Block diagram of algorithm for biasing a mask to correct optical proximity effects.

Variables Used for Optimization

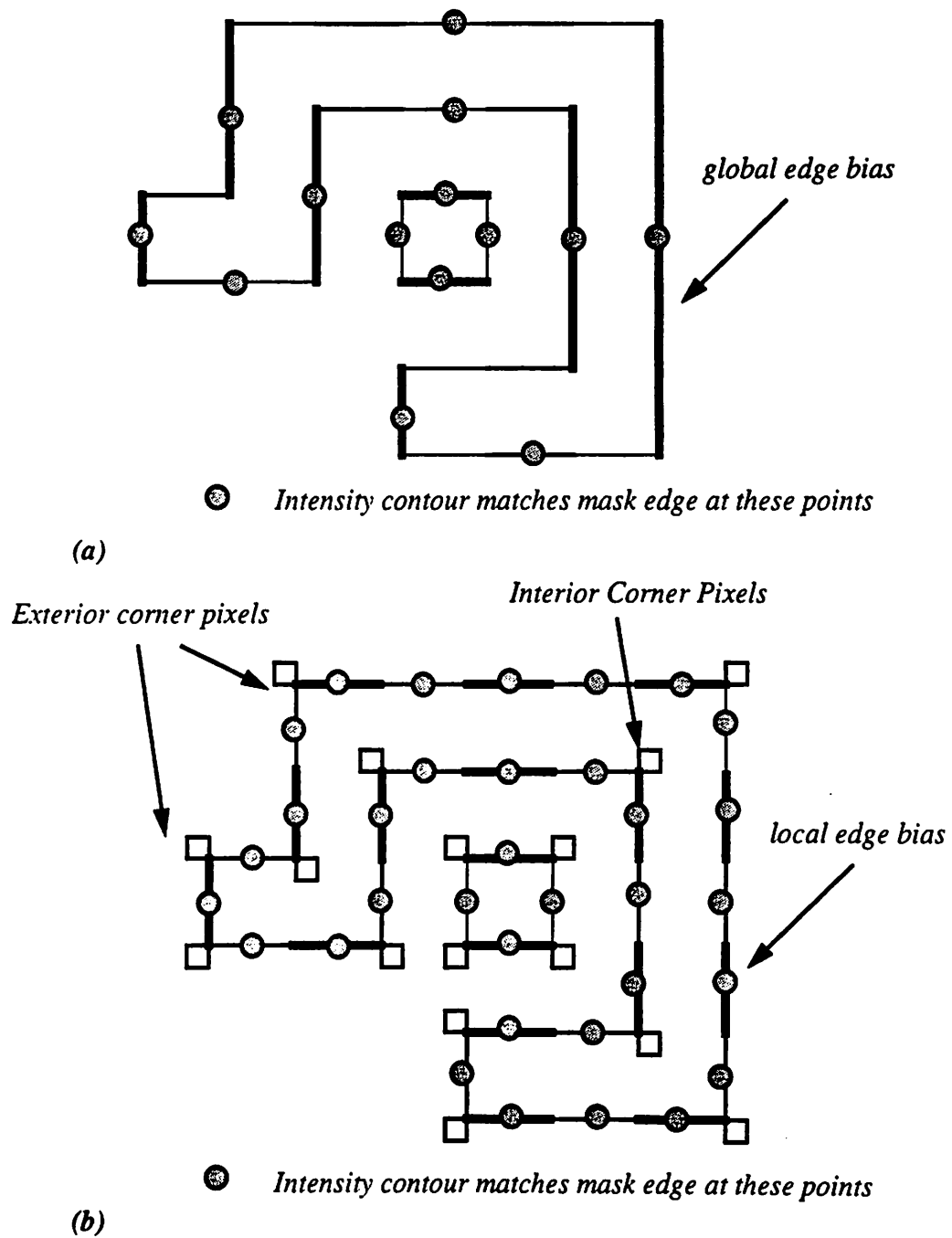


Figure 6.2 Variables used to calculate a complete 2-D optimization of any mask layout. (a) The pre-bias optimization matches the intensity contour at the center of each edge. (b) The local-bias optimization step matches the intensity contour at various locations along the edge. Each edge segment can be moved. In addition corner pixels are added at interior and exterior corners.

A single test mask is used to illustrate both steps of the edge-nibbler algorithm. Fig. 6.3 shows the test mask ($0.25\mu\text{m}$ minimum feature size) while Fig. 6.4 gives the desired and actual contours for the test mask. The intensity contour is the 0.3 intensity level extracted from a SPLAT contour plot. The simulation assumes a 10% attenuating mask illuminated with a DUV ($\lambda=248\text{nm}$) stepper which has 0.53 NA and a ring of annular illumination from 0.6 to 0.7. Note that there is significant foreshortening at the ends of lines and several edges have placement and CD errors.

The pre-bias step of the edge-nibbler algorithm resizes the mask so the contour at the center of each edge in the pattern matches the edge of the mask. The pre-biased mask is shown in Fig. 6.5 and the resulting intensity contour is shown in Fig. 6.6. The result of this optimization illustrates that the shortening at the ends of lines and the line placement and CD errors are corrected. However, the pattern shows little improvement near elbows and corners.

The local-bias step corrects the pattern in these areas. Since it can be executed with edge segments divided into larger or smaller pieces, two examples are shown. Fig. 6.7 gives the optimization result of the local-bias step with an edge segment length of $0.05\mu\text{m}$. Fig. 6.8 shows that this fine local-bias optimization yields intensity results which are quite close to the desired contours. However, the mask is quite exotic and may be difficult to fabricate. Fig. 6.9 is a more practical optimization result obtained with the local-bias step; it uses a $0.25\mu\text{m}$ edge segment length to reduce the complexity. Nevertheless, the intensity contours resulting from the optimization are still quite close to the desired ones as shown in Fig. 6.10. In fact, when the results of the coarse and fine local-bias algorithms are compared, as shown in Fig. 6.11, the coarse local-bias result appears to be nearly as good as the fine-local bias optimization except for some errors near the corners of the pattern.

The time required for each stage of the edge-nibbler bias algorithm is linearly related to the run time for SPLAT. The typical examples shown here require 5-10 iterations to converge on a solution. For a SPLAT run of 3 minutes on a DEC 5000/125, which corresponds to a 2 μ m X 2 μ m mask, it takes about 15-30 minutes to optimize the pattern.

Test Mask for 2-D Optimization

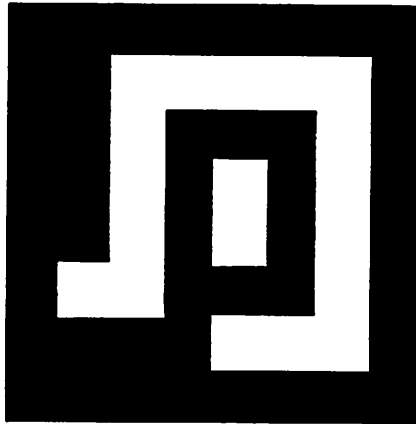


Figure 6.3 Mask of minimum sized features ($0.25\ \mu\text{m}$) used to test the pre-bias and local-bias algorithms.

Desired and Actual Contours for the Test Mask

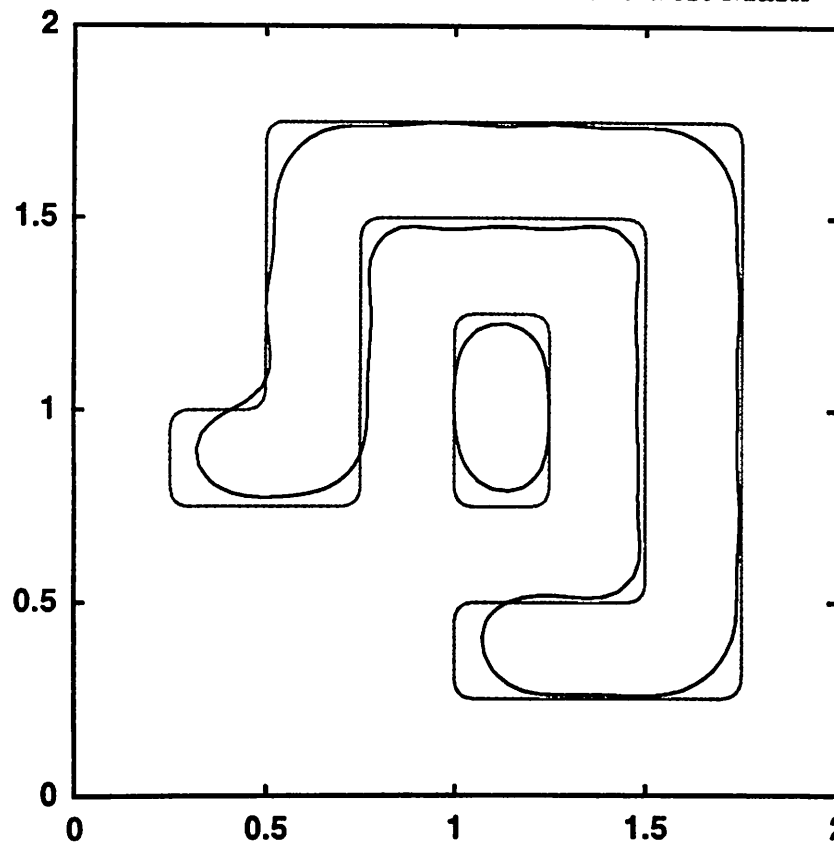


Figure 6.4 Desired and actual contours for the test mask. The outline of the mask is obtained by low-pass filtering the original mask. The intensity contour is determined by extracting the 0.3 intensity level from a SPLAT contour plot. Note the foreshortening at the ends of the lines and the misplacement of some of the edges.

The time required for each stage of the edge-nibbler bias algorithm is linearly related to the run time for SPLAT. The typical examples shown here require 5-10 iterations to converge on a solution. For a SPLAT run of 3 minutes on a DEC 5000/125, which corresponds to a $2\mu\text{m} \times 2\mu\text{m}$ mask, it takes about 15-30 minutes to optimize the pattern.

Test Mask for 2-D Optimization

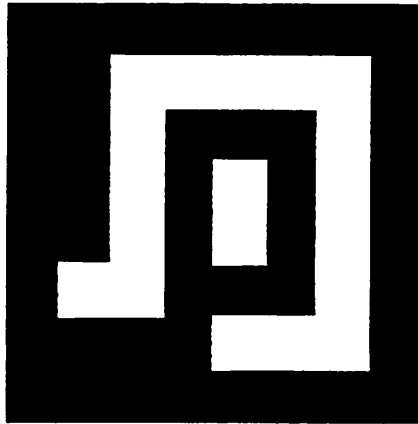


Figure 6.3 Mask of minimum sized features (0.25 μm) used to test the pre-bias and local-bias algorithms.

Desired and Actual Contours for the Test Mask

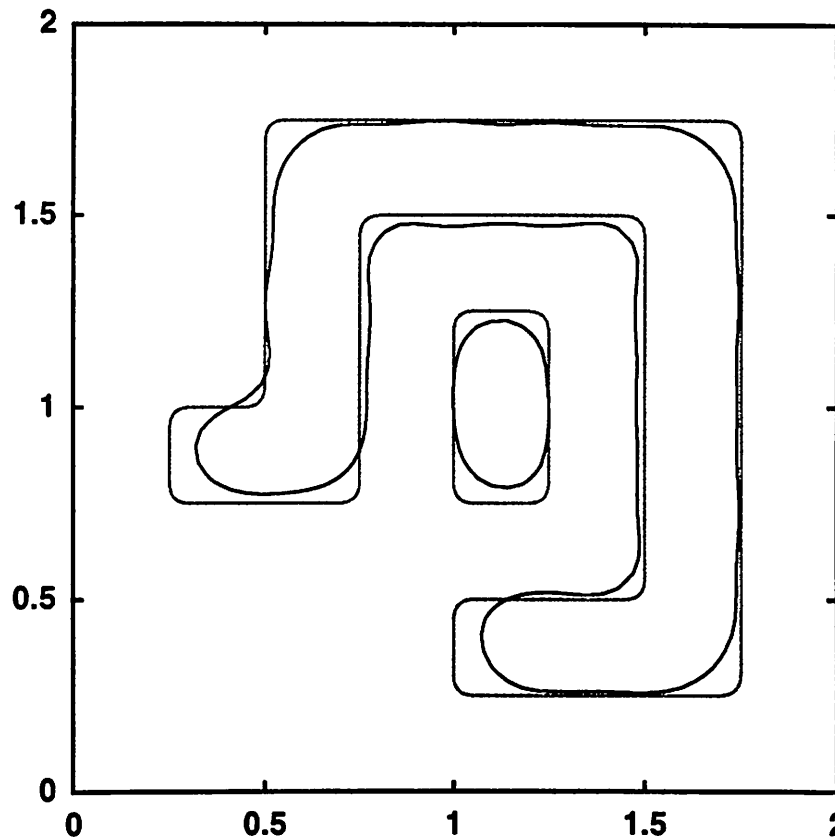


Figure 6.4 Desired and actual contours for the test mask. The outline of the mask is obtained by low-pass filtering the original mask. The intensity contour is determined by extracting the 0.3 intensity level from a SPLAT contour plot. Note the foreshortening at the ends of the lines and the misplacement of some of the edges.

Pattern Obtained with Pre-Bias Algorithm

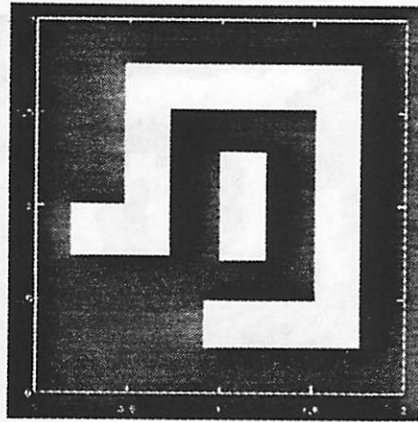


Figure 6.5 Resized pattern which corrects the mask so the intensity level matches the original mask edge.

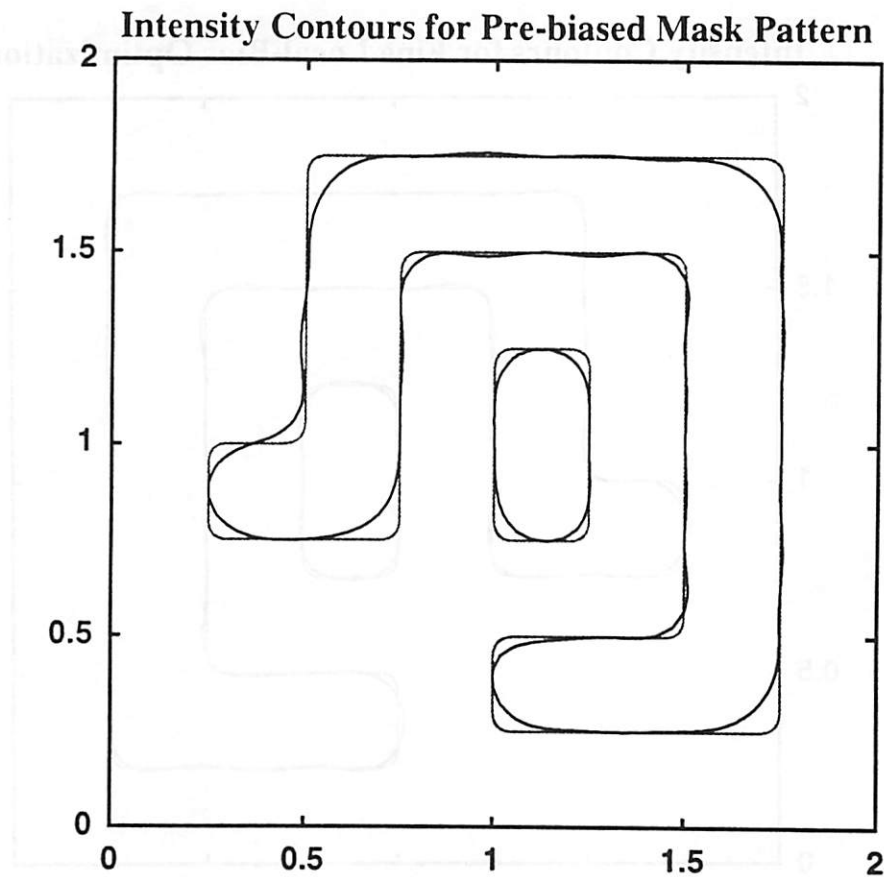


Figure 6.6 Intensity contours now match the mask edge at the center of each edge. These intensity levels are simulated using the mask in Fig. 6.5. The results at this stage are reasonable, but some improvement can be obtained near the corners of the pattern.

Pattern Obtained with Fine Local-Bias Algorithm

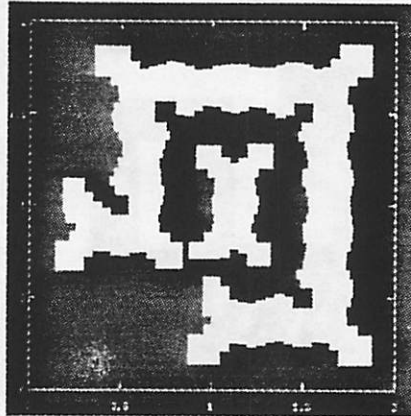


Figure 6.7 Fine local-bias mask pattern resulting from a more rigorous optimization, with an edge segment length of $0.05\mu\text{m}$.

Intensity Contours for Fine Local-Bias Optimization

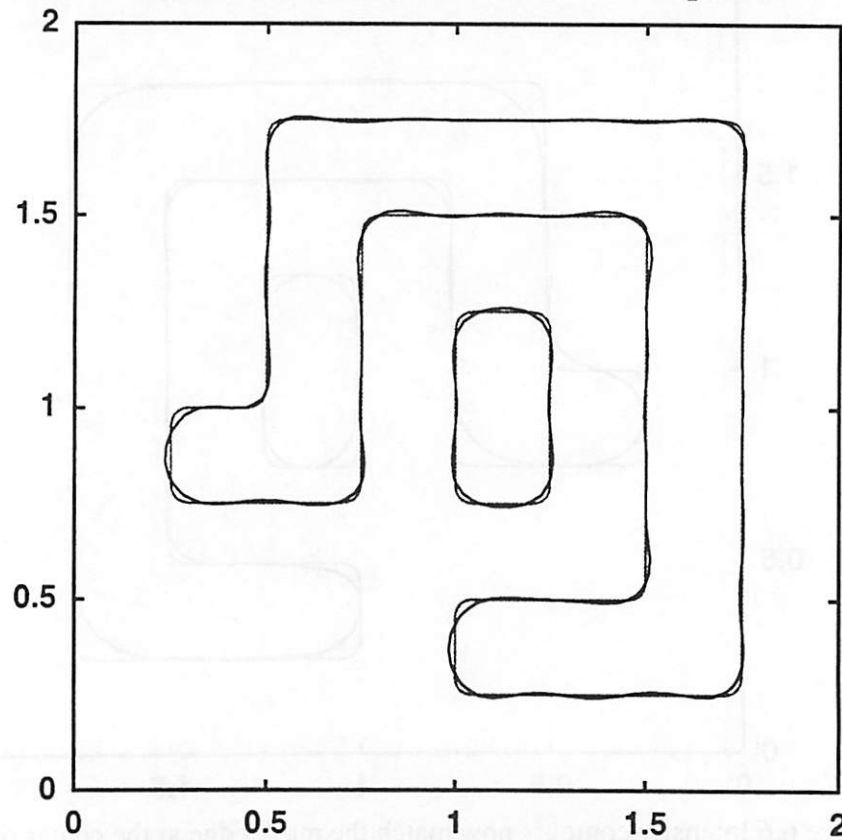


Figure 6.8 Desired and actual contours for fine local-bias optimization. Note that the actual contour and the desired one nearly match at the intensity level where the feature is designed to print.

Pattern Obtained with Coarse Local-Bias Algorithm

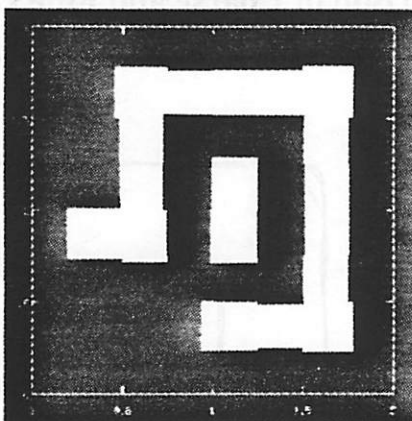


Figure 6.9 Results of coarse local-bias algorithm using an edge segment length of $0.25\mu\text{m}$. The resulting mask is much less complex than the one produced by the fine local-bias algorithm even though the results are nearly as accurate (see Fig. 6.11).

Intensity Contours for Coarse Local-Bias Algorithm

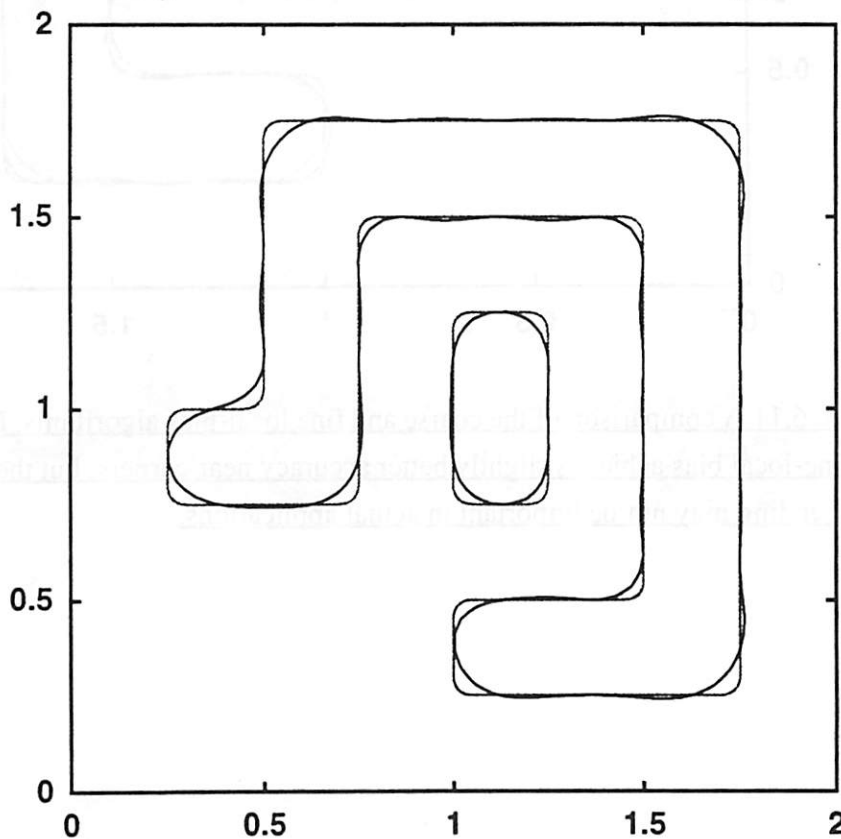


Figure 6.10 Desired and actual intensity contours for the coarse local-bias step of the edge-nibbler algorithm. Note that the accuracy is better than the pre-bias algorithm, but not as good as the fine local-bias algorithm.

Comparison of Coarse and Fine Local-Bias Results

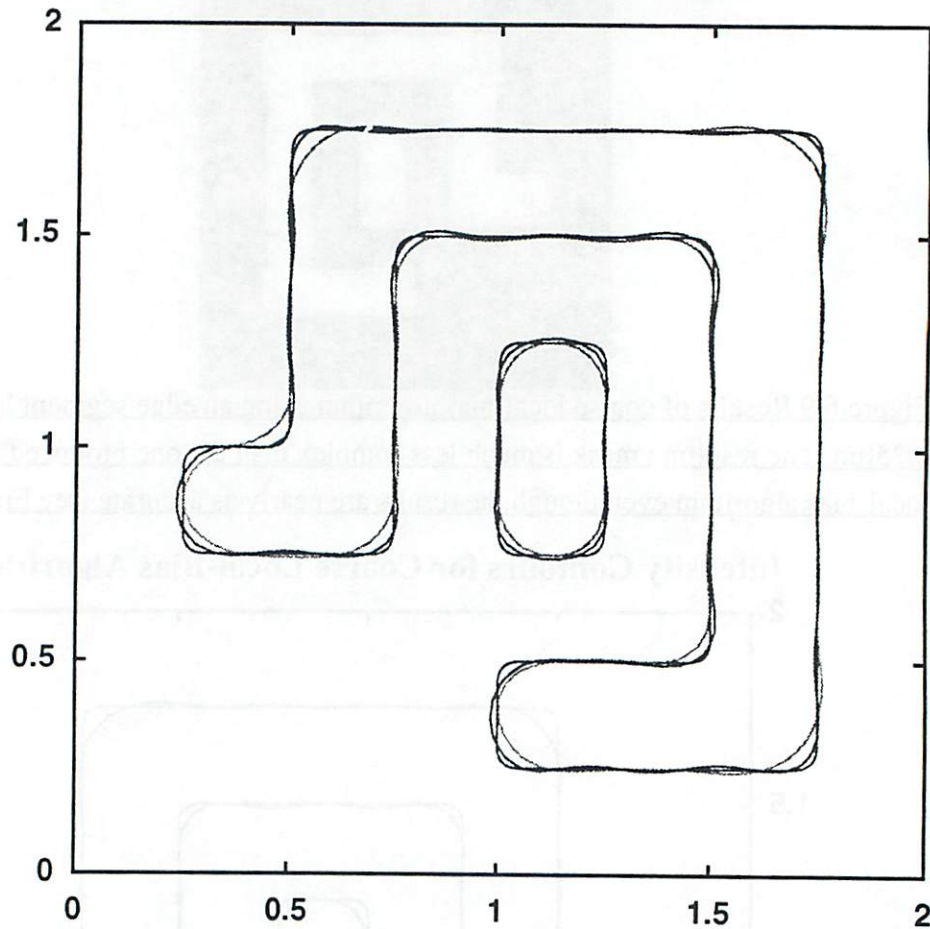


Figure 6.11 A comparison of the coarse and fine local-bias algorithms. For this pattern, the fine-local bias achieves slightly better accuracy near corners, but the elimination of the rounding may not be important in actual applications.

6.5 Concerns with the Edge -Nibbler Algorithm

There are a number of concerns with the edge-nibbler algorithm. First, it is conceivable that the fine or coarse local-bias mask will have inferior depth of focus performance due to the addition of the edge nibbled features. Second, inspecting these masks may be difficult. Third, there is a large increase in data due to the enhanced mask complexity. Finally, fabrication may be a problem.

6.5.1 Depth of Focus Performance

The depth of focus performance for our test mask is examined to determine whether there is any degradation. The cross-sections are taken across the long and short side of the strap in the center of the pattern and across the outside line as shown in Fig. 6.12. The CD versus focus plots are extracted at these locations and shown in Fig. 6.13, Fig. 6.14, and Fig. 6.15. The plots illustrate that the depth of focus is not reduced by either fine or coarse local-biasing.

6.5.2 Mask Inspection

Another concern with edge-nibbled corrections is that the mask may be difficult to inspect. The contour plots in Fig. 6.16, Fig. 6.17 and Fig. 6.18 show the intensity plots seen by a typical mask inspection station. The simulations of the inspection process assumed 488nm light and an NA of 0.85. Fig. 6.16 is the base inspection case with no modifications to the mask. Fig. 6.17 and Fig. 6.18 show the inspection image for finely and coarsely gridded masks respectively. From the contour plots, it is evident that mask inspection is slightly more difficult since there are 0.15 intensity spots in the clear area of the mask. These spots may be interpreted as defects by the inspection system. However, the corners and other changes introduced by the edge-nibbler do not appear to create any additional defects, so the inspection process should not be adversely affected by such masks.

Cut-Lines for Testing Depth of Focus Performance

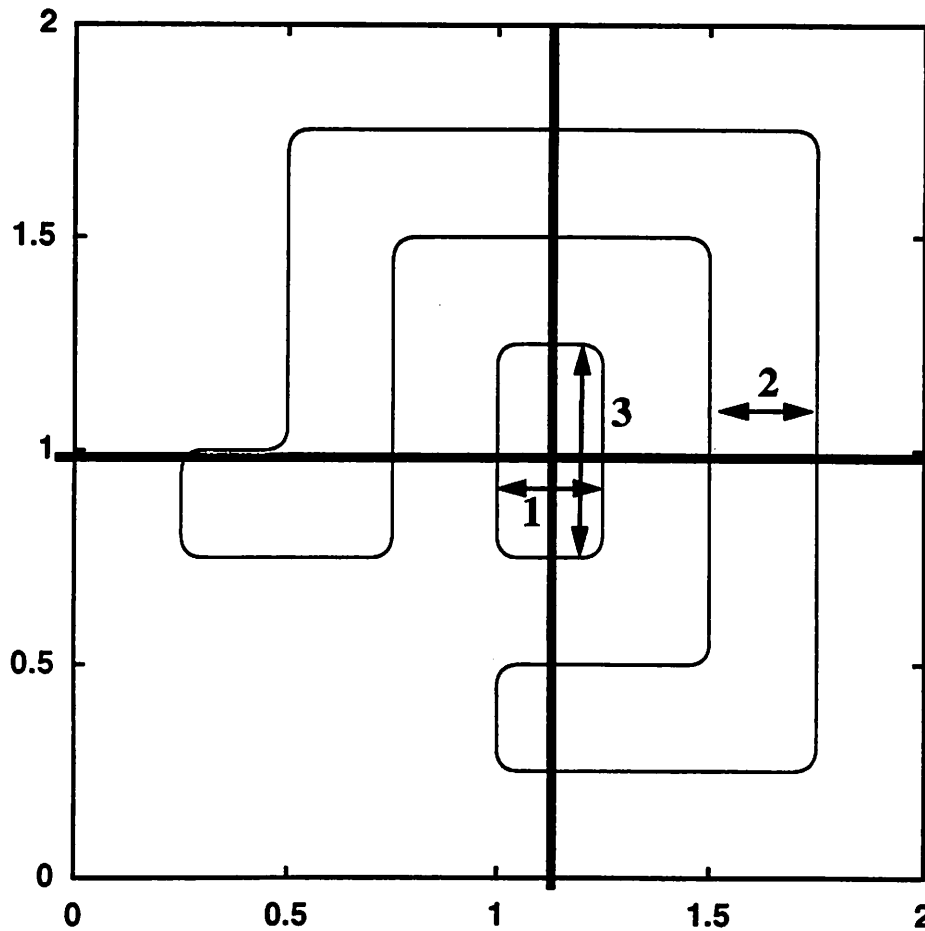


Figure 6.12 Cut lines across the test pattern. The depth of focus at locations 1, 2 and 3 is examined to determine whether the depth of focus of the pattern is degraded by the presence of edge-nibbled features, which were introduced to correct the proximity effect. Simulations use $\lambda = 248\text{nm}$, 0.53 NA, annular of 0.6-0.7, and a 10% attenuating mask.

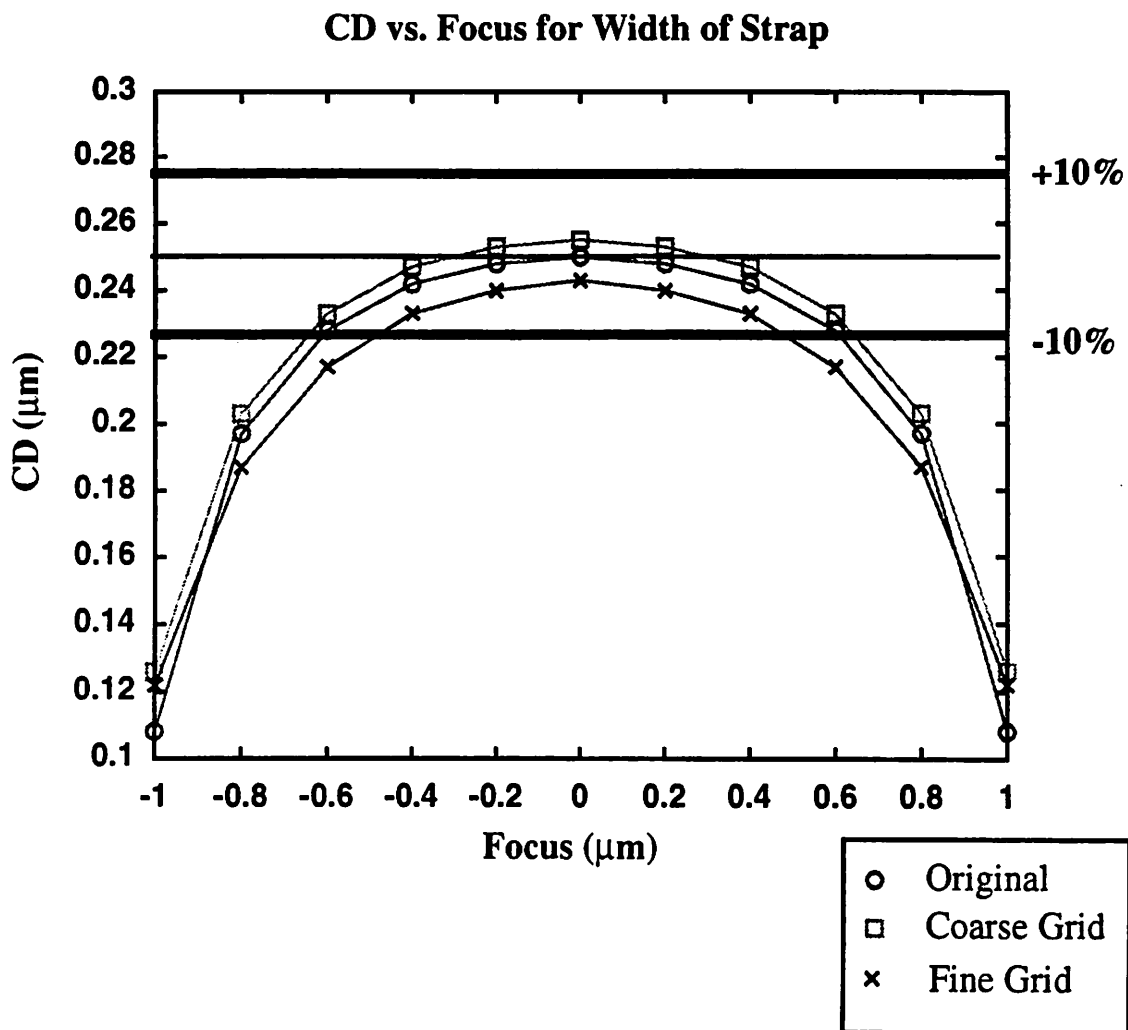


Figure 6.13 Critical dimension versus focus for the width of the strap in the center of the test pattern. The original, coarse and fine-grid solutions were checked for depth of focus performance. The fine grid solution has the worst depth of focus performance, but the coarse grid slightly improves the depth of focus.

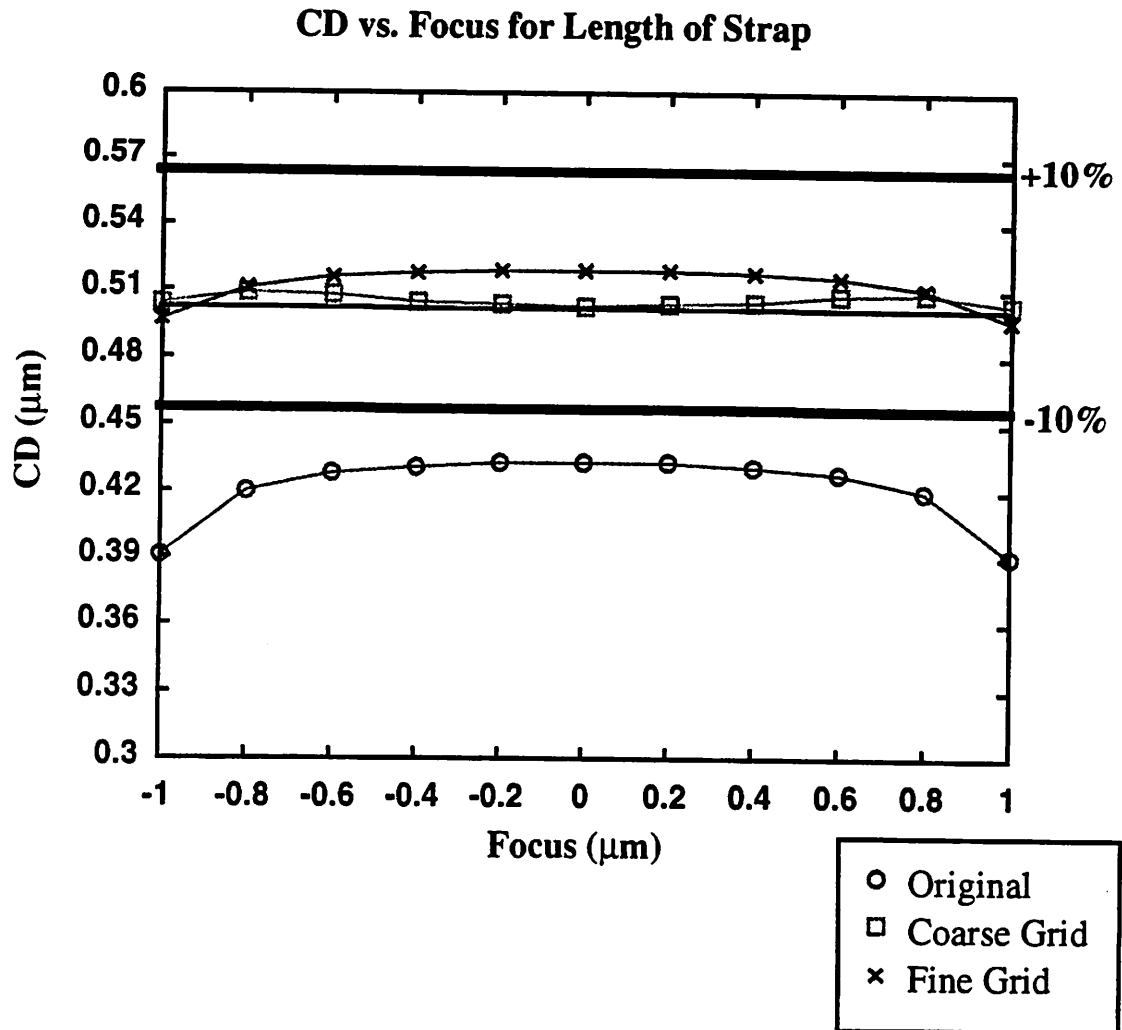


Figure 6.14 Critical dimension versus focus for the length of the strap in the center of the test pattern. The original, coarse and fine-grid solutions were checked for depth of focus performance. Both the fine grid and coarse bias solutions offer similar depth of focus performance. Note that the depth of focus of the uncorrected mask is negligible since the linewidth of out of control due to foreshortening of the feature.

Use of a Pattern Library for Optical Proximity Correction

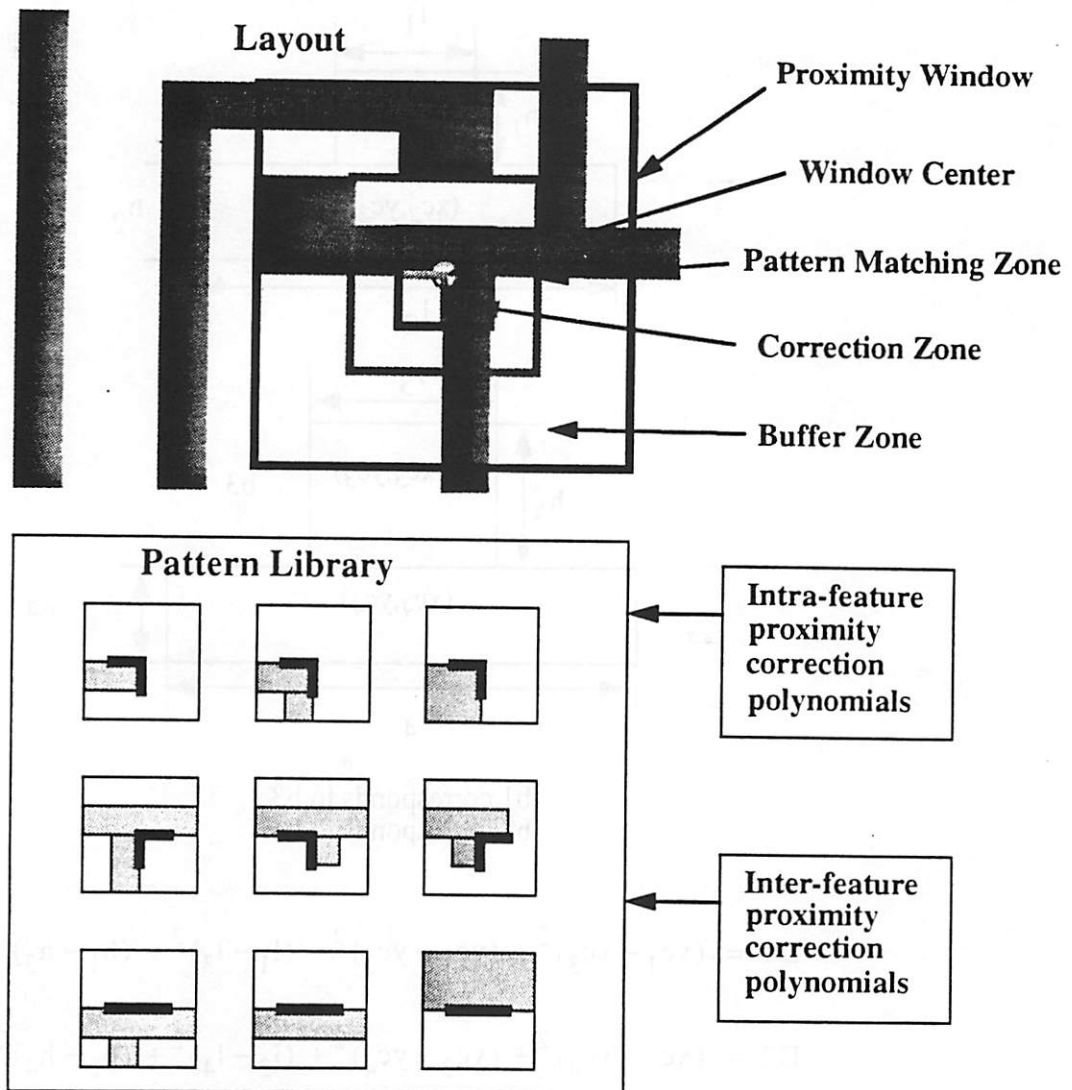
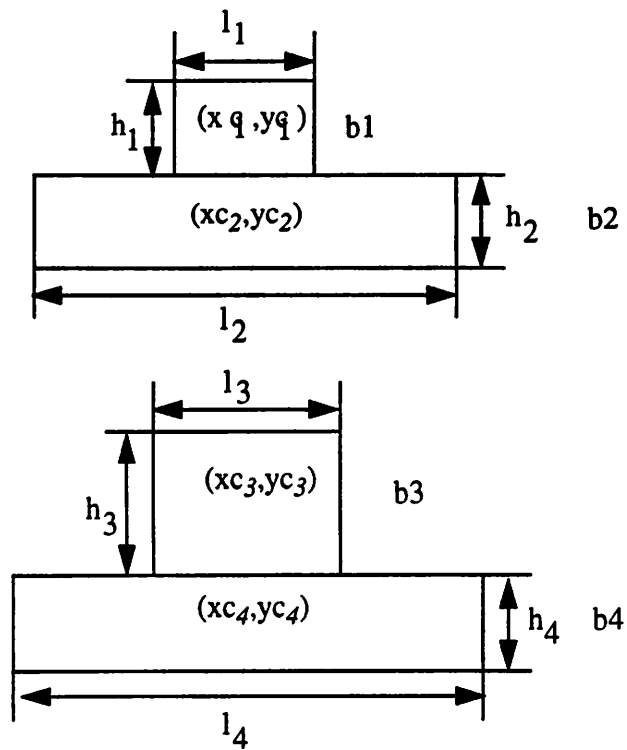


Figure 6.23 Description of the use of a pattern library for optical proximity correction. A proximity window is moved through a layout by attaching the window to corner and edge points in the layout. The area inside the pattern matching zone, the base pattern, is looked up in the pattern library. Intra-feature proximity correction polynomials are used to correct any deviations of the pattern from the one found in the library. Next, inter-feature proximity correction polynomials are used to account for the periphery.

Distance Metric



b1 corresponds to b3
b2 corresponds to b4

$$D1 = (xc_1 - xc_3)^2 + (yc_1 - yc_3)^2 + (l_1 - l_3)^2 + (h_1 - h_3)^2$$

$$D2 = (xc_2 - xc_4)^2 + (yc_2 - yc_4)^2 + (l_2 - l_4)^2 + (h_2 - h_4)^2$$

$$\text{Distance} = D1 + D2$$

Figure 6.24 This distance measure is used to identify which pattern in the library is closest to the one being checked.

References for Chapter 6

- [1] Takayuki Abe, Satoshi Yamasaki, Ryoichi Yoshikawa, and Tadahiro Kakigawa, "Representative Figure Method for Proximity Effect Correction," Vol. 30, No. 3B, March 1991, pp. L528-L531.
- [2] Mihir Parikh, "Self-consistent proximity effect correction technique for resist exposure (SPECTRE)," *J. Vac Sci. Technol.*, 15(3), May/June 1978, pp. 931-933.
- [3] Y. Liu, A.K. Pfau, and A. Zakhor, "Systematic Design of Phase-shifting Masks with Extended Depth of Focus and/or Shift Focus Plane," *SPIE: Optical/Laser Microlithography V*, March 1992.
- [4] Y. Liu and A. Zakhor, "Computer Aided Phase-Shift Mask Design with Reduced Complexity," *SPIE: Optical/Laser Microlithography VI*, pp. 477-493, March 1993.
- [5] Nick Cobb, Avidesh Zakhor, "Large area phase-shift mask design," *SPIE Optical/Laser Microlithography VII*, March 1994.
- [6] J. Stirniman, M. Rieger, "Fast proximity correction with zone sampling," *SPIE Optical/Laser Microlithography VII*, March 1994.
- [7] O Otto, J.G. Garofalo, K.K. Low, C.-M. Yuan, R.C. Henderson, C. Pierrat, R.L. Kostelak, S. Vaidya, "Automated optical proximity correction - a rules-based approach," *SPIE Optical/Laser Microlithography VII*, March 1994.
- [8] John J. Helmsen and Andrew R. Neureuther, "3D Lithography Cases for Exploring Technology Solutions and Benchmarking Simulators," *SPIE: Optical/Laser Microlithography VI*, pp. 382-394, March 1994

Chapter 7 Polynomials for Intra and Inter-Feature Proximity Corrections

7.1 Introduction

The most important aspect of the library-based correction scheme is the development of a method which can use a single base pattern to predict the corrections necessary for a wide variety of features. In the method envisioned in Chapter 6, polynomials fill the role of calculating corrections for patterns different than, but similar to each base pattern. The correction polynomials predict intra-feature and inter-feature proximity effects separately. The intra-feature polynomials describe changes to the bias based on slight variations of the base pattern while the inter-feature polynomials correct the bias for the influence of features in the periphery of the base pattern. This chapter first describes how a polynomial transfer function is developed to predict the bias for patterns with the same structure as the base pattern but with different dimensions. Next, the inter-feature correction polynomials are discussed in order to correct the bias of the base pattern for different features in its periphery. Finally, as an example, the correction polynomials for an end pattern are used to bias a mask obtained from the semiconductor industry.

7.2 Intra-Feature Proximity Correction

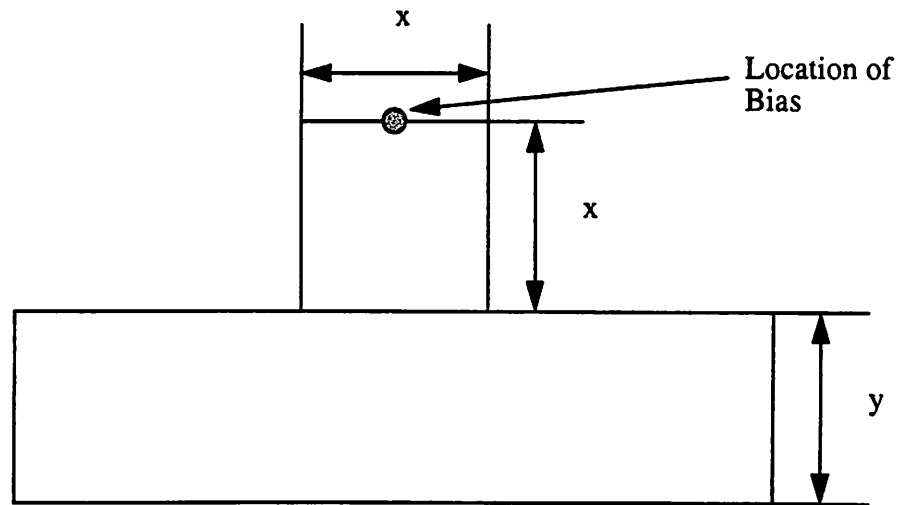
The example in this section shows that a polynomial function can describe the bias needed to correct a cluster of similar patterns. The base pattern shown in Fig. 7.1 is a square stub situated on a line, and the cluster consists of 25 patterns with various stub and line sizes. The artificially created example uses two changing dimensions, namely, the length and width (x) of the stub and the width (y) of the line. The biases for the cluster are calculated using the edge-nibbler bias algorithm discussed in Chapter 6. These biases are

then fit to a 2nd order polynomial using linear regression. The model used for the linear regression is shown in Eq. 7.1

$$\text{Bias} = a_0x^2 + a_1y^2 + a_2x + a_3y + a_4xy + a_5 \quad (7.1)$$

The adequacy of the model is tested by comparing the bias obtained from the model with that obtained from the bias algorithm. The results are shown in Fig. 7.2. They demonstrate that by using the polynomial, it is possible to calculate the bias needed to correct the intra-proximity effect to within $\pm 0.01\mu\text{m}$ ($0.02 \lambda/\text{NA}$). Note that a constant bias applied to all patterns in the cluster would have a bias error of $\pm 0.02\mu\text{m}$ ($0.04 \lambda/\text{NA}$), so the polynomial correction buys a factor of two improvement.

Test Feature for Intra-Feature Proximity Correction



$x = 0.24$ to $0.40\mu\text{m}$ in steps of $0.04\mu\text{m}$
 $y = 0.24$ to $0.40\mu\text{m}$ in steps of $0.04\mu\text{m}$

Figure 7.1 A single cluster of patterns used to test whether intra-proximity effects can be characterized using a polynomial transfer function. There are 25 different patterns in the test set, with different dimensions for x and y .

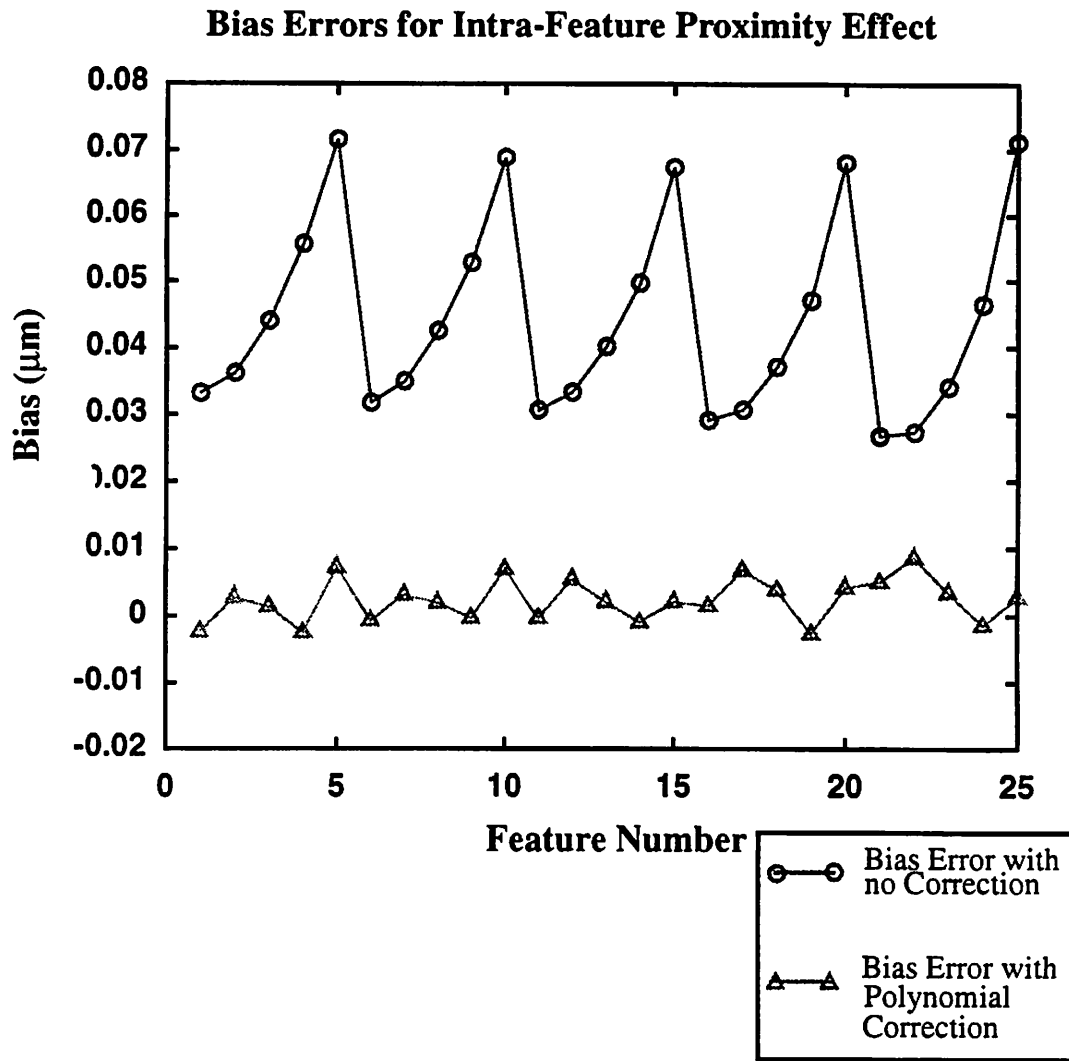


Figure 7.2 Uncorrected and corrected biases calculated from prebias algorithm for the layouts in Fig. 7.1. Note the 2X improvement in total variation of biases using the correction polynomials.

7.3 Overview of Inter-Feature Proximity Corrections

It would be ideal if all patterns could be corrected using intra-feature corrections. Unfortunately, half of the proximity effect arises from inter-feature interactions, which, of course, depend on the surroundings of the base pattern. One way to account for these interactions with a polynomial correction scheme is to use the representative figure

method. The representative figure method is not new to photolithography; in fact, it was originally suggested as a way to improve the speed of e-beam proximity correction [1]. The basic idea is to divide up the layout into an arbitrary number of regions as shown in Fig. 7.3. Within each region, all the rectangles are lumped into a representative rectangle

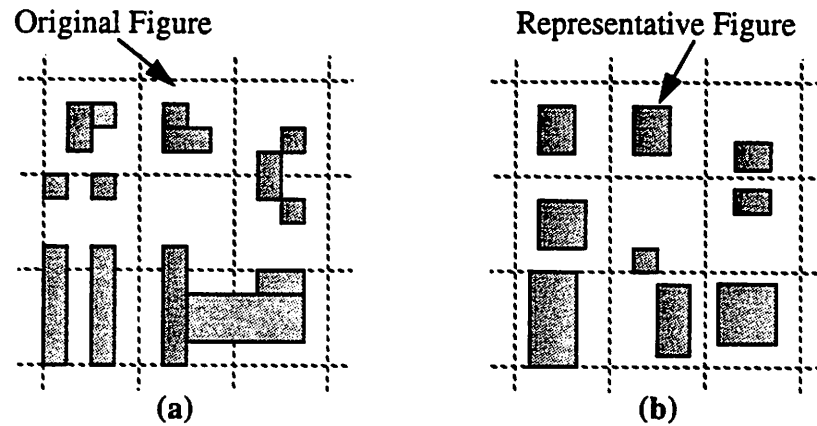


Figure 7.3 The shaded areas in (a) are the original patterns and the representative rectangles are shown in (b) [ref].

which ideally conveys all of the information about the proximity effect of that pattern. As discussed in Chapter 6, the proximity effect for e-beam lithography is caused by backscattered electrons which can cause over-exposure. This effect is modeled as two circularly symmetric Gaussians. For e-beam proximity correction, a mathematical representation for the influence of the representative feature can be derived [1].

The mathematics for optical lithography are, however, highly nonlinear and quite complex. First, the proximity effect can be either additive or subtractive. Second, the partial coherence of the illumination affects the strength and effective interaction distance of the proximity effect. Third, the effect is typically *not* circularly symmetric and cannot be modeled as a Gaussian. Finally, the optical proximity effect is hidden because the electric fields, which cannot be directly observed, are the root cause of the optical proximity effect; the intensity or the square of the electric field is the physically observed quantity.

Despite these dissimilarities with e-beam proximity correction, it is prudent to start optical proximity correction with a simple approach analogous to e-beam lithography and then extend it where necessary. Therefore, an approach is presented in which a training set is used to learn a polynomial which approximates the bias caused by rectangles from each region. Since this polynomial is completely general, it does not prejudge the nature of the optical proximity effect and its variations with position will give insight into the magnitude and sign of the effect. With the polynomial approach used here, the bias due to the periphery is obtained by adding the bias of each representative figure in all the regions in the periphery.

7.3.1 Representative Figure Method

The intuition behind the representative figure method is that the proximity effect of a number of different features can be represented by a single one. The implementation of the idea arises from an example in e-beam lithography and the one used here was initially proposed by Joe Garofalo in the Sematech Phase-Shift Mask Project; it is illustrated in Fig. 7.4. The representative rectangle is simply a weighted average of the length and width of the boxes in the proximity to the main feature. The equations used to find the length and width of the effective rectangle are shown below.

$$W_{\text{eff}} = \frac{W_1L_1 + W_2L_2 + W_3L_3}{L_1 + L_2 + L_3} \quad (7.2)$$

$$L_{\text{eff}} = \frac{W_1L_1 + W_2L_2 + W_3L_3}{W_1 + W_2 + W_3} \quad (7.3)$$

$$D_{\text{eff}} = D_1 \frac{A_1}{A_T} + D_2 \frac{A_2}{A_T} + D_3 \frac{A_3}{A_T} \quad (7.4)$$

$$A_T = A_1 + A_2 + A_3 \quad (7.5)$$

Representative Figure Method for Optical Lithography

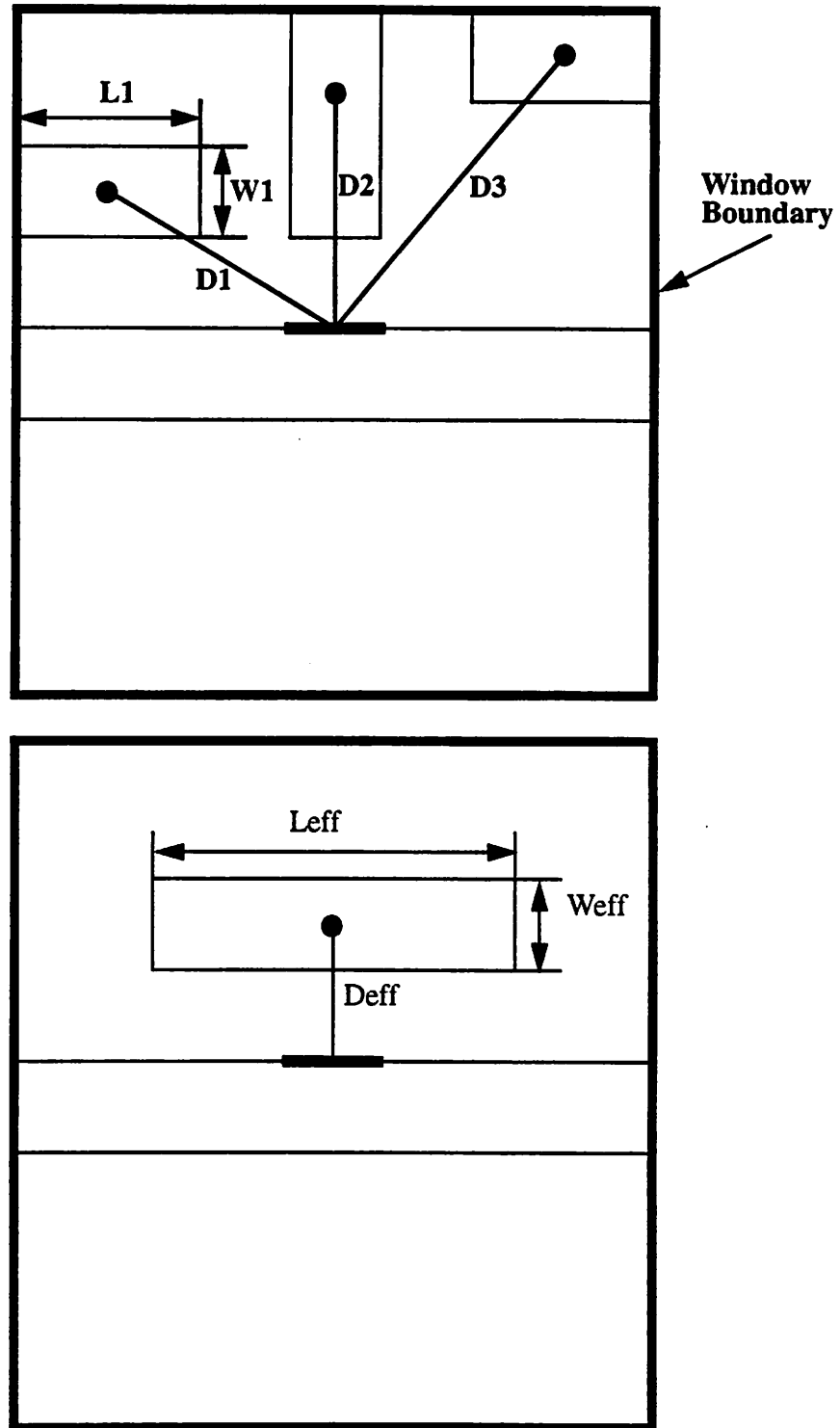


Figure 7.4 Illustration of the representative figure method for optical lithography. The information about several peripheral features is lumped into a single representative one.

7.3.2 Partitioning the Periphery

The implementation of the representative figure method for complicated layouts is a bit more involved than the simple representation shown above since the layout must be partitioned into various regions around the base pattern. The partitioning choice is somewhat arbitrary and will be different depending on the type of feature. For the case of a line, the partitioning choice is simple and requires only a representative region on the top and bottom of the line. However, the vast majority of cases in actual layouts will be more complicated since most base pattern have corners, such as the end of a line. The example of the partitioning chosen for an end is illustrated in Fig. 7.5. The base pattern is an end of

Regions for Correcting Inter-Proximity Effect on Main Feature

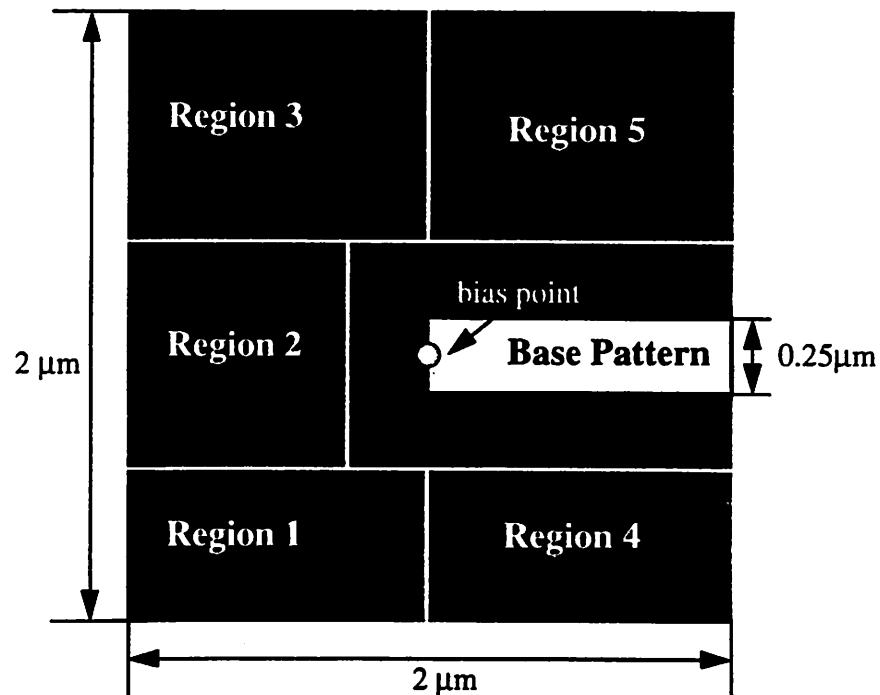


Figure 7.5 Choice of representative figure regions for correcting the proximity effects on the main feature. A representative rectangle is calculated for each region based on the definition shown in Fig. 7.4.

a line. Naturally, the immediate periphery of the end is empty since the nearest feature must be at least $0.25\mu\text{m}$ away from the minimum sized base pattern. The remaining periphery is encompassed in the five representative regions. To illustrate the idea, an original and representative pattern are shown in Fig. 7.6a and Fig. 7.6b.

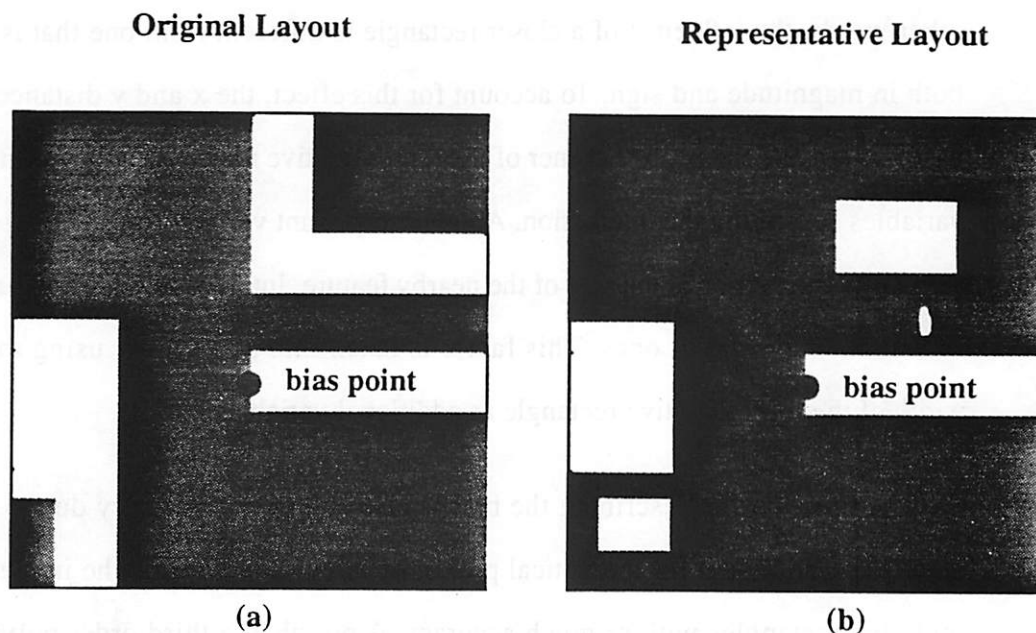


Figure 7.6 Original layout (a) and representative layout (b).

7.3.3 Learning Correction Functions for the Representative Regions

The usefulness of the representative figure method for optical lithography hinges on its ability to predict the change in bias created by the proximity influence of the representative rectangle in each region. One approach to solving this problem is to fit a polynomial to the bias caused by any sized rectangle within each representative region. The remainder of this section describes the variables used in the polynomial, the form of the polynomial function, the training set of examples used to extract the coefficients of the function, and an example of how well the function fits the bias for the end of a line surrounded by different peripheral features. Finally, potential problems with this method are evaluated.

The choice of variables which describe the influence of the single representative rectangle in the region is somewhat arbitrary, but they should somehow describe the size and location of the rectangle. One important criteria for determining the degree of interaction arising from a particular feature is the distance of that feature from the base pattern. In other words, the influence of a closer rectangle is different from one that is farther away both in magnitude and sign. To account for this effect, the x and y distance between the base pattern and the nearest corner of the representative rectangle are chosen as two of the variables describing the interaction. Another important variable determining the degree of proximity interaction is the size of the nearby feature. Intuitively, larger feature have more influence than smaller ones. This factor is taken into account by using the length and width of the representative rectangle as additional variables.

The function for describing the bias is also somewhat arbitrary due to the lack of a good physical model for the optical proximity effect. To describe the influence of representative rectangles with as much accuracy as possible, a third order polynomial in all four variables is used. This polynomial has a total of 33 terms. The coefficients are calculated using a multivariate linear regression based on a training set of examples. The degree of the polynomial requires at least 33 examples to calculate the coefficients for the function and additional examples will improve the accuracy of the model for predicting cases which are different from those used to create the model.

As discussed above, a training set is needed to determine the coefficients of the polynomial function. A training set which covers as many configurations as possible while requiring a minimum of examples is critical since the coverage of the training set determines the accuracy of the bias and the size determines the time needed to simulate all the cases. Our approach assumes that the minimum sized rectangle is a square of the minimum feature size. Anything smaller than that will have an insignificant influence on the main pattern. Given this base size, increments of the rectangle's length and width are used

to systematically cover all variations of box sizes. The value of the increments used to change the box sizes are determined by Eq. 7.6 and 7.7 where ΔX is the increase in the width of the box and ΔY is the increase in the height of the box. Width and height are the dimensions of the representative rectangle, and n_x and n_y are the number of boxes in the x and y directions. Given the importance of location, all the various box sizes are also

$$\Delta X = \frac{(\text{Width} - 0.25)}{n_x} \quad (7.6)$$

$$\Delta Y = \frac{(\text{Height} - 0.25)}{n_y} \quad (7.7)$$

moved throughout the representative region. The location of the boxes is determined by the ΔX and ΔY values. A rectangle of each size is moved to every location within the representative region that falls on a point which is an integer multiple of ΔX and ΔY .

This method of generating training sets is used for the example in Fig. 7.5. For representative region #1, dimensions of $1.0\mu\text{m} \times 0.5\mu\text{m}$, and $n_x = n_y = 3$, $\Delta X = 0.084\mu\text{m}$ and $\Delta Y = 0.25\mu\text{m}$. The size of the starting box is $0.25\mu\text{m} \times 0.25\mu\text{m}$. It is translated to all positions within the representative region that are integer multiple of ΔX and ΔY . After the translation process, the box is lengthened in the y-direction by $0.084\mu\text{m}$ and the placement process is repeated. After increasing the length of the box until it touches the edge of the region, the length is reduced to the minimum of $0.25\mu\text{m}$ and the width is increased by ΔY to $0.5\mu\text{m}$. Again, the positioning process is repeated. The length and width of the box are increased until the box fills the entire region and can no longer be translated to new position because any movement would require some part of box to move outside the region. That set of boxes completes the training set for the region. For this case, there are a total of 90 boxes. The basic configuration of training examples can easily be extended to the other regions.

The biases and polynomial fit functions are calculated for each region. The results for region #1 are shown in Fig. 7.7. The range of biases required to correct the base pattern to

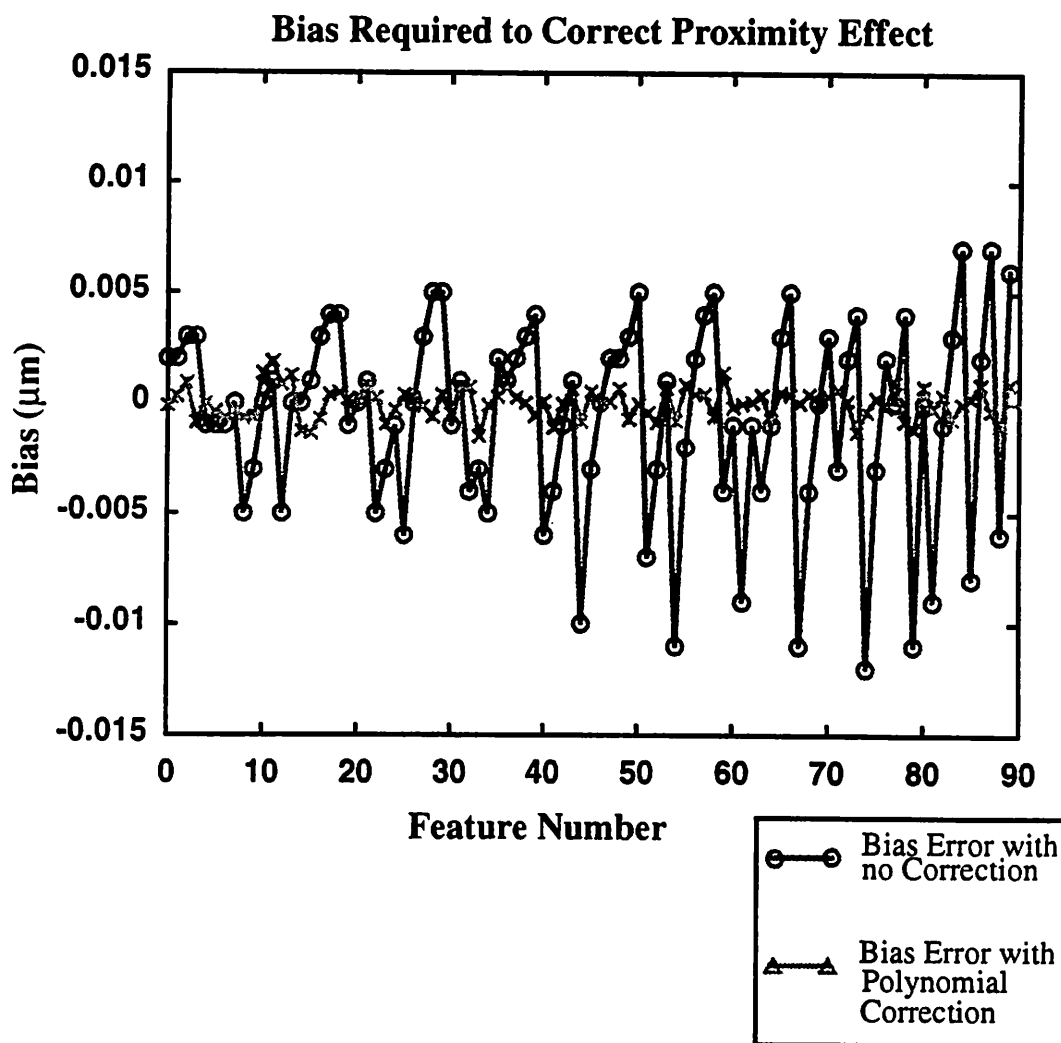


Figure 7.7 Plot of the bias required to correct an end for the proximity effects of neighboring geometry and the accuracy with which a polynomial predicts that bias.

account for the proximity influence of the nearby feature is $0.02\mu\text{m}$. The bias error with the polynomial correction is the difference between the correction predicted by the polynomial and the actual correction. The graph shows that the polynomial closely approximates the bias caused by features within the representative region. There are 90 different cases for this polynomial training set and the error is improved by 5X, from $0.02\mu\text{m}$ (0.05

λ/NA) to $0.004\mu\text{m}$ ($0.02 \lambda/NA$). The total error for the other regions is summarized in Table 7.1. The hope is that since the bias can be accurately calculated for each region, the total bias needed to correct the proximity effect for an arbitrary periphery can be predicted. This assumption is tested in the following section.

Table 7.1: Bias Range Required to Correct Proximity Effect and Accuracy of Polynomial Correction

| Region | Range before Correction (μm) | Range after Correction (μm) |
|--------|-------------------------------------------|------------------------------------------|
| 1 | 0.020 | 0.004 |
| 2 | 0.060 | 0.006 |
| 3 | 0.017 | 0.004 |
| 4 | 0.027 | 0.004 |
| 5 | 0.025 | 0.004 |

7.3.4 Real Layout Results

Given the polynomial correction functions found from training sets in all five regions for the example of an end of a line, it is possible to test the representative figure inter-feature polynomial correction function for this case on an actual layout. The layout in Fig. 7.8 is from the peripheral logic of a standard cell design. Using the methods outlined in Chapter 6, patterns are extracted which have similar base patterns but different periphery. There are 74 different patterns for the end of a line in this layout which makes it a good case study. There are enough examples to thoroughly test whether the previously trained polynomial correction can predict the correct bias for the feature. The results of applying the algorithm outlined above are shown in Fig. 7.9. The solid line is the bias actually needed to correct the feature for the proximity effects due to the periphery while the dotted line is the error between the what the polynomial predicts as the bias and the actual bias. The polynomial can correct the end of the line to within $\pm 0.025\mu\text{m}$ ($0.05 \lambda/NA$). Compared to a constant bias which would allow a correction to within $\pm 0.04\mu\text{m}$ ($0.08 \lambda/$

NA), the added effort yields a 40% improvement in accuracy. This level of improvement may be sufficient for some applications.

Layout Example for Optical Proximity Correction

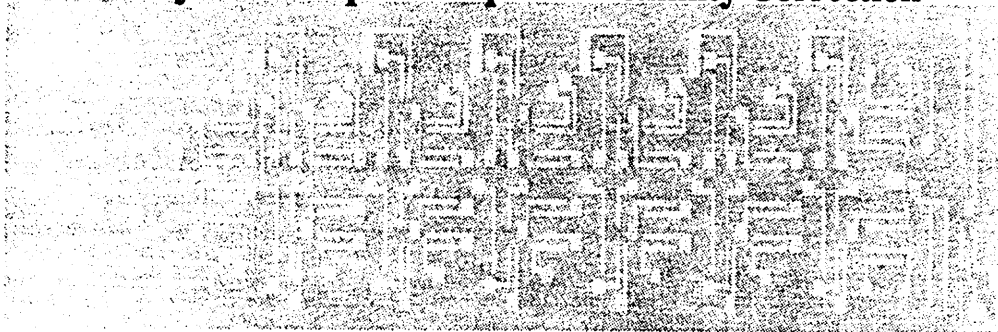
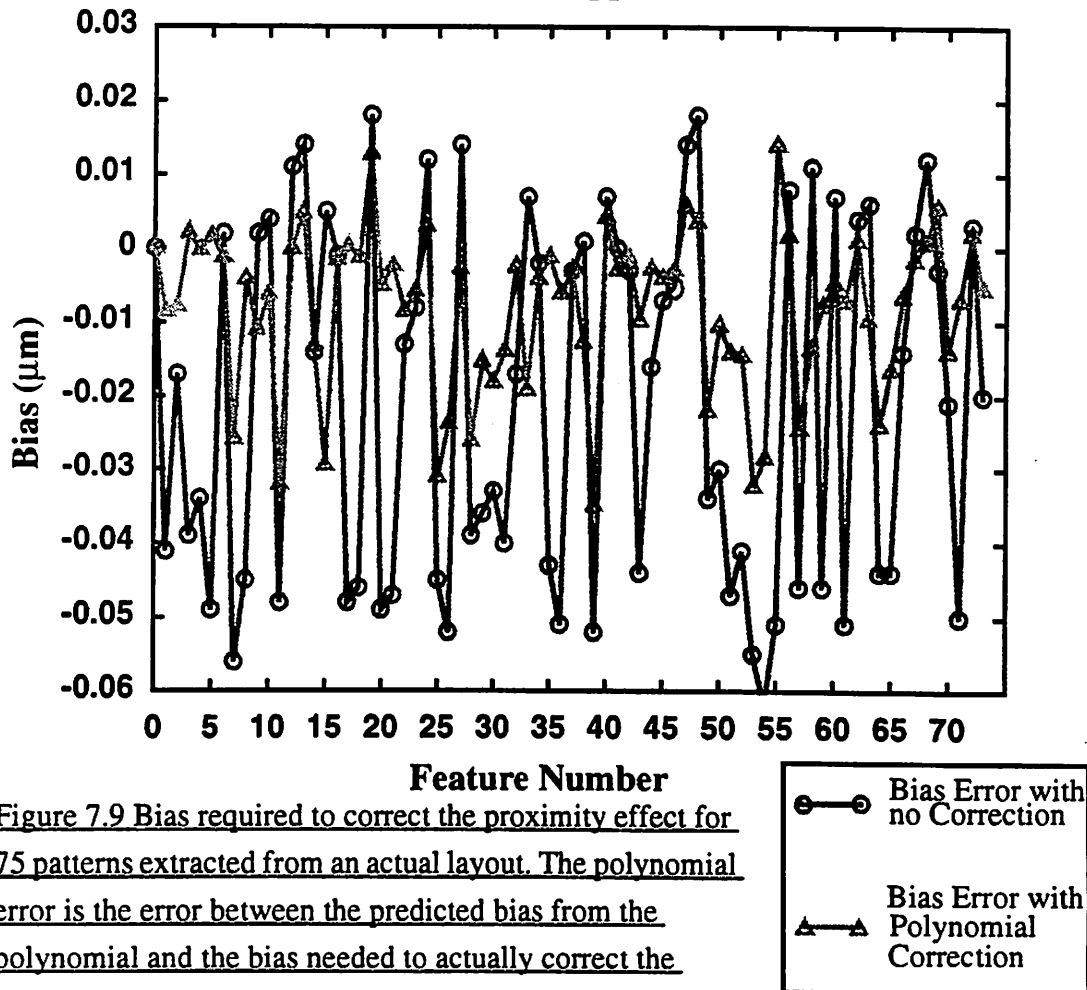


Figure 7.8 Actual layout used to obtain examples for correcting an end to account for the optical proximity effect.

Bias Required to Correct Proximity Effect and Polynomial Approximation



7.3.5 Bias Accuracy Problems

The most plausible explanation for the somewhat disappointing accuracy of the representative figure method for determining inter-feature correction polynomials is that the representative figure method is based on assumptions which are not appropriate for optical lithography. For example, Fig. 7.6a shows an original pattern and Fig. 7.6b shows the equivalent representative pattern which is used as a model for the bias correction. The basic assumption of the method is that the bias of these pattern should be approximately the same. However, for this case, the bias difference is $0.02\mu\text{m}$. This is not an isolated case of the assumed model not producing the same bias as the actual pattern. Fig. 7.10 shows that almost one-fourth of the model patterns used to replace the actual patterns in the example of section 7.3.4 exhibit a similar bias error. Essentially, the grouping of features into a single rectangle, which is the foundation of the representative figure method, is changing important coherent interactions between features. Fig. 7.11 further illustrates this point by showing that there is a strong correlation between errors in the representative pattern and errors in the correction polynomial. The correlation coefficient of 0.77 implies that over 80% of the error is caused by the use of the representative pattern. These errors account for one-half of the total error in the correction and without them, the correction should be accurate to approximately $\pm 0.015\mu\text{m}$ ($\pm 0.03\lambda/\text{NA}$) instead of $\pm 0.025\mu\text{m}$ ($\pm 0.05\lambda/\text{NA}$).

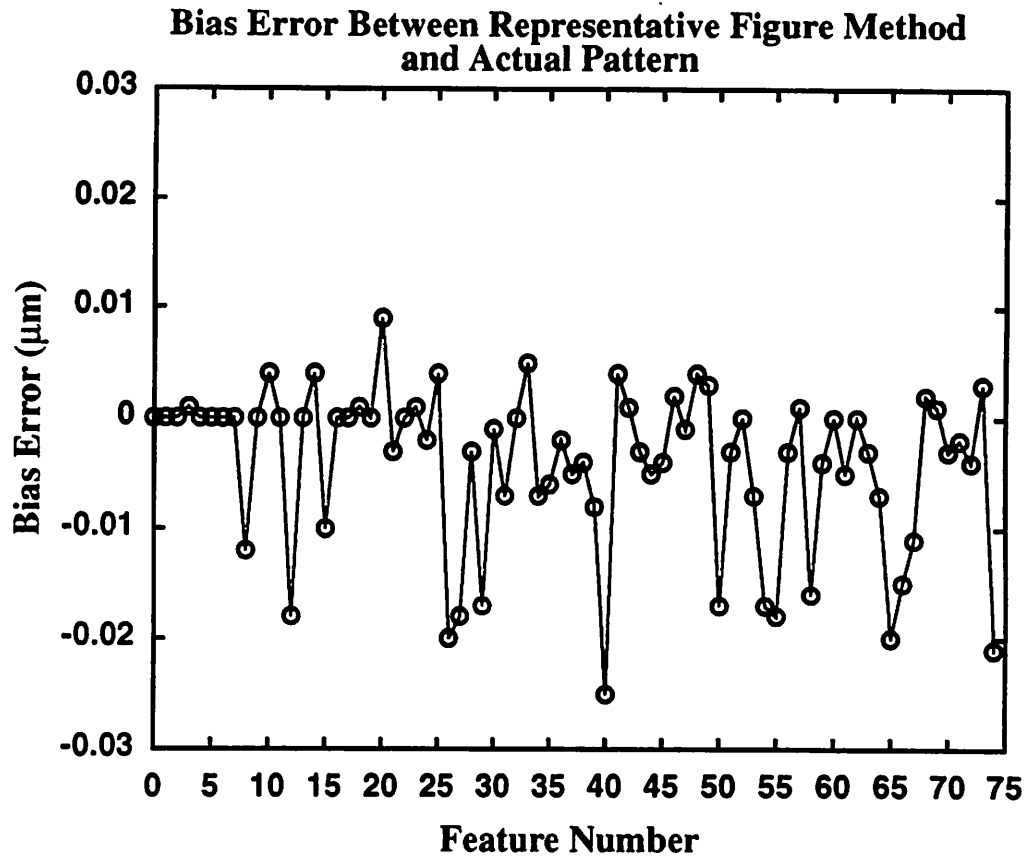


Figure 7.10 Bias error between a pattern modified to encompass the changes incurred by using the representative figure method minus the bias for the real pattern. Thus, this graph indicates the error inherent in using the representative figure method for biasing the end of lines.

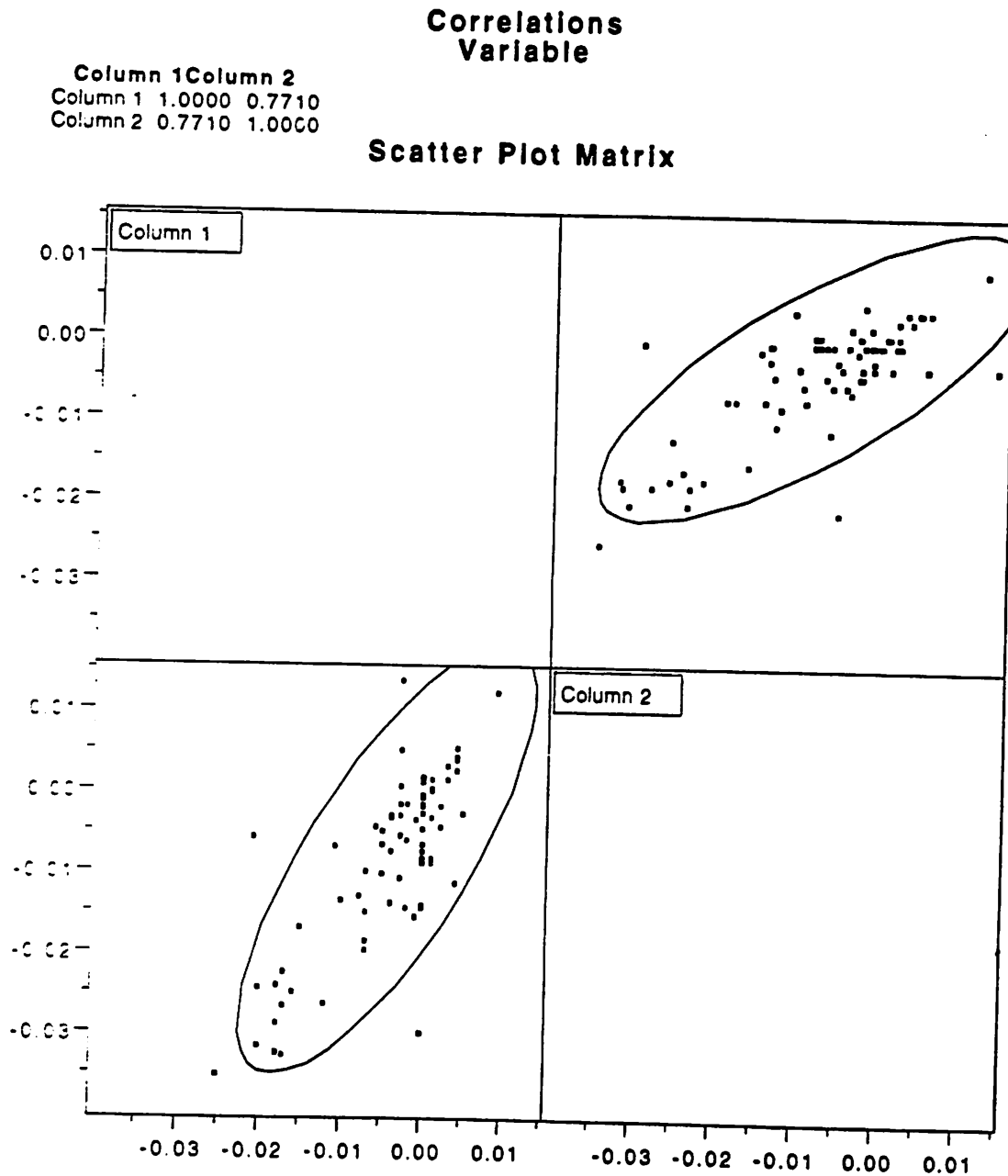


Figure 7.11 Correlation between error inherent in representative figure approach and the error present when the representative figure method is used to correct a series of patterns.

7.4 Positional Influences

The poor accuracy of this approach led us to consider the positional influence of peripheral features to determine whether the representative figure approach could be changed to improve its accuracy. Fig. 7.12 shows a simple test pattern which illustrates the positional effects of peripheral features. The base pattern is an end of a line. A contact of dimensions $0.25\mu\text{m} \times 0.25\mu\text{m}$ is placed near the end such that the center to end spacing is $0.5\mu\text{m}$ to $0.7\mu\text{m}$, where $\lambda/\text{NA} = 0.47$. The position of the contact is also varied around the end of the line. The bias of the line with no pixels is $0.065\mu\text{m}$. The bias for other configurations of pixels 1 through 5 is summarized in Table 7.2. As shown in these results, the influence of the contact is highly dependent on its position in the periphery. For example, contact #3 reduces the bias to $0.054\mu\text{m}$ while contact #1 reduces the bias to $0.062\mu\text{m}$, a difference of $0.008\mu\text{m}$ or 13%.

In addition to positional influences, another very important consideration is the nature of the interaction with multiple pixels in the periphery. Data to test this is given in Table 7.3. The table shows the impact on the bias of various combinations of pixels. The first column is the bias calculated from scratch using the optimization system while the second column shows the result of calculating the bias by linearly summing the appropriate biases of individual pixels from Table 7.2. The close approximation of the linear sum of pixel biases is quite impressive. As long as the positional dependence is maintained, the biases can be added linearly. Theoretically, this result should be expected since the inter feature contribution to the proximity effect can be viewed as a perturbation of the intensities at the line end. The strong positional influence is due to the interaction with the pattern itself. The result that pupil biases add linearly is a very important insight which can be exploited in OPC systems.

Bias Changes as $0.25\mu\text{m} \times 0.25\mu\text{m}$ Contacts are Moved Away From an End

(Pixels were simulated alone in each case)

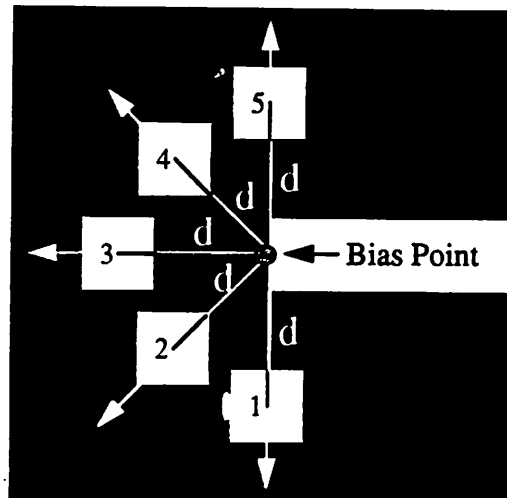


Figure 7.12 Positional influences of pixels surrounding an end of a line. The pixel center to end center spacing is $d \mu\text{m}$. Each of the pixels was simulated alone.

TABLE 7.2 Actual Biases for Contacts Located $d \mu\text{m}$ Away from an End

| $d (\mu\text{m})$ | Pixel Location | | | | |
|-------------------|----------------|-------|-------|-------|-------|
| | 1 | 2 | 3 | 4 | 5 |
| 0.5 | 0.062 | 0.057 | 0.054 | 0.057 | 0.061 |
| 0.55 | 0.065 | 0.060 | 0.058 | 0.059 | 0.064 |
| 0.60 | 0.067 | 0.060 | 0.059 | 0.060 | 0.066 |
| 0.65 | 0.069 | 0.060 | 0.060 | 0.059 | 0.066 |
| 0.70 | 0.069 | 0.061 | 0.062 | 0.061 | 0.066 |
| 0.75 | 0.069 | 0.063 | 0.064 | 0.063 | 0.067 |

TABLE 7.3 Actual Bias for Contacts Calculated Together and Individually

| Pixels | Bias (μm) | |
|-----------|--------------------------------|-------------------------------------------------------------------|
| | Bias Calculated from Optimizer | Bias Calculated from Linear Sum of Individual Pixels in Table 7.2 |
| None | 0.065 | 0.065 |
| 1 | 0.062 | 0.062 |
| 1+2 | 0.053 | 0.054 |
| 1+2+3 | 0.044 | 0.043 |
| 1+2+3+4 | 0.037 | 0.035 |
| 1+2+3+4+5 | 0.034 | 0.031 |

7.5 Pixel-Based Approach

The indication that the biases add approximately linearly when position dependence is maintained, led to the development of a more general pixel-based method for determining the inter-feature polynomial correction function. The idea differs from the representative figure approach in that the periphery is divided into square pixels and the bias caused by each pixel is calculated independently, rather than by the effect of a representative single feature. Also, the pixel approach neglects the second order effects of pixel-pixel interactions and their influence on the main feature. For convenience in the initial implementation, masks are assumed to be gridded at $0.25\mu\text{m}$ which means feature lengths and widths must be multiples of $0.25\mu\text{m}$. Furthermore, the edge nibbling or edge modification are also restricted to $0.25\mu\text{m}$ segments. This restricted environment will both demonstrate the technique and give insight into base pattern dependencies. The simplifying assumptions are illustrated in Fig. 7.13.

Edge Modifications for Simplified 2-D Biasing

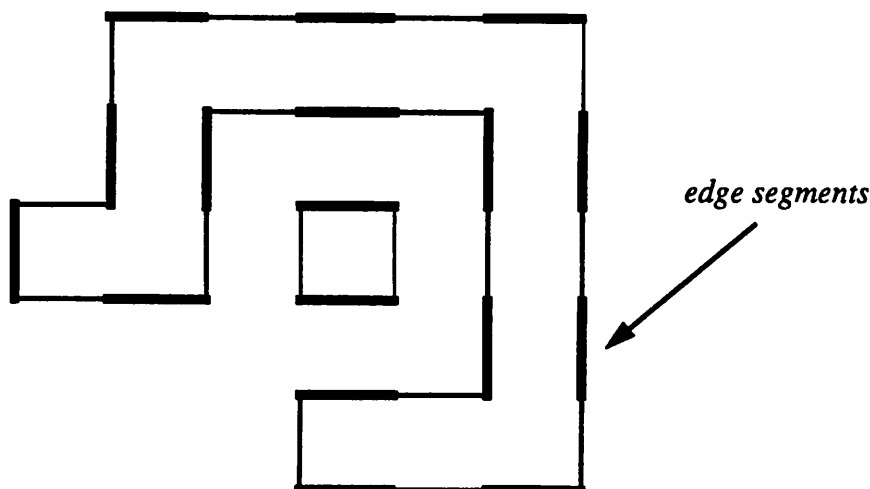


Figure 7.13 Simplifications associated with the pixel-based method for inter-feature optical proximity correction. The mask is assumed to be gridded at $0.25\mu\text{m}$ and the edge segments are split into $0.25\mu\text{m}$ sections for coarse-grid biasing.

An example of the grid used for the pixel-based approach is shown in Fig. 7.14. The clear region is the actual base pattern (a clear space on a mask). The periphery surrounding the base pattern is divided into square pixels. The bias caused by the each pixel on the end of the base pattern is shown by the number (in μm). The immediate area around the base pattern is excluded since no pixel in that area can be on without violating the design rules for the base pattern. If a pixel in that region were on, the base pattern would be different. The bias results presented here are accurate to $0.001\mu\text{m}$. A positive bias means that the bias at the bias point must be increased while a negative bias implies a decrease in the bias at the bias point.

There are several interesting phenomena associated with these results. For example, there is vertical symmetry above and below the bias point to within $\pm 0.001\mu\text{m}$. Also, the region of negative bias near the end of the line is due to the large influence of extra in-phase light interacting with the light at the end of the line. The most interesting phenomena concerning these bias results is that the bias caused by the pixels is not symmetric

about the bias point. This has a very important consequence for any optical proximity correction scheme in that any correction function must have some angular dependence.

Bias at End of Line Caused by Each Pixel Independently

| | | | | | | | |
|-------|--------|--------|--------|-------|-------|-------|--------|
| 0.0 | 0.0 | 0.0 | 0.001 | 0.003 | 0.002 | 0.0 | -0.004 |
| 0.0 | 0.0 | 0.0 | 0.0 | 0.003 | 0.004 | 0.001 | -0.002 |
| 0.003 | 0.001 | -0.005 | -0.006 | 0.0 | 0.007 | 0.004 | 0.001 |
| 0.003 | -0.005 | -0.015 | | | | | |
| 0.003 | -0.006 | -0.018 | | | | | |
| 0.002 | -0.006 | -0.015 | | | | | |
| 0.002 | -0.001 | -0.005 | -0.005 | 0.001 | 0.006 | 0.002 | -0.001 |
| 0.003 | 0.001 | 0.001 | 0.002 | 0.005 | 0.006 | 0.002 | -0.004 |

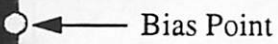


Figure 7.14 Independent pixel bias on the base pattern. The immediate area around the pattern is excluded since no pixel there can be part of the periphery based on the design rules for the layout. The bias is in μm .

Fig. 7.15a and Fig. 7.15b show two more examples of the bias needed for the pixel method of optical proximity correction. The examples demonstrate that certain patterns will not have vertical symmetry about the bias point as shown in Fig. 7.15a. This is caused by the asymmetry of the pattern itself. Also, both patterns do not have left-right symmetry since the bias caused by pixels connected to the main pattern have a much different effect than pixels not connected to the main pattern.

Bias Caused by Each Pixel Independently

| | | | | | | | |
|-------|--------|--------|--------|-------|-------|-------|--------|
| 0.0 | 0.001 | 0.000 | 0.001 | 0.002 | 0.001 | 0.0 | -0.001 |
| 0.002 | 0.001 | 0.0 | 0.001 | 0.003 | 0.005 | 0.002 | -0.001 |
| 0.002 | 0.000 | -0.003 | -0.005 | 0.003 | 0.009 | 0.004 | 0.002 |
| 0.002 | -0.005 | -0.011 | | | | 0.006 | 0.003 |
| 0.002 | -0.004 | -0.011 | | | | 0.006 | 0.002 |
| 0.002 | -0.004 | -0.011 | | | | 0.002 | 0.001 |
| 0.001 | 0.000 | -0.002 | 0.000 | 0.001 | 0.002 | 0.000 | -0.002 |
| 0.002 | 0.001 | 0.002 | 0.002 | 0.003 | 0.004 | 0.000 | -0.001 |

(a)

| | | | | | | | |
|-------|--------|--------|--------|-------|-------|--------|--------|
| 0.0 | 0.000 | 0.000 | 0.001 | 0.002 | 0.001 | -0.001 | -0.001 |
| 0.001 | -0.001 | -0.001 | 0.000 | 0.003 | 0.004 | 0.001 | -0.002 |
| 0.002 | 0.001 | -0.003 | -0.004 | 0.001 | 0.006 | 0.003 | 0.000 |
| 0.003 | -0.004 | -0.013 | | | | 0.008 | 0.002 |
| 0.002 | -0.006 | -0.016 | | | | 0.011 | 0.001 |
| 0.001 | -0.006 | -0.013 | | | | 0.007 | 0.001 |
| 0.002 | 0.000 | -0.005 | -0.005 | 0.002 | 0.006 | 0.002 | -0.001 |
| 0.003 | 0.001 | 0.002 | 0.001 | 0.002 | 0.005 | 0.002 | -0.002 |

(b)

Figure 7.15 Independent pixel bias on the base pattern. This example is for a matching zone of 4X4 pixels in the center of the proximity window. Even though pixels may be touching the feature at the left or bottom, they are still considered to be in the periphery. (a) Elbow pattern. (b) End of line pattern used in Fig. 7.15 to correct the bias at the end of lines.

To test the pixel based approach, the base pattern in Fig. 7.15b, a line end with a 4X4 pixel ($1.0\mu\text{m} \times 1.0\mu\text{m}$) matching zone, is used. The polynomial function is applied to the same set of patterns as the ones used by the representative figure method. The results are shown in Fig. 7.16. They are quite impressive, and illustrate a prediction accuracy of $\pm 0.01\mu\text{m}$ ($0.02 \lambda\text{NA}$), or a 4X reduction in the proximity effect, a value which is acceptable for most applications.

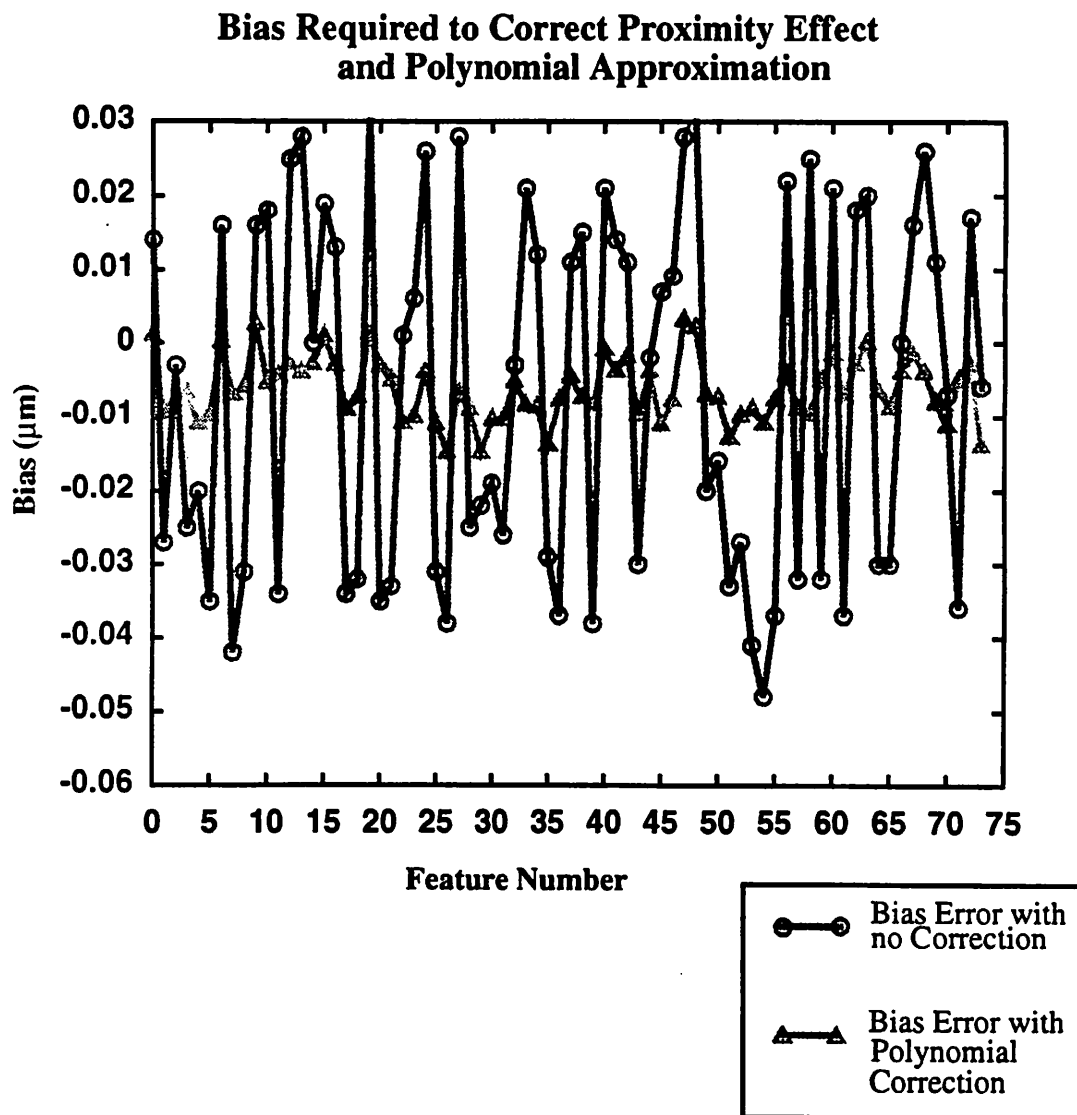


Figure 7.16 Bias required to correct the proximity effect and the polynomial approximation for the pixel-method. Note that this method can predict the bias for the inter-feature proximity effect to within $\pm 0.01\mu\text{m}$.

7.6 Example with Current System

Based on these results, a pattern-based optical proximity correction system was implemented in OCT/VEM/RPC to show the potential of the system to correct the ends of a line. A section of an industry layout is shown in Fig. 7.17. The biased mask is shown in Fig. 7.18. Note that the correction is only applied to the end of lines; all other feature are unchanged. In Fig. 7.19, all the ends in the pattern are simulated with SPLAT to show that the intensity contour does not match the mask pattern at the end of lines. In Fig. 7.20, the biased mask is simulated and the SPLAT contours now match the original mask as desired by the designer.

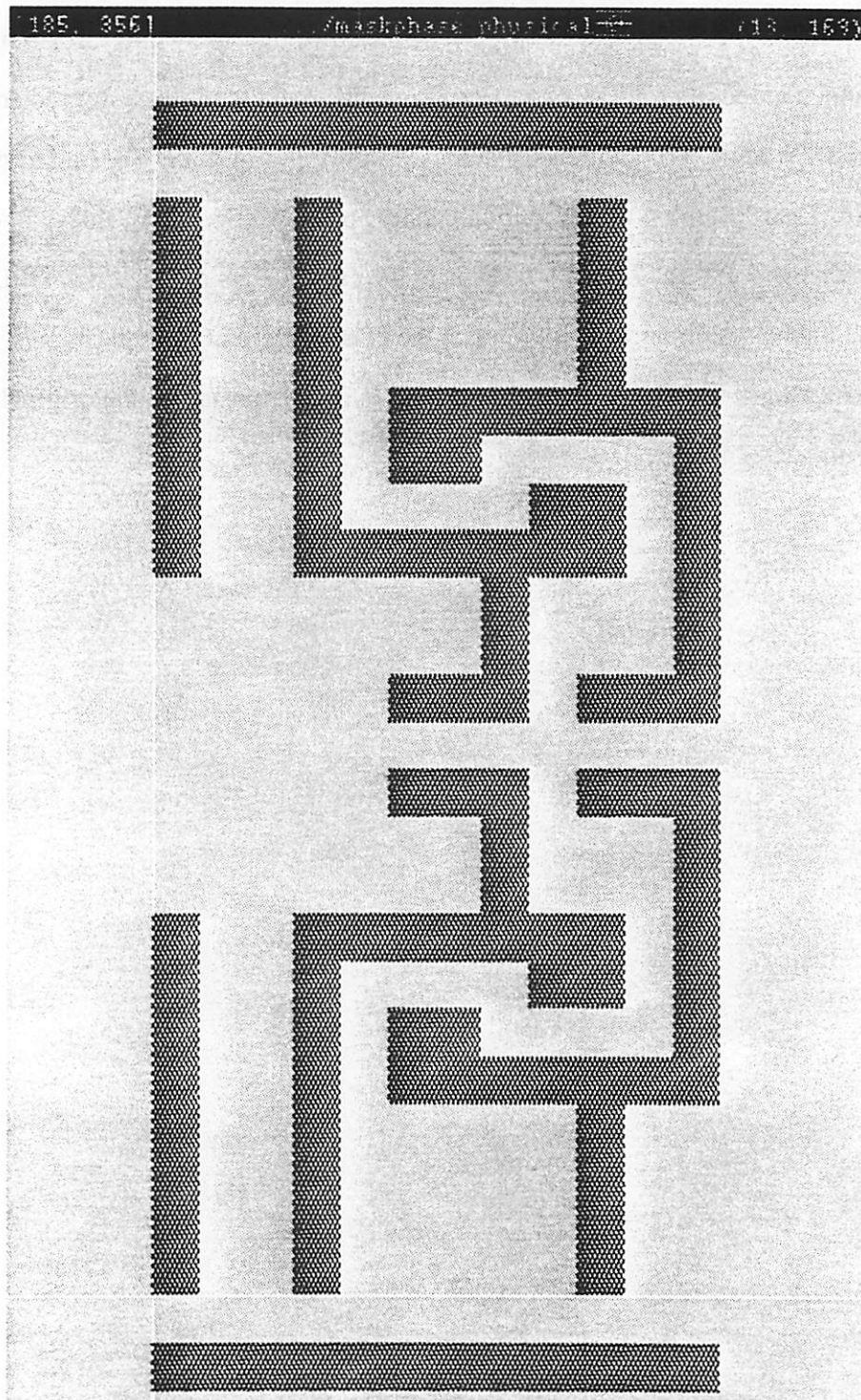


Figure 7.17 Test layout for correcting ends of lines for the proximity effect. The periphery around each end is subtly different, necessitating slightly different corrections for each instance.

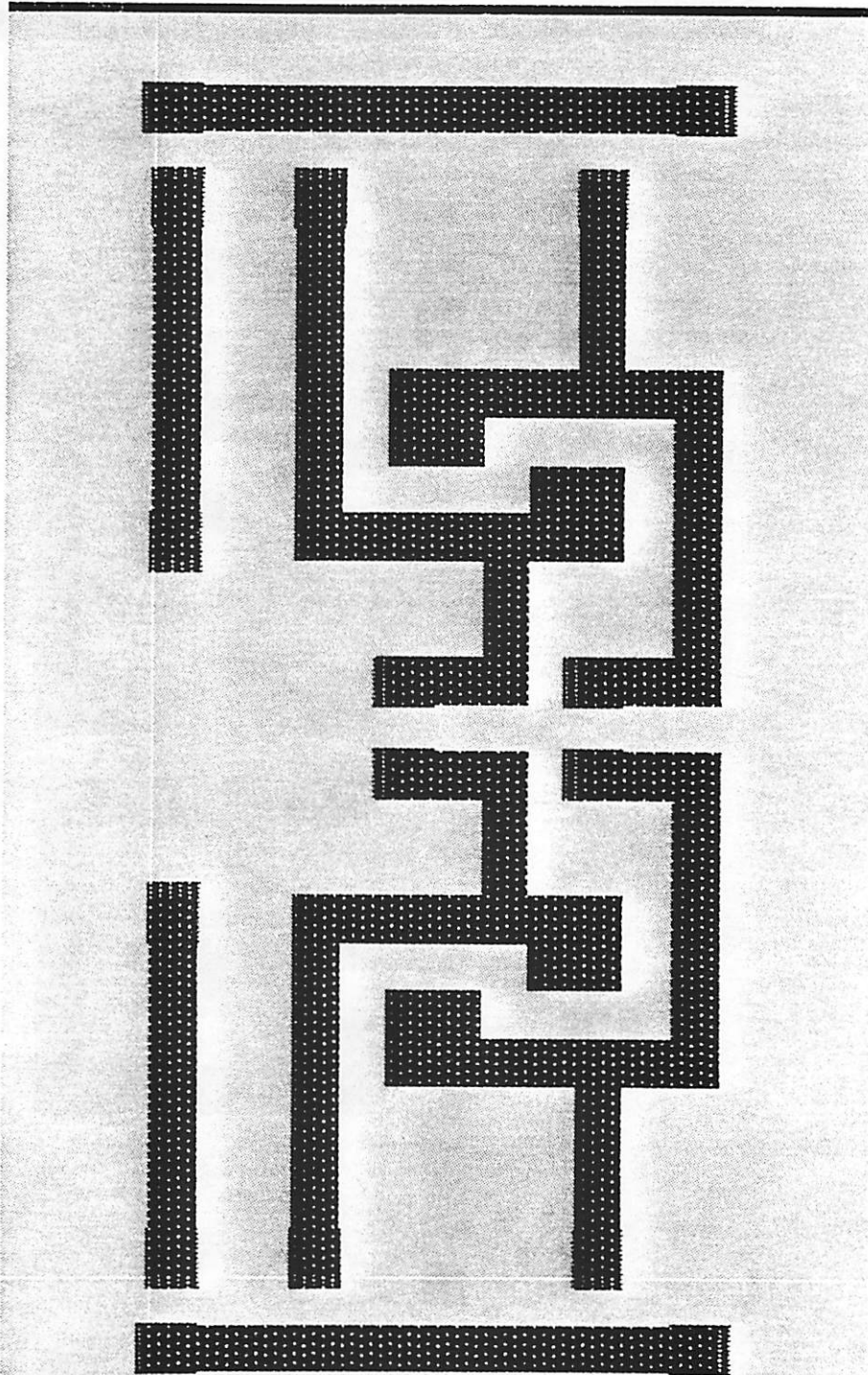


Figure 7.18 Previous layout corrected to account for proximity effects at the ends of lines. Note that there are proximity corrections only at the ends of lines. If other features need correction, a new pattern must be simulated and tested to correct that type of feature.

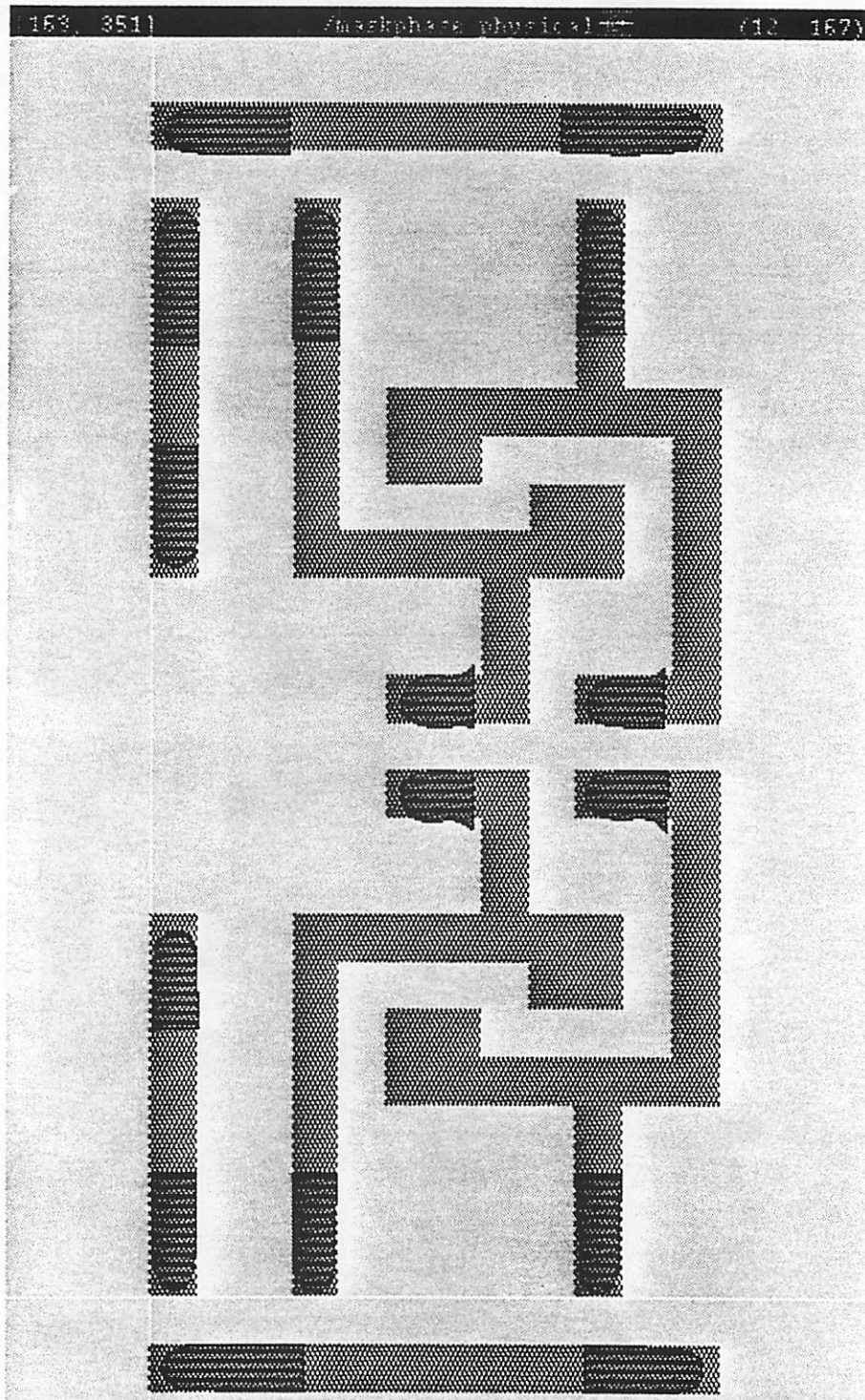


Figure 7.19 SPLAT simulations of the ends in the layout, showing that the 0.3 intensity contour does not match the edge of the mask as required by a robust pattern transfer step.

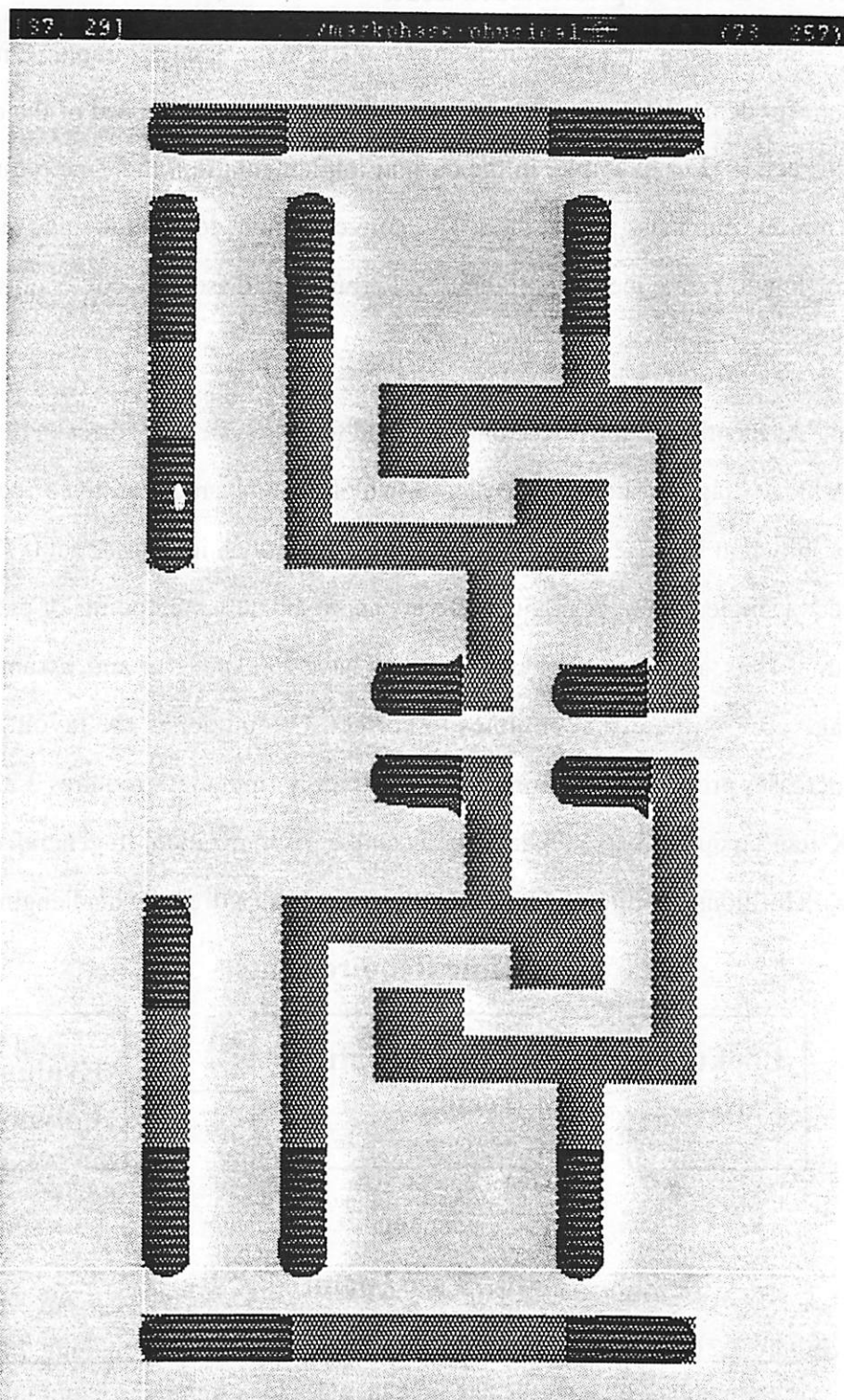


Figure 7.20 SPLAT simulations of the 0.3 intensity contour with the proximity correction. Note that the intensity contour more closely matches the edge of the original mask after correction.

7.7 Practical Implementation Issues

Several simplifying assumptions are made in the practical implementation of this system for demonstration purposes which directly impact the speed of the optical proximity correction. For example, in the current implementation, the time required to correct a 1mm X 1mm mask is 2.22 days. This correction time does not include the 30 days needed off-line to create the pattern libraries. Fortunately, these time constraints are not inherent to the system.

As mentioned above, the time required for this system to correct a mask is quite large. A block diagram showing the breakdown of the times required to correct a single pattern is shown in Fig. 7.21. As the system currently works, it takes about 0.77 seconds to correct a single pattern or point. There are approximately 0.25 points or patterns needed per μm^2 . Thus, a $100\mu\text{m} \times 100\mu\text{m}$ mask will have 2500 patterns and, assuming no hierarchy, take approximately 32 minutes to correct. Of course, as the layout grows, the time increases proportionally. For example, a 1mm X 1mm mask requires 2.22 days and a 1cm X 1cm layout will take 23 days for a complete optimization. In general, correcting masks with millions of features for proximity effects is an extremely challenging endeavor.

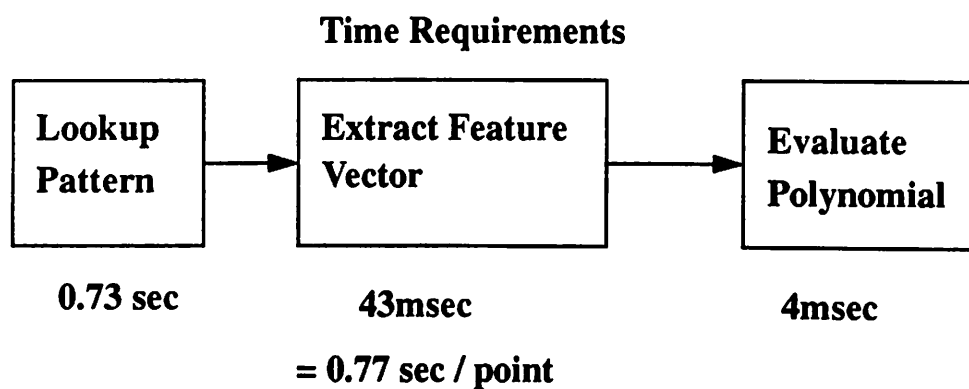


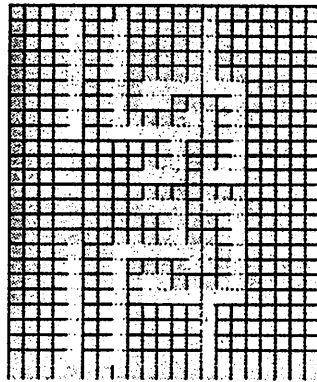
Figure 7.21 Block diagram of the time requirements for calculating the bias for each correction point on a mask. The time includes looking up the pattern in the library, extracting the feature vector, and evaluating the polynomial correction function.

Not only are the time requirements for instantiating the corrections excessive, but also the time needed to generate the library itself is extremely time-consuming. For example, a simple layout with thirteen patterns will require $44 \text{ Pixels} * 10 \text{ SPLAT Runs/Pixel} * 13 \text{ Patterns} = 5720 \text{ SPLAT Runs}$. (Ten SPLAT runs are required to optimize each pattern.) At two minutes per SPLAT run, the total time is 7.9 days on a DECstation 5000/125. Of course, a complex layout with 50 patterns will require proportionally longer, approximately 30.6 days.

Even though the time constraints may at first seem to be a serious problem, they can be reduced by speeding up various parts of the system. For example, the library access can be decreased by a factor of 100X using more sophisticated algorithms. This improvement would reduce the time needed to instantiate corrections into a layout from 23 days to 2 days. Also, utilizing the mask hierarchy can yield 3-100X speed improvements, especially if the correction is run in parallel. The library generation is also a problem, but speeding up SPLAT by fully utilizing fast fourier transforms might decrease the time needed to generate patterns for the library by 10 to 1000X. In addition, the library generation system is easily run in parallel.

The key underlying problem with pattern-based optical proximity correction is that the number of patterns in a given layout may be too large. To get an initial indication of the number of patterns, several typical layouts have been evaluated, as shown in Fig. 7.22. Although these layouts have some repetition, the pattern library needed for each is still quite significant considering the relatively small size of layout. These results correspond to about 50 pattern per design cell. As larger problems are solved, the total number of patterns in the library may continue to increase to the point where several hundred or several thousand different patterns must be optimized for the library. Also, as the library times continue to increase, the library size becomes larger, which will require more sophisticated algorithms for searching the database for matching patterns. More careful

Typical Layouts and Pattern Counts



**2 μ m X 2 μ m window
with 1 μ m X 1 μ m
matching zone**

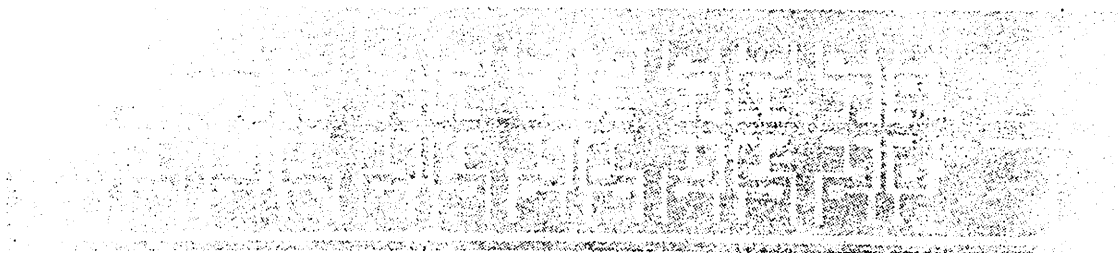
13 Patterns

(a)



45 Patterns

(b)



44 Patterns

(c)

Figure 7.22 Typical layouts and pattern counts for some masks. (a) This layout is part of a standard cell design that was snapped to a 0.25 μ m grid. (b) Industrial layout. (c) Industrial layout.

studies of how the number of patterns grows with design cell area and with the number of cells designed by different designers are clearly needed to determine the efficiency of pattern based OPC approaches.

7.8 Overall Perspective

These considerations have led us to the realization that pattern-based optical proximity correction algorithms would be more appropriately applied in cases where only certain modifications must be made to the mask. For example, often designers are concerned that the poly overlap over the gate is sufficient to prevent short-circuiting the source and drain of the transistor. One use of the pattern-based optical proximity correction algorithm, then, is to correct only those areas of the layout which are stored in the pattern library. In other words, only the patterns which we care about are corrected. For instance, in the example of section 7.6, the only pattern that is modified is the one for the end of a line. The power of this approach is that the pattern library can be adjusted such that it corrects only those features which cause the most trouble while maintaining the powerful characteristic that each feature is corrected independently, depending on the periphery around that feature. As another example, the existing system could be extended to do proximity correction for protection against shorts along wires. In that case, the pattern may be the edge of a line. All such edges would be corrected as part of a single pattern to do proximity correction for that feature.

Admittedly, pattern-based optical proximity correction may not be the optimum correction algorithm in some instances. For example, the TVT and AT&T ray trace method is best for cases where simple 1-D rules are sufficient. The system can be extended to 1.5-D if special cases and additional rays are added to the tables. The zone-sampling model used by PRECIM, can also be useful where it is necessary to correct entire masks and fold empirical data about plasma etching into the system. Nevertheless, both of these optical

proximity correction algorithms will someday need a pattern recognition system to separate the critical features which must be corrected from those which do not need any correction. The need for such a synergy between pattern recognition and other optical proximity correction schemes stems from the inherent problem that correcting an entire mask will generate so much additional data that the mask writing machines will be overwhelmed. If corrections can be applied only where necessary, this problem can be overcome.

References for Chapter 7

- [1] Takayuki Abe, Satoshi Yamasaki, Ryoichi Yoshikawa, and Tadahiro Kakigawa, "Representative Figure Method for Proximity Correction," Vol. 30, No. 3B, March 1993, pp. L528-L531.

Chapter 8 Conclusion

The use of resolution enhancement techniques could have a dramatic impact on optical lithography by allowing the manufacture of the next generation of integrated circuits on existing lithography processing equipment. Although many experiments have been done which indicate that these techniques should yield vast resolution improvements, their practical application to realistic layouts is still forthcoming. There are several reasons for this delay. Most importantly, at these dimensions and with the techniques available, mask proximity correction is essential; thus, there is a need for the development of sophisticated algorithms which can apply optical proximity correction to layouts. Also, a variety of physical phenomena in imaging, substrate reflections, and resist reaction kinetics, must be understood more thoroughly to incorporate even more sophisticated physical models into the proximity correction schemes.

The overall goal of this thesis is to investigate resolution enhancement techniques and explore the issues involved in applying proximity correction to a phase-shift or attenuating mask. The first step in this process is to sort out the various resolution enhancement methods to determine their relative effectiveness in improving resolution and depth of focus. Next, 1-D optical proximity correction algorithms are investigated to determine whether it is possible to correct simple patterns for proximity effects. Third, experimental verification of the resolution enhancement techniques and proximity correction algorithms is necessary. Once simulation and experimental insight into 1-D features is understood, 2-D proximity correction algorithms for small areas are examined. Finally, a 2-D pattern classification scheme is devised to correct specific patterns and to gain insight into other proximity effects and correction approaches.

A main contribution of this thesis is the demonstration that simulation can be used to evaluate resolution enhancement techniques and then bias them to correct for 1-D optical proximity effects. To investigate phase-shift mask techniques and to bias masks to print features at the desired dimensions, a design system, DRGEN, was developed during a summer at AT&T Bell Labs. The system is first used to analyze a variety of phase-shift mask and illumination systems. Based on its exceptional performance for printing constant width lines of varying duty cycle, the rim phase-shift mask with annular illumination is chosen as a candidate technique for optical proximity correction. DRGEN is then used to bias the rim size on the mask such that all features print lines with the same critical dimension. In all, over 10,000 SPLAT runs were necessary to choose an appropriate resolution enhancement technique and bias the mask for optimal performance.

To confirm the simulation results, a mask is designed to print $0.30\mu\text{m}$ and $0.22\mu\text{m}$ lines of varying pitch. Subsequent experiments with the $0.30\mu\text{m}$ features on this reticle confirm some simulation predictions and indicate areas where further understanding is necessary. For example, experimental evaluation of the depth of focus versus pitch indicates that there is a dead zone in focus at a specific pitch. This dead zone is important because it indicates that previous experimental results of resolution enhancement techniques with only dense lines and spaces and isolated lines or spaces are misleading. They do not show that the depth of focus can be much less for some features. Experiments with $0.22\mu\text{m}$ features in APEX-E illustrate the capability of rim phase-shifting masks with annular illumination to print very aggressive geometries. However, the dense-iso split is quite serious at these linewidths and TCAD simulation results indicate that the problem may be related to physical properties of the resist.

The other main contribution of this thesis is the demonstration that 2-D optical proximity correction can be accomplished using relatively slow but accurate aerial image simulation programs. Our approach uses 2-D biasing and pattern recognition. The 2-D

optimizer itself is quite useful for biasing small patterns because it is fast, accurate, simple, and converges in five to ten iterations. Combining the 2-D optimization results with a pattern library and inter-feature correction polynomials allows the system to correct specific types of patterns in much larger layouts. The inter-feature correction polynomials arise from the insight that the proximity effects due to patterns in the periphery can be linearly superimposed. The 2-D pattern correction system is implemented in the OCT/VEM CAD system to demonstrate the correction of specific types of patterns. The eventual usefulness of such a system depends upon the assumption that the designer will know the small set of patterns that will likely cause problems in the layout.

However, the successful implementation of optical proximity correction for larger layouts will require a much more sophisticated system. It will need to use the hierarchy of the layout to reduce the total computation. The system must distinguish between minimum-sized patterns which require optical proximity correction and larger features which do not need any layout modifications. The number of patterns in the layout is critical since large libraries will slow down the correction speed of the system. The pattern, rule, or function set used for proximity correction must be easy to create or modify for various types of mask and stepper configurations. Furthermore, resist effects appear to have a significant influence on the proximity correction and adjustments must be made to the optimization algorithms to account for them.

Once the system has been implemented, further testing of resolution enhancement techniques can begin. With a corrected aerial image, it is possible to test resolution enhancement technology on real layouts to determine the extent of the improvement. Also, these experimental results will point to areas of the optical proximity correction algorithm which need additional work to incorporate resist effects. It may be possible to use a transfer function which will incorporate the influence of the resist, instead of relying only on the aerial image. After these problems are resolved, resolution enhancement tech-

niques and optical proximity correction will become useful in production. Optical proximity correction may, in fact, be used alone to remove systematic errors in the lithography process which can then lead to tighter linewidth control. In either case, proximity correction will likely have application in photolithography.